The Herschel Catalogue of Solar System Object Observations - Explanatory Supplement

Volume I

The Herschel-PACS Solar System Object Observations Comet Catalogue

HERSCHEL-HSC-DOC-2200

Version: 1.0

25th July 2018

The Herschel Catalogue of Solar System Object Observations - Explanatory Supplement

Volume I: Herschel-PACS Solar System Object Observations Comet Catalogue

Prepared by:

Cristina Romero Calvo[1, 2], Mark Kidger[1], Miriam Rengel[1, 3, 4] and Mircea Stoica[5]

1. Herschel Science Centre, European Space Agency, European Space Astronomy Centre
2. Technische Universität Berlin, Germany
3. Max-Planck-Institut für Sonnensystemforschung, Germany
4. European Organisation for the Exploitation of Meteorological Satellites, Germany
5. University Medical Center Hamburg-Eppendorf, Department of Neurophysiology and Pathophysiology, Hamburg, Germany

HERSCHEL-HSC-DOC-2200, Version: 1.0, 25th July 2018

1. Abstract

We present the first volume of the Herschel Catalogue of Solar System Object Observations (HCSSO). This has been prepared as a complement to the two catalogues of Herschel point source observations: The Herschel/SPIRE Point Source Catalogue (HSPSC) and the Herschel/PACS Point Source Catalogue (HPPSC), which filter and exclude moving targets.

Although most of the solar system objects observed by Herschel were inactive, point sources, ten active comets were also observed, mainly at 70 and 160 μm, several of them at more than one epoch, although there were also a few observations at 100 μm. Both short period, Jupiter Family comets, mainly making close passes to Earth and non-periodic objects were observed by PACS. The resultant sample covers a variety of objects with a wide range of dynamical history and level of activity: five Jupiter family objects, and five non-periodic objects.

For these objects the standard recipes for point source aperture photometry make no sense, as the coma may be much larger than the recommended aperture size for point sources. Similarly, due to the differing geocentric distances for the objects observed, a constant aperture size may correspond to very different physical aperture sizes at the comet, making direct comparison of activity of different objects impossible. For extended objects we can extract two-dimensional photometric information giving the radial distribution of dust emission within the coma and, at the same time, allowing us to calculate photometry for identical physical apertures.

In this first volume, we present an atlas of images, physical circumstances of observation, photometric radial profiles, radial profile fits and photometry in multiple angular and physical aperture sizes for active comets observed by Herschel that are clearly extended targets: this information we make available so that it can be used for modelling, or for comparative studies.

Volume II will present the main body of the catalogue, with a full listing of all Herschel targeted observations of SSOs, physical circumstances, photometry compiled from the literature for sources with published data and measured systematically and homogeneously by ourselves for those that do not and such ancillary data as is necessary to place the Herschel data in its proper context.

We intend that a future Volume III will present a similar compilation of serendipitous observations of Solar System Objects, identified and rejected in the HSPSC as moving targets, some of which are doubly excluded as also being clearly extended.

2. Table of Contents

3. Introduction

The Herschel Space Observatory (Pilbratt et al. 2010) was the fourth cornerstone mission in the European Space Agency (ESA) science programme. It had a primary mirror of 3.5m in diameter that allowed an unprecedented spatial resolution and sensitivity at far–infrared (FIR) and sub–millimetre (smm) wavelengths.

Herschel operated successfully from June 2009 to 29 April 2013 when it ran out of the liquid helium coolant required to maintain the operational temperatures for the instruments' detectors.

The three instruments on-board covered the FIR and smm spectral range from 55 to 671 μm. The Photodetector Array Camera and Spectrometer (PACS, Poglitsch et al. 2010) and the Spectral and Photometric Imaging REceiver (SPIRE, Griffin et al. 2010) were able to make both spectroscopic and photometric observations, while the Heterodyne Instrument for the Far Infrared (HIFI, de Graauw et al. 2010) was a purely spectroscopic instrument. Over 35 000 science observations were made during the more than 25 000 hours of science time, while approximately 10 000 calibration observations were also made in standard science modes and are of science quality. The large legacy dataset that was obtained that is far from having been fully analysed and which still has a great potential for new scientific discoveries, which provides the motivation for the present catalogue.

The observing time was allocated to both Guaranteed Time (GT) and Open Time (OT) Programmes. Many excellent source catalogues have already been produced by these observing programs, however there are many observations that remained unexplored. To maximise the scientific return of the Herschel photometric observations, the Herschel/SPIRE Point Source Catalogue (HSPSC, Schulz el al. 2017) and the Herschel/PACS Point Source Catalogue (HPPSC, Marton el al. 2017) were generated.

These provided a homogeneous source extraction that enables a systematic and unbiased comparison of sensitivity across the different Herschel fields, which single programs will generally not be able to provide, making them a fundamental resource for future generations of data-miners. The extracted point sources include mainly individual YSOs and unresolved YSO clusters of our Galaxy, as well as the dusty extragalactic objects of the local and distant Universe. Such a huge dataset can help scientists better to understand the early phases of star and galaxy formation in addition to the possibility of carrying out statistical analysis of stellar and galaxy clusters to unravel astrophysical evolution laws through time. They will also provide an excellent target list for future proposals with ground and space-based facilities.

However, although both the HSPSC and the HPPSC detected thousands of Solar System Objects, these were rejected in the filtering process, which identified and eliminated moving targets, leaving a homogeneous set of fixed targets but, in the process, removing an important sub-set of science targets.

The motivation for the Herschel Catalogue of Solar System Object Observations is as a complement to the HSPSC and the HPPSC, producing an equivalent homogenous compilation of photometric data in the six Herschel bands between 70 and 500 μm for solar system objects observed by Herschel.

Within Volume II of this catalogue we present both PACS and SPIRE data. In this volume we treat only PACS data. The principal reason for this is that, unlike for PACS, the amount of unpublished SPIRE data of active comets is extremely small. At the same time, the much lower s/n of the SPIRE data and the number of background sources close to the target that have a flux comparable to or higher than the SSO being observed, makes reliable photometry of extended sources extremely difficult to extract. We thus limit ourselves to the larger and more reliable PACS data set.

The three Herschel instruments were designed to meet the goals of the mission to study the formation of stars and galaxies, physics of the interstellar medium, astrochemistry and solar system research.

Herschel performed around 37000 science observations of which 1693 were from Solar System objects (4.5% of the total) which represent 170 individual objects, including 5 planets and 6 of their satellites, 14 comets, 107 TNOs and 38 other asteroids. These measurements have been only partially exploited and to facilitate their analysis we have compiled these observations in the Herschel Catalogue of Solar System Object Observations (SSOO). We have included a detailed classification of the observed bodies, a complete ancillary information as well as physical circumstances of the observations (phase angle, heliocentric distance, etc.) to facilitate a search for correlations between properties.

In order to provide further information of interest we analysed 1287 photometric observations from PACS. We used the science ready maps in the Herschel Interactive Processing Environment (HIPE)v15.0.0 and due to the diversity of the 170 SSO (e.g. TNOs, planets) we had to develop a pipeline for applying point source aperture photometry to the different bodies. The quality of the measurements had been analysed taking into account the source flux, sky background and published results from different types of bodies and the flux densities of the SSOs.

We aim to facilitate the analysis of Herschel SSO data and help the scientific community to use the archive to widen our knowledge of the Solar System. Our own analysis of the data in this catalogue will be presented both as part of the Explanatory Supplement and as scientific publications.

4. Acronyms

ADP	Ancillary Data Product
Aka	Also known as
AU	Astronomical Unit
ESA	European Space Agency
FIR	Far InfraRed
GT	Guaranteed Time
HCSSOO	Herschel Catalogue of Solar System Object Observations
HIFI	Heterodyne Instrument for the Far Infrared
HIPE	Herschel Interactive Processing Environment
HOTAC	Herschel Observatory Time Allocation Committee
HPDP	Highly Processed Data Product
HPP	Herschel PACS Photometry (data product)

HPPSC	Herschel-PACS Point-Source Catalogue
HSA	Herschel Science Archive
HSPSC	Herschel-SPIRE Point-Source Catalogue
IAU	International Astronomical Union
JPL	Jet Propulsion Laboratory
LD	Lunar Distance(s)
MPC	Minor Planet Circular or Minor Planet Center (according to context)
NAIF	Navigation and Ancillary Information Facility (NASA)
ObsID	Observation Identifier
OD	Operational Day
OT	Open Time
PACS	Photodetector Array Camera
PSF	Point source Spread Function
s/n	Signal-to-noise
SAA	Solar Aspect Angle
smm	Sub-millimetre
SPICE	Spacecraft Planet Instrument C-matrix Events
SPIRE	Spectral and Photometric Imaging REceiver
SSO	Solar System Object
SSOO	Solar System Object Observations
ToO	Target of Opportunity
YSO	Young Stellar Objects

5. Catalogue objectives

5.1. Background

The aim of this work was to use all the Solar System performed observations to create the Herschel Catalogue of Solar System Object Observations (HCSSOO), as a Herschel Highly Processed Data Product (HPDP), the goal of which is to become a reference archive from which information may be extracted selecting by type (e.g. object class, albedo, colour index) for comparative statistical studies and further exploitation of the data.

As an addition, our own analysis of the data (e.g. PACS photometric study of active comets) will be presented in Romero Calvo (2018, Masters Dissertation, Technische Universität, Berlin, Fakultät VI, IGG).

5.2. Scope

Herschel produced 1693 good quality SSOO. The observations were made by two cameras/medium resolution spectrometers covering the following wavelengths: PACS (57-210µm) SPIRE (191-671µm) and a very high resolution heterodyne spectrometer HIFI (157-625µm).

All these observations are included in the catalogue, the creation of which consisted of 4 steps:

1. Compilation of the Herschel Catalogue of Solar System Object Observations.

1693 science observations referring to 170 different bodies, including Major Planets, Minor Planets (NEOs, MBAs, Centaurs, TNOs), Satellites and Comets are compiled into the HCSSOO. The process of compilation also involved the analysis of 63 available publications which used Herschel observations of the Solar System.

2. Organization of the information in order to facilitate accessibility and retrieval.

The aim of the catalogue is to be as complete as possible, for this reason different type of information was included, this information had been divided into three sections due to explanatory purposes:

(a) Classification of the observed bodies to facilitate defining samples This section will consist on the following information: NAIF id, International Astronomical Union nomenclature, target, alternative names, first classification, dynamical classification, second dynamical classification, classification comment.

(b) Complete ancillary information for each SSOO

The following data will be included: Observation id, operation day, start time, integration time, proposal ID, scientific mode, instrument, band wavelength, postcards, related publications.

(c) Physical circumstances for each SSOO

In this section physical circumstances for each solar system observed object will be found such as albedo and its standard deviation, V-R, B-V colour indexes and their errors, right ascension and declination, illumination, heliocentric range, observer range, phase, method flux, flux and its standard deviation.

3. Completion of the missing information in the catalogue.

In order to maintain homogeneity in the catalogue and provide further information of interest a photometric study using PACS observations was carried out. The Herschel Interactive Processing Environment (HIPE)v15.0.0 was used to analyse science ready maps and to follow a pipeline which its main basic operations were:

(a) Source fitting of the body

(b) Annular sky aperture photometry

(c) Photometric aperture correction

(d) Colour correction

The final result is the monochromatic colour corrected flux density. The quality of the measurements was analysed taking into account the source flux, sky background and published results from different types of bodies and flux densities of SSO.

4. Catalogue dissemination and preserving it as part of the Herschel Legacy Archive.

We aim to facilitate the analysis of Herschel SSO data and help the scientific community to use the archive to widen our knowledge of the Solar System. The catalogue will be published in the Herschel Science Archive as part of Herschel Legacy.

6. The PACS instrument and its data

For a full description of the PACS instrument and its capabilities, we recommend the overview paper of Poglisch et el (2010) and the PACS Handbook (Exter, 2017). Within these will be found ample references to more detailed descriptions and documentation, should these be required.

6.1. Background

PACS was designed as a general-purpose science instrument for the far-infrared, operating within the wavelength range 51–210 µm. It incorporated two sub-instruments.

1) An imaging dual-band photometer ($\Delta\lambda/\lambda$ <0.5) operating over an instantaneous field of view (FoV) of 3.5'x1.75', with full sampling of the telescope point spread function. Bandpass combinations were either 60–85 µm and 125–210 µm (blue/red filter) or 85–125 µm and 125–210 µm (green/red filter).

2) A medium resolution (R ≈1500) integral-field spectrograph, operating between 51 and 210 µm, with a velocity resolution of 75–300 km s^{-1} and an instantaneous coverage of ≈1500 km s^{1} over a field of view of 47"x47".

The scientific rationale for the photometer and spectrometer design are given in Poglitsch et al. (2010), which also provides a good summary of the PACS instrument, capabilities, and observation techniques, with numerous references to relevant work. For a more technical guide to PACS, we refer you to the PACS Instrument Description Documents (IDD I is the easiest to read, II-III contain more technical descriptions of the components of the PACS instruments and can be found on the Herschel PACS Library pages). PACS consisted of two units (see Figure 1):

1) the cold focal plane unit (FPU) inside the Herschel cryostat on the payload module

2) the warm electronic unit on the Herschel service module

Both units were connected via a harness. The harness consisted of a cold part inside the cryostat vessel and a warm part outside. Care was taken in the arrangement of the warm harness to optimise electromagnetic compatibility (EMC), e.g. interference of the signals on the harness by electrical switching of the solar panels.

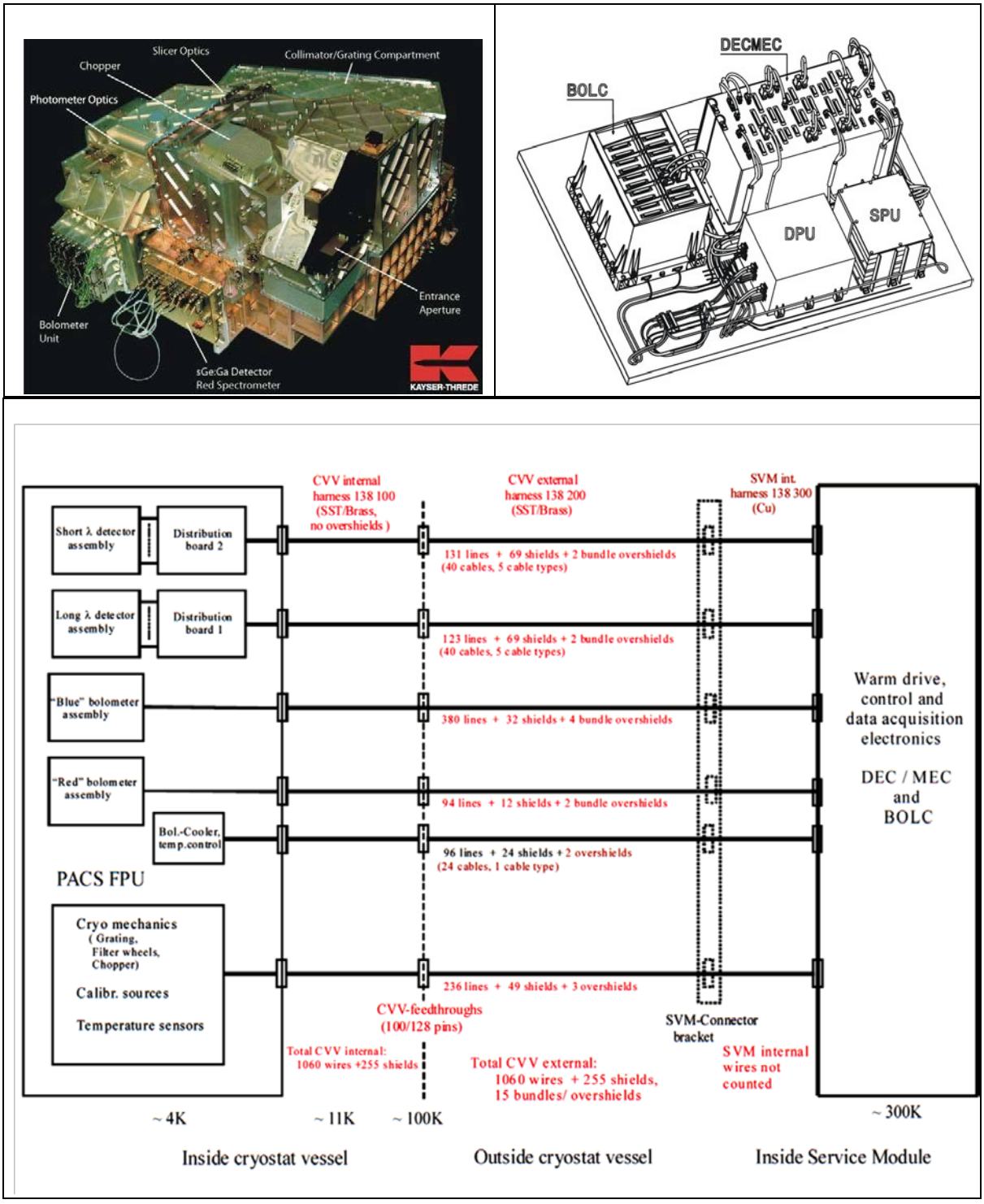

Figure 1: The main components of PACS. Top left: Cold FPU (T _4 K) assembled at Kayser-Threde, Munich, containing the optical elements and the detectors. Top right: Warm electronic boxes (T_300 K) with the on-board CPUs controlling the instrument and receiving engineering and science telemetry. The location of some elements is indicated. Bottom: A functional block diagram showing the components of the harness connecting the cold FPU inside the Herschel cryostat on the payload module with the warm electronic unit on the satellite service module.

6.2. Observing with PACS

Any observation with PACS (or any of the Herschel instruments) was performed following an Astronomical Observation Request (AOR) made by the observer. The AOR was constructed by the observer by filling in an Astronomical Observation Template (AOT) in the Herschel Observation Planning Tool, HSpot. Each template contained options to be selected and parameters to be filled in, such as target name and coordinates, observing mode etc. How to do this is explained in detail in the HSpot user's manual and the PACS Observer's Manual. The AOR content was subsequently translated into instrument and telescope/spacecraft commands, which were up-linked to the observatory for the observation to be executed. One special feature of PACS commanding was the use of On-board Control Procedures (OBCPs), command macros composed of a logical sequence of low-level commands needed to execute a certain type of observation, which were stored on-board. This reduced the telecommand bandwidth considerably, because only the name of the OBCP and the related parameters, whose values depended on the AOT parameter selection of the observer, had to be uplinked as part of the Mission Time-Line. The OBCPs were therefore essential elements of the AOT commanding design. A complete list of all PACS OBCPs and DEC/MEC sequences is given in Feuchtgruber et al. (2010) and is not germane to the discussion here.

The AOTs evolved in the first year of the mission as more efficient ways to carry out observations were created, so some of the standard AOTs used during the Performance Verification (PV) and Science Demonstration (SD) Phases (July–Dec, Oct–Dec 2009, respectively) were subsequently discontinued, and most were slightly changed.

Observations were made up of logical operations, such as configuring the instrument, initialisation, and science data-taking operations. These logical operations are referred to as building blocks (or just "blocks"). The science operations were usually repeated several times to achieve the requested SNR and/or to map a given sky area. Pipeline data reduction modules work on these building blocks under the hood. Since the noise of the bolometer readout system had a strong 1/f component, photometer observations were designed such that the signal was modulated with a frequency from 1 to 5 Hz to achieve optimum sensitivity. Signal modulation was possible either by using the focal plane chopper or by scanning with the whole telescope. In the pre-flight design of the PACS photometer AOTs (see Sauvage & Okumura, 2005), utilisation of the chopper was considered to be the more efficient. Besides a chop-nod point source AOT, a small-source AOT and a chopped-raster AOT were designed using a combination of telescope raster execution and chopping.

These three modes were tested during the AOT validation in the PV Phase, together with the scan map technique with the chopper mirror staring in the optical zero position. These AOT validation tests showed the scan map technique was superior to the chop/nod technique. Chopped small-source and raster mode were therefore abandoned and made inaccessible in the HSpot user interface and do not figure among the observing modes used for SSOs. The chop-nod point-source mode was maintained, because it provided accurate astrometry for the Herschel Pointing Calibration program (performed throughout the mission) and an independent reliable and low-cost observing method to test the photometer flux calibration consistency, while a few SSO science observations were also made in this mode before it was retired for general use and was used exclusively by the PACS ICC calibration team. Three photometer AOTs were fully validated and released to the observer community.

1) Point-source photometry with the chop-nod technique with the restrictions outlined above (see the "Point/Compact Source Observations: Mini-Scan Maps & Chop-Nod" release note).

2) Scan map technique, for large maps and for mini maps for point source photometry (see "Prime and Parallel scan mode" release note and the "Point/Compact Source Observations: Mini-Scan Maps & Chop-Nod" release note).

3) Scan map technique within the SPIRE/PACS parallel mode (see "Prime and Parallel scan mode" release note).

All photometer configurations performed dual band photometry with the possibility to select either the blue (60–85µm) or the green (85–125µm) band for the blue channel, and the red band (125–210µm) was always included. The two bolometer arrays provided full spatial sampling in each band.

6.3. Pipeline processing

Here we give the basics of PACS photometry pipeline processing. Extensive information is available in the references cited herewithin.

All Herschel observations were processed automatically by SPG (Systematic Product Generator) pipelines at the HSC, and placed in the HSA for users to download. In Section 8.4 the products found in these ObservationContexts are described, and in this chapter the pipelines that were run to create those products are explained. The SPG pipeline scripts together with a selection of interactive pipeline scripts can be found in HIPE. There are scripts provided for the various AOTs (observing modes) or for various science cases. The pipeline scripts are explained in full detail in the PACS Data Reduction Guide (PDRG) for spectroscopy and photometry. All pipeline scripts are run separately for the red and blue camera data, and in turn the ObservationContexts produced by the SPG contain data products of a red and blue variety – these are identified by an R or a B at the end of the product name (with a few exceptions, which have a G(reen) or contain both cameras and have no letter). All product names start with HPS (Herschel PACS Spectroscopy), or HPP (Herschel PACS Photometry).

For photometry there are several flavours of pipeline script offered, these using different mappers suitable generally for different types of source. Science-ready maps are produced with the highpass filter method (up to Level 2.5 products), JScanam and Unimap (up to Level 3 products), while MADMap maps can by generated by means of an interactive script. The SPG scripts can also be found in the Pipeline menu. Scripts to do photometry or convolution on the final products are offered in the Scripts menu within HIPE. We have chosen to use the Unimap products.

Unimap is a Generalized Least Squares (GLS) mapmaker developed in MATLAB and released by the DIET department of the University of Rome "La Sapienza" (Piazzo et al., 2015): the documentation can be found here, otherwise see the PDRG (phot). The Unimap interactive script reads Level 1 Frames and generates a map from the input obsids. The interactive script can be used for combining any number of obsids, while the standard processing concerns the combination of only two obsids (scan and cross-scan). Unimap performs a pre-processing to clean the data of systematic effects (offsets, drifts, glitches), and it uses the GLS algorithm to remove the correlated 1/f noise while preserving the sky signal over large spatial scales. The GLS estimator provided by Unimap can introduce distortions at the positions of bright sky emission, especially if point-like. The distortions, which generally appear as

cross-like artefacts, are due to the approximations of the signal model and to an imperfect compensation of disturbances at the pre-processing stage.

The pixel size for the final map in chosen in arcsec. The values used for the SPG are 1.6" for non-parallel blue observations and for 3.2" otherwise. Before moving further, all the scans and cross-scans are merged into a single structure. At this point, the time streams are still affected by some residual drift. To fully remove this remaining correlated noise, the following iterative loop is executed: at the start of the iterations, the current best-estimated map is generated, back-projected and subtracted from the timelines; then the residual drift is fit with a baseline (i.e. a first order polynomial) and subtracted from the timelines; a new map is created. The procedure is repeated for a user-selected number of iterations (by default set to 5). With the removal of the global drift (i.e., the correlated noise), the MADmap pre-processing is complete. Next, a deglitching is performed. The reason why glitches are removed only at this stage is that it is much easier to perform this operation once the global correlated drift is corrected for.

6.4. Data products used

The reader is referred to Exter (2018) for a detailed description of PACS products. A brief summary is shown in Figure 2.

Folder	Sub-folder	Filename pattern	Description
browseImageProduct		hpacsbrowseimage_<NNN>	The postcard
browseProduct	blue_Jscanam_map	hpacs_25HPPJSMAPB_blue_<RA>_<DEC>_00_v1.0_<NNN>	Level 2.5 SBP
	blue_Jscanam_map	hpacs_25HPPJSMAPB_green_<RA>_<DEC>_00_v1.0_<NNN>	
	red_Jscanam_map	hpacs_25HPPJSMAPR_<RA>_[p|m]<DEC>_00_v1.0_<NNN>	
	blue_projected_map	hpacs<OBSID>_20hppmapb_00_<NNN>	Level 2 SBP
	red_projected_map	hpacs<OBSID>_20hppmapr_00_<NNN>	
Level 0	HPPAVG<B|R> /herschel.pacs.signal.Frames	hpacs<OBSID>_00hppavb<b|r>s_00_<NNN>	timeline data
Level 0_5	HPPAVG<B|R> /herschel.pacs.signal.Frames	hpacs<OBSID>_05hppavb<b|r>s_00_<NNN>	timeline data
Level 1	HPPAVG<B|R> /herschel.pacs.signal.Frames	hpacs<OBSID>_10hppavb<b|r>s_00_<NNN>	timeline data
Level 2	HPPMAP<B|R>	hpacs<OBSID>_20hpppmap<b|r>_00_<NNN>	projected maps
Level 2_5	HPPHPFMAPB	hpacs_25HPPHPFMAPB_blue_<RA>_<DEC>_00_v1.0_<NNN>	projected maps
	HPPHPFMAPB	hpacs_25HPPHPFMAPB_green_<RA>_<DEC>_00_v1.0_<NNN>	(scan+cross-scan)
	HPPHPFMAPR	hpacs_25HPPHPFMAPR_<RA>_<DEC>_00_v1.0_<NNN>	
	HPPJSMAPB	hpacs_25HPPJSMAPB_blue_<RA>_<DEC>_00_v1.0_<NNN>	Jscanam maps
	HPPJSMAPB	hpacs_25HPPJSMAPB_green_<RA>_<DEC>_00_v1.0_<NNN>	(scan+cross-scan)
	HPPJSMAPR	hpacs_25HPPJSMAPR_<RA>_<DEC>_00_v1.0_<NNN>	
	HPPUNIMAPB	hpacs_25HPPUNIMAPB_blue_<RA>_<DEC>_00_v1.0_<NNN>	Unimap maps
	HPPUNIMAPB	hpacs_25HPPUNIMAPB_green_<RA>_<DEC>_00_v1.0_<NNN>	(scan+cross-scan)
	HPPUNIMAPR	hpacs_25HPPUNIMAPR_<RA>_<DEC>_00_v1.0_<NNN>	
Level 3	HPPJSMAP<B|R> and HPPUNIMAP<B|R>	same as Level 2.5 but "30" in place of "25"	multiple obsids combined

<RA> is the hour+minute, <DEC> is the <p|m>degree+arcminute. <NNN> is a timestamp. The SBPs provided are Level 2.5 maps unless only Level 2 is present. All observations have a red, and either a blue or green map, however only Level 2.5 includes the words "green|blue" in the name. The bands present at Level 3 depends on the common bands in the combined observations.

Figure 2: A summary table of PACS Products. Within this work we used the Unimap products, labelled HPPUNIMAPB/R).

Standard Level 2.5 data products from the HSA were used. These are fully-processed science-ready images that combine the scan and cross-scan into a calibrated map. PACS photometry data provides multiple products that are suitable for different purposes; we have chosen the UniMap product (see: http://infocom.uniroma1.it/unimap/ for more details) as the most suitable for this work. Readers are referred to Exter (2018) for details of these PACS products, their uses and limitations. The AORs used to generate this catalogue are listed in Table 1. In all cases, scan and cross-scan were concatenated, hence pairs of sequential ObsID numbers represent the scan and cross-scan for each filter at each epoch for each target.

The targets reported here were observed in two principal mapping modes with the PACS Photometer. Early in the mission and, for AORs that had been submitted and approved by HOTAC pre-launch, observations were made in small map mode, with the scan and cross-scan at 045º and 135º respectively, giving approximately square maps, as shown in the example shown in Figure 3.

1342186621	1342209005	1342227469	1342263832
1342186622	1342209006	1342227470	1342263833
1342198444	1342209384	1342231249	1342263834
1342198445	1342209385	1342231250	1342263835
1342199877	1342209386	1342231251	1342267433
1342199878	1342209387	1342231252	1342267434
1342203478	1342212281	1342250781	1342267443
1342203479	1342212282	1342250782	1342267444
1342207079	1342224492	1342255964	1342268982
1342207080	1342224493	1342255965	1342268983
1342209003	1342224494	1342255970	1342268984
1342209004	1342224495	1342255971	1342268985

Table 1: List of ObsIDs used in the generation of this catalogue.

As the mission progressed into routine operations, a new photometric mode was introduced that was principally for point source photometry, also used for mapping targets of modest size (typically no larger than ≈1 arcminute diameter). This was the mini-scan map mode in which short scans and crossscans were made at the so-called magic angles of 070º and 110º, providing a more efficient and clean combination of scan and cross-scan, giving a much more rectangular shape to the map when combined and giving much more homogenous coverage of the centre of the field of view. An example of a mini-scan map is shown in Figure 4.

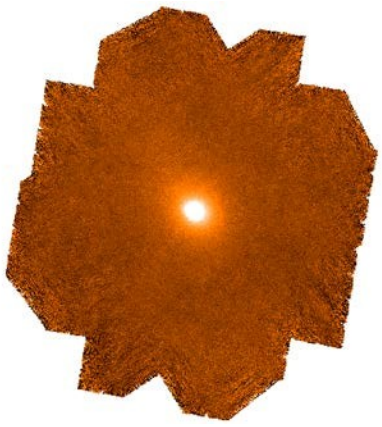

Figure 3: Example of a small map made by combining scan and cross-scan at angles of 045º y 135º. This is the 70 µm map of C/2006 W3 (Christensen) obtained by combining ObsIDs 1342186621 and 1342186622. As the map is the result of combining multiple individual scans, the map has ragged edges that reflect them.

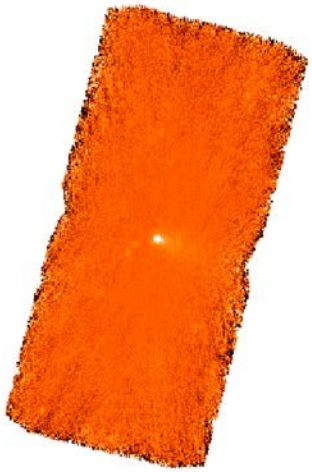

Figure 4: A typical mini-scan map, obtained by combining scan and cross-scan at angles of 070º and 110º. This is an image of 9P/Tempel 1 at 70 µm, obtained by combining ObsIDs 1342224492 and 1342224494. The shape of the map is strongly rectangular. As can be seen, coverage at the edges of the field is inhomogeneous and the direction of scan and cross-scan can be seen faintly in the noise.

6.5. Methods

For both weak point sources, for which PSF-fitting does not give satisfactory results and for active objects with an extent greater than the PSF the classic method of taking photometry is Aperture Photometry. This is the solution that we have adopted.

In its simplest form, aperture photometry consists of defining an aperture radius centred in the source that will contain all the pixels illuminated by it and determining the sky background by setting an annulus bigger than the aperture radius but close enough to share the same sky background properties, see Figure 5.

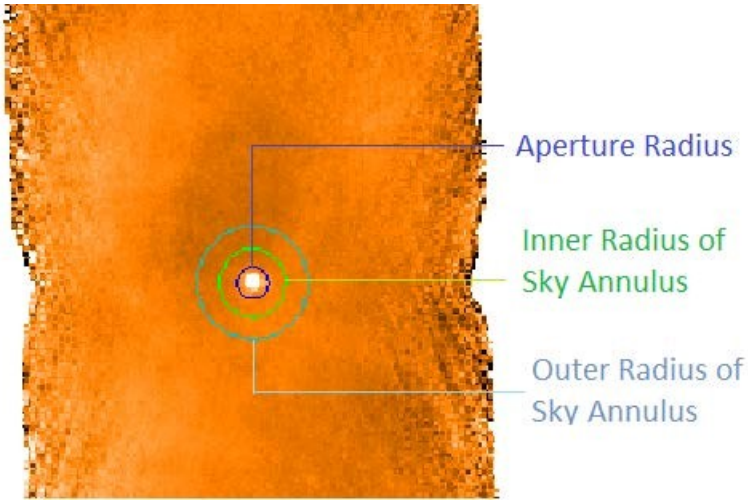

Figure 5: Aperture Photometry radii.

The main uncertainty to resolve is the question of how big these radii must be to produce optimal photometric data. There is no definitive answer for this, so extensive tests were undertaken to understand the effects of different choices. If a small aperture radius is chosen, not all of the pixels with flux from the observed body will be inside this radius and then the result will be to lose flux. In addition, for extended sources, we risk subtracting flux from the source that is included in the sky aperture should we define an annulus for the sky aperture that is too close to our target. But, on the contrary, if a very big radius is chosen for the photometric aperture, too many pixels will be included, with the addition of pixels that only serve to increase the sky noise and contamination (flux from background objects in the field that contaminates the flux of the target of interest), with the result that the flux will be a both too high and more uncertain than desired.

To select an optimum radius for the aperture for point sources, the point spread function (PSF) of the detector must be known. For Herschel the PSF is well characterised both for the telescope, through PACS imaging data (Geis & Lutz, 2010) and for the other instruments (HIFI: Muller et al., 2014; SPIRE: Ferlet, 2010). All the data that characterises fully the PSF is available through the Herschel Legacy Ancillary Data Product (ADP) pages. The PSF is the size and shape of the image of a point source on the detector. In general, it can be approximated by a Gaussian function and the angular size of the PSF is characterised by the FWHM, which is the value where the flux falls to half its central value. Since all of the celestial bodies that are being measured in the solar system, with the exception of the major planets, are considered point sources, obviously all of these objects will have the same PSF on the detector, independent of their brightness. Since the PSF has no edges, the intensity of the celestial body fades smoothly to zero with the increasing radius it is difficult to define a precise aperture radius suitable for all objects and all situations given the differences from object to object of flux, background, noise, possible background structure, etc.

The standard solution for the chosen value for the aperture radius for a point source is thus to select a scalar multiple of the FWHM (e.g. 1.4 x FWHM). Unfortunately, there is no single best solution. For bright sources, the use of a large photometric aperture is indicated to collect as much of the flux as possible, as missing flux is more of an issue for the s/n than background noise from a larger aperture. The use of a small aperture is recommended for faint sources, as it introduces the minimum quantity of background noise, thus maximising the s/n. Given that we must deal with sources that cover a huge range of fluxes from milliJansky to hundreds or thousands of Jansky and wish to employ a standard, self-consistent solution, a compromise must be found between the demands of different sources, we use a standard small photometric aperture as s/n is most critical for the faint targets. Evidently, as the aperture is small in relation to the area over which the flux is distributed, the aperture fails to sample the outer regions of the PSF, hence we have to add an aperture correction to compensate the missing flux. The aperture correction factor to apply is determined through careful signal-to-noise measurements of bright celestial bodies with different aperture radii and is detailed in the relevant instrument Handbooks (PACS: Exter et al., 2017; and SPIRE: Valtchanov, 2017).

For extended objects, this process of using a standard aperture and an aperture correction evidently breaks down, as significant flux may be extended far beyond what would be considered to be the limits of the PSF for normal usage. Similarly, the standard CCD recipe of taking the sky background from an annulus around the object ≈25% larger than a photometric aperture of 3-4*PSF is unsatisfactory as neither will the photometric aperture sample the full extent of the source, nor will the sky aperture be free of extended emission. What is worse is that frequently it is not obvious even how far out from the target centre of light the emission is present, so it is not a simple matter to fix an aperture size, nor a sky annulus.

The solution is to measure the flux of the comet within multiple apertures of different sizes and to use only the sky annulus corresponding to the largest aperture for the sky subtraction for all the apertures of whatever size.

For extended solar system objects – comets – there is also the not inconsiderable issue of the meaning of aperture photometry. Comets are at different distances and their distance both from the Sun and from the Earth changes constantly. Suppose we define a standard aperture of 60 arcseconds for measuring comets, we will encounter the following issues:

- For a distant comet, the entire coma may be much smaller than 60 arcseconds: all we would do is integrate noise and sky background. Similarly, for a comet making a close pass to Earth, or a very active object, the coma may be very much larger than 60 arcseconds: we will not sample the whole coma.

- A particular aperture diameter will correspond to a particular physical diameter at the comet. As the comet approaches the Earth, a fixed aperture diameter will correspond to an eversmaller *physical aperture at the comet*. Similarly, the same aperture diameter will correspond to a physical diameter at the comet three times as large for a comet at 3AU from the Earth as one at 1AU: we do not compare like with like, either when comparing comets or when following a single object at various epochs. As the comet gets closer to the Sun and the physical size of the coma grows, we will sample an ever-smaller region of it, meaning that parameters such as gas and dust production rates derived from photometry, refer to different regions of the cometary coma at different epochs.

Our solution, to measure in many apertures, allows us to make a fit to the coma radial profile and integrated calculate fluxes within any given physical aperture for any epoch following the process in Figure 6.

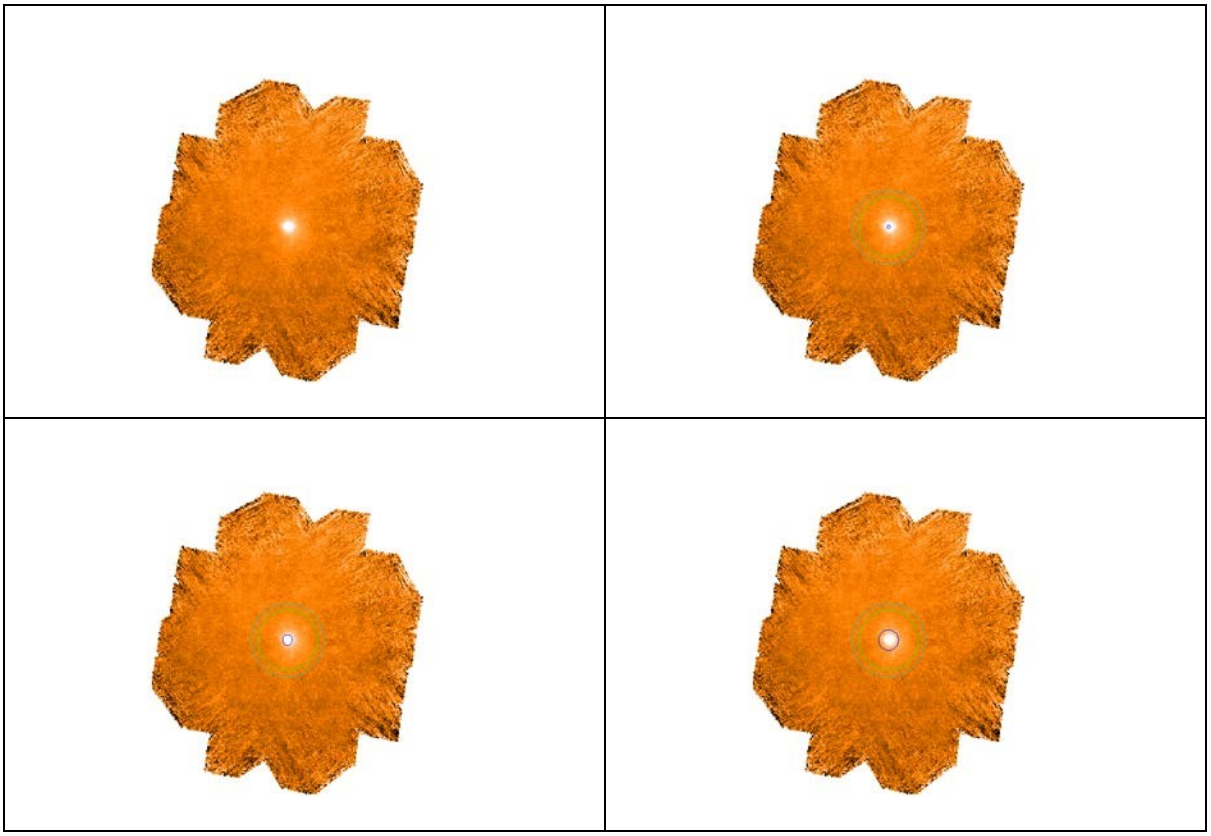

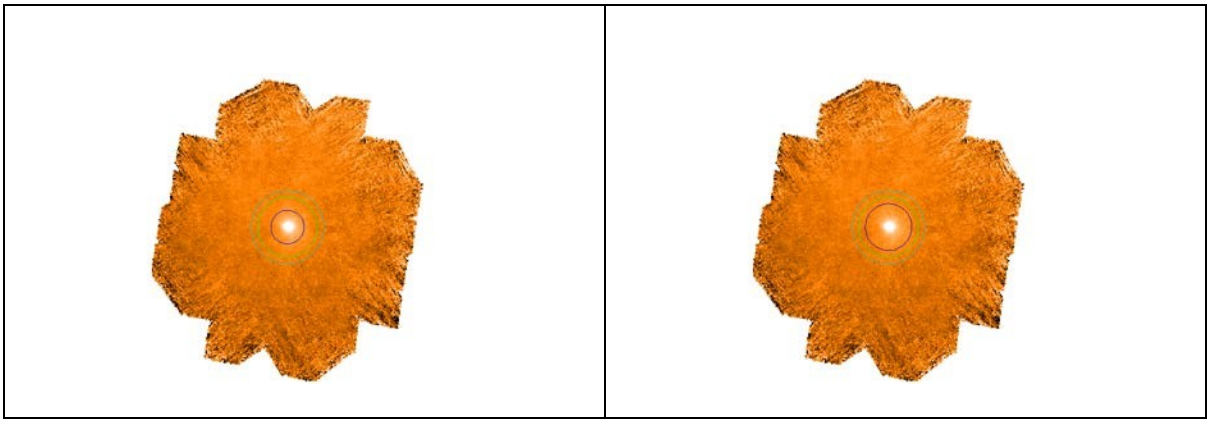

Figure 6: An example of aperture photometry as carried out in this work on C/2006 W3 (Christensen), 70 µm images. Top left – the original image; top right – the sky annulus used for all the apertures marked, along with a 5 arcsecond radius photometric aperture; middle left – same, with a 10 arcsecond photometric aperture; middle right – same with a 30 arcsecond photometric aperture; bottom left – same with a 50 arcsecond physical aperture; bottom right – same with a 70 arcsecond physical aperture. At the epoch of observation, 10 arcseconds corresponded to 26000 km at the comet.

We obtain the curve of growth of the coma flux and can fit a power law to the linear part of the curve, taking into account that the smallest radius may be affected by the PDF, causing flux losses and the largest may no longer be integrating coma. The resultant curve of growth for the example shown in Figure 6 is shown in Figure 7. From the fit, we can calculate the flux for any aperture size at the comet although, evidently, we should only carry out this exercise by interpolation and not by extrapolation to aperture sizes outside the range measured. As an example, we show the position of two sample physical aperture sizes corresponding to a physical *diameter* of 50000 km and 200000 km at the comet. We can see that, even at a heliocentric distance of 3.3 AU, the physical size of the coma detectable by Herschel was ≈$3x10^5$ km: slightly smaller than the radius of the Moon's orbit.

Figure 6 and Figure 7 illustrate the problem in defining the coma size. With normal stretch, in Figure 6 we see that the visible coma of this large, extended object does not even completely fill an aperture of radius 30 arcseconds. However, extreme stretches show that even the PSF pattern for PACS at 70 µm extends several arcminutes out from the centre of the image (Geis & Lutz, 2010). When we integrate the flux within apertures of increasing size out to 75 arcseconds Figure 7, we see that light losses are significant in the smallest aperture radius, even though we have applied the aperture correction determined for the instrument PSF to, in theory, correct for such light losses while, beyond 60 arcseconds, the curve of grown flattens significantly, suggesting that the limit of the coma has been reached. There is a danger though that, if the sky radius is set too small – i.e. only slightly larger than the largest photometric aperture – we will practice cannibalism, subtracting coma flux from coma flux. However, if the sky annulus is made too large, we may (a) introduce errors by calculating the sky too close to the edge of the map, allowing edge effects to influence and (b) introduce flux from other sources in the field of view and (c) measure a mean sky background that is unrepresentative if there are second order gradients present across the field, as the assumption that a linear interpolation of sky brightness gradients across the aperture is valid, breaks down. The larger the sky annulus, the greater the danger that, in particular, the second of these assumptions may break down.

The optimum annulus size can only be established by trial and error. For maps with a relatively large size, we have been able to use large sky annuli; where we see that the curve of growth flattens well before reaching the largest photometric aperture, the sky annulus can be reduced in size. Where the

map is small, we have to make the sky annulus as large as is compatible with falling entire within the area of even sky coverage of the map, avoiding edge effects.

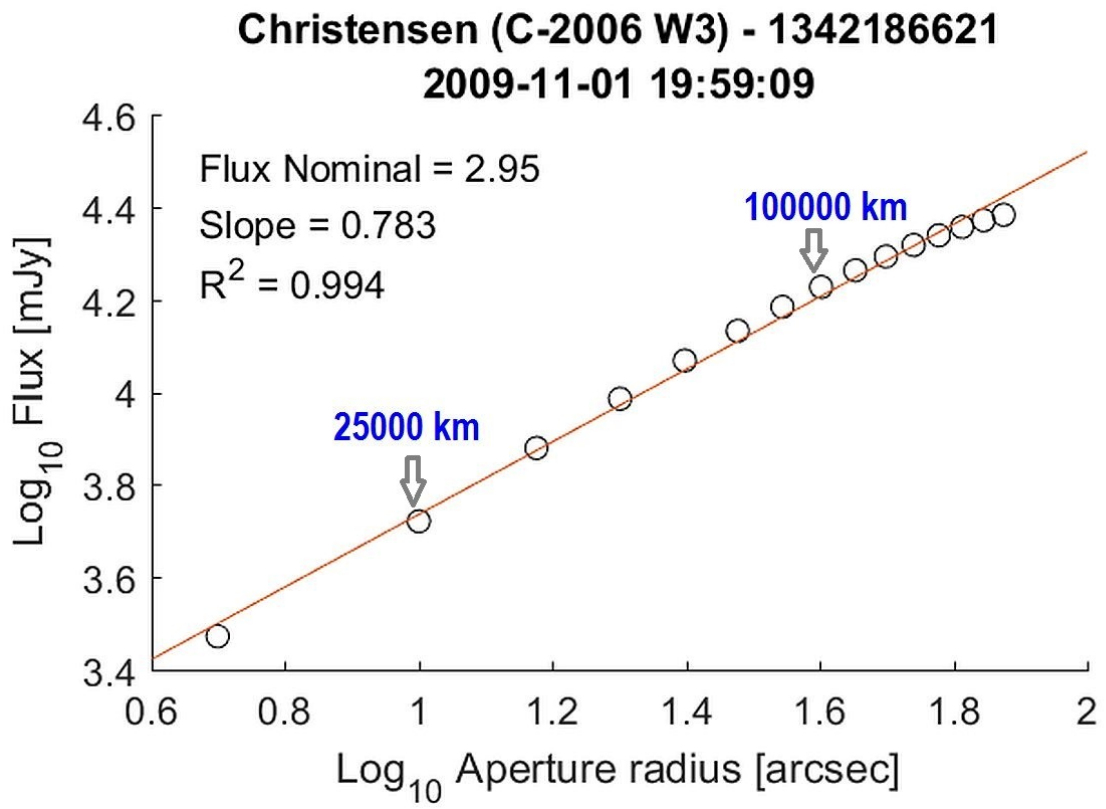

Figure 7: An example of the curve of growth obtained from the photometry shown in Figure 6. Each point is a measure in a photometric aperture of radius from 5 to 75 arcseconds, at steps of 5 arcseconds. A least squares power law fit is drawn through the data. We see that the curve of growth flattens-out considerably beyond a radius of 60 arcseconds, indicating that the limit of the coma has been reached, although this plot also illustrates the difficulty in defining the exact physical radius of the coma as, logically, there is no exactly defined limit. We also see that the innermost radius of 5 arcseconds is slightly below the line too, indicating flux losses due to the radius of the PSF being significant compared to the photometric aperture. We add the position of a radius corresponding to 25000 km and to 100000 km at the comet, in each case, marked with an arrow.

We find that large and relatively high activity comets such as C/2006 W3 (Christensen), or C/2009 P1 (Garradd), the coma is typically $>10^5$ km while, for low-activity, Jupiter family comets, the coma diameter is typically $<5x10^4$ km in the Herschel/PACS data. One of the issues that we have found is finding a characteristic physical aperture size that is valid for all comets within our sample for the purposes of comparison of the activity of different objects.

6.6. Cautionary Notes

The primary goal of the catalogue is to provide information of high quality and reliability that may be used "as presented" for scientific studies. Detailed information on the description of the data, methodology and quality assessment can be found in Romero Calvo (2018, Masters Dissertation, Technische Universität, Berlin, Fakultät VI, IGG).

Here below we discuss some of the limitations on the data and, as important, on the scheduling of the objects described.

6.7. Scheduling restrictions

Herschel's ability to observe solar system targets was limited by a series of scheduling restrictions. The most important to consider were the following.

6.7.1. Solar Elongation (aka Solar Aspect Angle)

In particular, targets had to be located between a solar elongation (usually referred to as Solar Aspect Angle - SAA) of 60°.8 and 119°.2. Targeting was thus not possible for objects close to opposition, or to perihelion. In addition, there was a range of Solar Aspect Angles at which it was known even prior to launch, that the service module could be heated by direct sunlight and so the telescope's pointing performance could be compromised. Initially, this range, known as "hot betas", or hot beta angles, was set such that pointings were restricted from Solar Aspect Angles from 110° to 119°.2. However, as the mission progressed and knowledge of the pointing performance of the satellite improved, it was realised that heating of the baseplate of the star trackers was affecting pointings at Solar Aspect Angles smaller than 110° and that this effect restricted scheduling at an additional range from 105° to 110° too.

Save in special cases[1], at all times during the mission, pointings within the hot beta range were limited to short excursions, each of which was studied on a case-by-case basis by the Spacecraft Environment Scientist before being approved (or not) for scheduling. Restrictions on excursions into the hot range were tightened progressively, as their effects became better quantified and, in the last third of the mission were limited typically to a maximum of an hour, strongly discouraged at the hottest end of the Solar Aspect Angle range and only permitted at the end of an OD to allow the Service Module to cool during the Daily Telecommuncations Period with the ground station, during which the Service Module was always in a cold configuration.

These pointing restrictions had a significant impact on the scheduling of some of the objects listed here and made the scheduling of other potential SSO targets, impossible. Any object making a close pass to Earth *outside* the Earth's orbit would be close to the opposition point and either unschedulable or, at best, at hot betas when best-positioned for observation. Evidently, when a comet was closest to perihelion and thus brightest, it was usually outside the permitted range of SAA and thus unobservable, although on the cold side and thus could be observed without limitations up to the SAA limit. For other objects that were outside the Earth's orbit, observation was only possible when at least 60° from the opposition point and, later in the mission, >75° and thus at a much greater herschelcentric distance than when close to opposition, implying lower fluxes and lower s/n for the same length of integration and lower physical resolution at the comet.

6.7.2. The Instrument sub-schedule

A second, important consideration was the need to encompass SSO observations, with their often limited periods of visibility, efficiently within the overall observing schedule. The schedule was

[1] A typical case would be the need to orientate the service module towards hot beta angles for instrument recovery activities, maintaining this orientation for as much as two full operational days, during which time only pointing-robust observations (typically, large maps) would be scheduled.

prepared as a series of two-week – fourteen Operational Day (OD) – cycles, within which the different instruments were allocated particular blocks of time according to demand. As a rule of thumb, more spectroscopy was scheduled at times when the Galactic Centre was visible, while a higher proportion of photometry was scheduled at times when the Galactic Poles were visible.

Of the seven sub-instruments, four (PACS Photometry, SPIRE Photometry, SPIRE PACS Parallel Mode and SPIRE Spectroscopy) required a cooler re-cycle to be completed before observing and their observing blocks were limited in duration by the cooler hold time: typically, 2 ODs for SPIRE and 2.5 ODs for PACS Photometry. Efficient use of helium was primordial in scheduling.

Scheduling of SSOs was not permitted by SPIRE PACS Parallel Mode, while PACS photometry was scheduled in 2.5 OD blocks, for efficiency of helium use, with the extra 0.5 ODs at the end of a cooler hold scheduled as PACS Spectroscopy or, occasionally, as HIFI. Although as many as three PACS Photometry blocks could be concatenated, they were always punctuated by periods of at least 0.5 OD when PACS photometry was not available. Similarly, for most of the mission, SPIRE Photometry was rarely ever scheduled for more than two ODs in any scheduling cycle and, by the end of the mission, with a highly depleted pool of observations available for scheduling, not all scheduling cycles even included 1 OD of SPIRE Photometry (blocks of 1 OD of SPIRE Photometry would be combined with SPIRE Spectroscopy to form a 2 OD block that would use the SPIRE cooler efficiently). These limitations were important when several observations of an SSO needed to be scheduled within a particular interval of time.

6.7.3. Tracking rate restrictions

For SSOs making a close approach to Earth, an important consideration was the differential tracking rate required. Initially Herschel was limited to a maximum differential tracking rate of 10”/minute. As knowledge and confidence in the performance of Herschel increased, this was relaxed to 30”/minute. This though still limited Herschel’s ability to observe objects making approaches to within ≈20 Lunar Distances (LD) of the satellite.

6.7.4. Ephemeris restrictions

In theory, Herschel could react in an ideal case in 4-5 days to a Target of Opportunity (ToO) alert, such as a newly discovered bright comet or a Near Earth Object. In practice, to be able to schedule observations, it was necessary to include an ephemeris for the target in the Herschel Uplink database. During approximately the first half of the mission this required a complete new build of the Herschel Proposal Submission software, incorporating the newly added ephemeris file(s). The preparation of a new build typically added 3 days to the turnaround time in reacting to a ToO alert. Additionally, for newly discovered objects, it could take several days before a sufficiently accurate ephemeris to permit telescope scheduling was available. This meant that, on some occasions, the visibility window of a SSO ended before an observation could be scheduled.

7. Catalogue description

7.1. Contents

The catalogue contains the following elements:

1. Tables of aperture photometry for multiple aperture diameters for each comet and ObsID.

2. Fits to integrated coma radial flux profile – log10 Flux(mJy) = Slope * log10 Aperture radius (arcsec) + constant, where the constant term would be the extrapolated flux in mJy in a 1 arcsec radius.

3. Integrated fluxes in mJy in standard physical aperture diameters at the comet of 10^3, $2.5x10^3$, $5x10^3$, 10^4, $2.5x10^4$, $5x10^4$ and 10^5km, calculated from the fit to the coma aperture photometry.

Additionally, and as ancillary data, we provide:

4. Curves of growth of the integrated coma radial flux presented as $\log_{10}$ Flux(mJy) against $\log_{10}$ Aperture radius (arcsec).

5. Images of the comets observed, for each filter and epoch of observation, in the standard astronomical orientation of North up and East to the left.

6. Complementary visible CCD imaging at an epoch or at epochs as close as possible to the Herschel observations to give context for the Herschel data.

7.2. Description of the catalogue

This is provided in ASCII as a CSV file, named “Active Comet Catalogue.csv” with the final aperture photometry data for each comet at each epoch. Below, we describe the column headings used and a description of contents.

7.2.1. Listing of column headings used

The column headers used in the catalogue are the following:

ObsId, Target IAU, Target, NAIF ID, WL, MapScanVel, LevProd, map, RA_fit, DEC_fit, rap, risa, resa, Flux_pre, Flux_ApC, Flux_CC, Mean Flux, Temperature, CC_Factor, spgVersion, StartTime, Radius 1 ("), Radius 2 ("), Intercept, Slope, Radius 1 (km), Radius 2 (km), Flux 10^3Km, Flux 2.5x10^3Km, Flux 5x10^3Km, Flux 10^4Km, Flux 2.5x10^4Km, Flux 5x10^4Km, Flux 10^5Km, Flux (Radius 1), Flux (Radius 2).

7.2.2. Description of contents of columns

7.2.2.1. ObsID

The ObsID within the HSA of the AOR that has been processed. Note that the products used are always the combination of two ObsIDs while, if there are products for both 70 and 100 µm, the photometry at 160 µm will be obtained from the combination of four ObsIDs. Similarly, if two observations were taken during the same OD using exactly the same instrumental configuration, as was the case on one occasion for C/2009 P1 (Garradd), the photometry presented will be the mean of the combination of all the ObsIDs in this configuration that were taken on that OD.

7.2.2.2. Target IAU

The official IAU designation for the target according to the system as defined by the IAU Minor Planet Center. The rules for designations are given here:

https://www.minorplanetcenter.net/iau/lists/CometResolution.html

7.2.2.3. Target

The target name as defined in the observing log and thus associated with the ObsID. This is the target name used when the proposal was submitted and approved by HOTAC and thus the target name that appears in the Uplink database.

7.2.2.4. NAIF ID

NAIF is the Navigation and Ancillary Information Facility, used by SPICE. The Navigation and Ancillary Information Facility (NAIF), acting under the directions of NASA's Planetary Science Division, has built an information system named "SPICE" to assist NASA scientists in planning and interpreting scientific observations from space-borne instruments, and to assist NASA engineers involved in modelling, planning and executing activities needed to conduct planetary exploration missions. The use of SPICE, which derives from it functions (**S**pacecraft ephemeris; **P**lanet, satellite, comet or asteroid ephemeris; **I**nstrument information; orientation information – the transformation provided by the so-called **C**matrix, which provides time-tagged pointing information; and **E**vents information – planned and unplanned mission activities), extends from mission concept development through the post-mission data analysis phase, including help with correlation of individual instrument data sets with those from other instruments on the same or on other spacecraft. The primary SPICE data sets are often called "kernels", or "kernel files." SPICE kernels are composed of navigation and other ancillary information that has been structured and formatted for easy access and correct use by the planetary science and engineering communities.

The NAIF ID is a unique identifier for solar system objects, both natural and artificial that allows a target to be linked to an ephemeris. This is increasingly used in ground-based observatories too to facilitate the observations of solar system targets. Information on NAIF IDs and their use can be found here: https://naif.jpl.nasa.gov/pub/naif/toolkit_docs/FORTRAN/req/naif_ids.html

7.2.2.5. WL

Wavelength of the observation associated with the ObsID. Permitted values are “blue1” (70 µm), “blue2” (100 µm) and “red” (160 µm). All PACS ObsID are associated with two independent data products, corresponding to the simultaneously observed blue channel (blue 1, or blue 2) and red channel.

7.2.2.6. MapScanVel

The scan velocity for the map. Permitted values are 10 arcseconds/second, 20 arcseconds/second and 60 arcseconds/second, corresponding to “slow”, “nominal” and “fast”. The slow scan rate was deprecated early in the mission, but some comet data was taken in this mode.

7.2.2.7. LevProd

The level of product used. In all cases of active comets, the product was Level 2.5, corresponding to combination of scan and cross-scan.

7.2.2.8. Map

The data product used from the list of products provided (see Figure 2). We have used the UNIMAP product, i.e. the map, combining scan and cross-scan, produced by Unimap.

7.2.2.9. RA Fit

The Right Ascension of the fitted astrometric position for the target, measured from the map product. This may differ significantly from the position obtained from the ephemeris file used in product generation and from the map centre.

7.2.2.10. Dec Fit

The Declination of the fitted astrometric position for the target, measured from the map product. This may differ significantly from the position obtained from the ephemeris file used in product generation and from the map centre.

7.2.2.11. rap

The radius of the photometric aperture in arcseconds.

7.2.2.12. risa

Radius in arcseconds of the inner edge of the sky aperture ring.

7.2.2.13. resa

Radius in arcseconds of the outer edge of the sky aperture ring.

7.2.2.14. Flux_pre

Raw flux in milliJansky within the photometric aperture after sky subtraction, before any corrections are applied.

7.2.2.15. Flux_ApC

Aperture corrected flux in milliJansky. Here we apply the standard aperture correction for the instrument taken from Table 5.4 of the PACS Handbook (Exter et al., 2017).

7.2.2.16. Flux_CC

The colour-corrected flux in milliJansky calculated by applying the correction factor obtained from Tables 5.5-5.7 of the PACS Handbook (Exter et al., 2017).

7.2.2.17. Mean Flux

This is the flux in the aperture in milliJansky, averaged over the different map products where more one than one product was produced for a single target and filter on a single OD.

7.2.2.18. Temperature

This is the greysphere temperature assumed for the body when calculating the colour correction.

7.2.2.19. CC_Factor

This is the colour correction factor applied to the raw flux. The raw flux is divided by this factor to obtain the colour corrected flux.

7.2.2.20. spgVersion

This is the pipeline product version number used. Version 14.2 corresponds to the final bulk reduction of the Herschel archive and represents the state of the art in data reduction.

7.2.2.21. StartTime

The start time for the integration.

7.2.2.22. Radius 1 (")

This is the radius of the smallest aperture used for the least squares fit to the curve of growth.

7.2.2.23. Radius 2 (")

This is the radius of the largest aperture used for the least squares fit to the curve of growth.

7.2.2.24. Intercept

This is the value of the constant term, a, in the power law fit:

$$F_x = a \cdot x^b \qquad (1)$$

Where F_x is the total flux in milliJanskies in an aperture of radius x arcseconds.

In physical terms, “a” corresponds to the total flux in milliJansky that would be measured in a notional aperture of 1 arcsecond diameter.

7.2.2.25. Slope

This is the exponent term in Equation (1) and represents the slope of the power law fit to the curve of growth.

7.2.2.26. Radius 1 (km)

The physical distance in kilometres at the comet that corresponds to the smallest aperture radius used for the least squares fit to the curve of growth. To calculate the physical diameter of the aperture at the comet, multiply this value by a factor of two.

7.2.2.27. Radius 2 (km)

The physical distance in kilometres at the comet that corresponds to the largest aperture radius used for the least squares fit to the curve of growth. To calculate the physical diameter of the aperture at the comet, multiply this value by a factor of two, which would then correspond to the calculated physical diameter of the coma at the epoch of observation for this wavelength.

7.2.2.28. Flux 10^3km

The calculated integrated flux in milliJansky within a physical aperture at the comet of radius 10^3km, obtained from the fit to the curve of growth.

7.2.2.29. Flux 2.5x10^3km

The calculated integrated flux in milliJansky within a physical aperture at the comet of radius $2.5x10^3$km, obtained from the fit to the curve of growth.

7.2.2.30. Flux 5x10^3km

The calculated integrated flux in milliJansky within a physical aperture at the comet of radius $5x10^3$km.

7.2.2.31. Flux 10^4km

The calculated integrated flux in milliJansky within a physical aperture at the comet of radius 10^4km, obtained from the fit to the curve of growth.

7.2.2.32. Flux 2.5x10^4km

The calculated integrated flux in milliJansky within a physical aperture at the comet of radius $2.5x10^4$km, obtained from the fit to the curve of growth.

7.2.2.33. Flux 5x10^4km

The calculated integrated flux in milliJansky within a physical aperture at the comet of radius $5x10^4$km, obtained from the fit to the curve of growth.

7.2.2.34. Flux 10^5km

The calculated integrated flux in milliJansky within a physical aperture at the comet of radius 10^5km, obtained from the fit to the curve of growth.

7.2.2.35. Flux (Radius 1)

The calculated integrated flux in milliJansky within a physical aperture at the comet of radius equivalent to the minimum radius used to calculate the fit to the curve of growth, obtained from the fit to the curve of growth.

7.2.2.36. Flux (Radius 2)

The calculated integrated flux in milliJansky within a physical aperture at the comet of radius equivalent to the maximum radius used to calculate the fit to the curve of growth, obtained from the fit to the curve of growth.

7.3. Description of files provided

7.3.1. Aperture photometry images and graphics

For each ObsID we provide the processed Level 2.5 images used to obtain the photometry and the images with photometric apertures used overplotted (for examples, see Figure 10, Figure 11, Figure 12 & Figure 13). The structure of the filenames is:

- Processed level 2.5 image with no overplotted graphics

ObsID-ApertureSize-Product: for example, 1342186621-50.0-HPPUNIMAPR-ApPhot, where the aperture radius is in arcseconds, HPPUNIMAPR declares that the Herschel PACS Photometry product used is the one from Unimap in the Red channel (160 µm).

- Processed level 2.5 image with overplotted photometric aperture

ObsID-ApertureSize-Product-ApPhot: for example, 1342186621-50.0-HPPUNIMAPR-ApPhot, where "ApPhot" is the aperture radius is in arcseconds, HPPUNIMAPR declares that the Herschel PACS Photometry product used is the one from Unimap in the Red channel (160 µm).

- Grid of points used for flux error determination

ObsID-ApertureSize-Product-Stdv-F: for example, 1342186621-50.0-HPPUNIMAPR-Stdv-F, where "ApPhot" is the aperture radius is in arcseconds, HPPUNIMAPR declares that the Herschel PACS Photometry product used is the one from Unimap in the Red channel (160 µm) and Stdv-F is the

standard deviation of the background flux. To estimate the error in the measured flux we used a process whereby the sky apertures around the source were placed in a 9x9 grid, with an interval of 5 pixels and centred on the fitted coordinates of the source. The "Annular Sky Aperture Photometry" task was used then in HIPE, with the same aperture size as the one used for calculating the flux in band.

- Grid of points used for flux error determination after sigma clipping

ObsID-ApertureSize-Product-Stdv-1stIt: for example, 1342186621-50.0-HPPUNIMAPR-Stdv-1stIt, where "ApPhot" is the aperture radius is in arcseconds, HPPUNIMAPR declares that the Herschel PACS Photometry product used is the one from Unimap in the Red channel (160 μm) and Stdv-1stIt is the standard deviation of the background flux after clipping apertures that deviate by more than 2σ (potentially contaminated with background sources, or with un-corrected bad pixels). Any aperture that deviated by more than 2σ was suppressed for the calculation of the flux in band. Grid of fluxes used for flux error determination after sigma clipping

ObsID-ApertureSize-Product-Plot: for example, 1342186621-50.0-HPPUNIMAPR-Plot, where "ApPhot" is the aperture radius is in arcseconds, HPPUNIMAPR declares that the Herschel PACS Photometry product used is the one from Unimap in the Red channel (160 μm) and Plot is the plot of the measured sky flux after clipping sky apertures that deviate by more than 2σ. An example of how sky apertures would be excluded from the calculation due to containing a background source is shown in Figure 8.

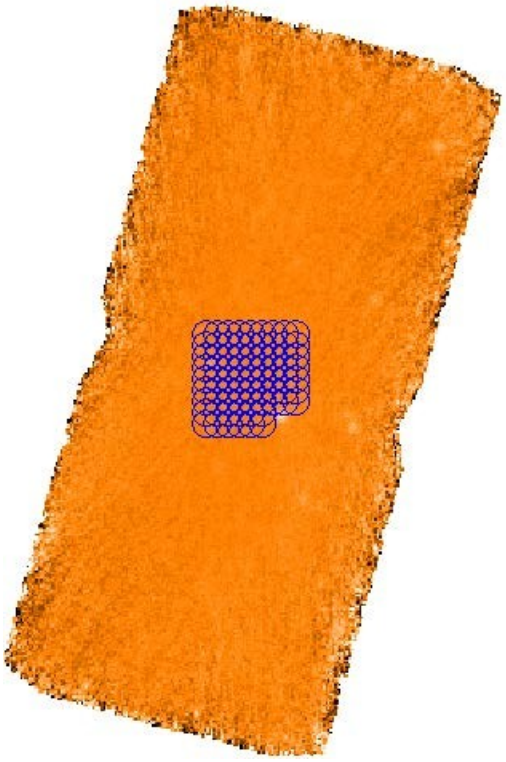

Figure 8: An example of Flux STD calculation - grid after exclusion of apertures. Observation: 2001 QX322 - ObsID: 1342211621 - HPPUNIMAPB. NB: this is a point source, not included in this volume and included for illustrative purposes only. We see that various apertures around a bright background source are clipped-out in the final calculation of the sky mean and standard deviation.

7.3.2. Visible images

For each comet we provide visible CCD images that give ground-based context for the Herschel data. Normally this is in the form of two CCD images taken at or close to the epoch of the Herschel observation, selected from the large pool of images provided by the observers in the "Observadorescometas" network. The images are selected to be not just simultaneous, or near-simultaneous with the Herschel observations, but to have an image scale and depth that provide adequate context for the Herschel data. In some cases, the image may refer to an epoch more distant from the Herschel data if the comet did not show major changes in the intervening time and no suitable nearsimultaneous image was available due to source observation geometry.

The structure of the filename is:

ObsID, Comet name, date of image (yyyymmdd), IAU site code of observatory that provided the image. A typical example is 1342263835-29P-130129-213.png.

IAU site codes and ancillary information are listed in the url https://www.minorplanetcenter.net/iau/lists/ObsCodesF.html. Additional information on the images are given in the notes on each comet provided in this volume.

Figure 9: A typical CCD image taken quasi-simultaneously with the Herschel data, which we use to provide context for the Herschel observations. In this case we show an image of 45P/Honda-Mrkos-Pajdusakova obtained on 2nd October 2011 by Ramón Naves and Montse Campàs from IAU Site Code 213 (Barcelona, Spain).

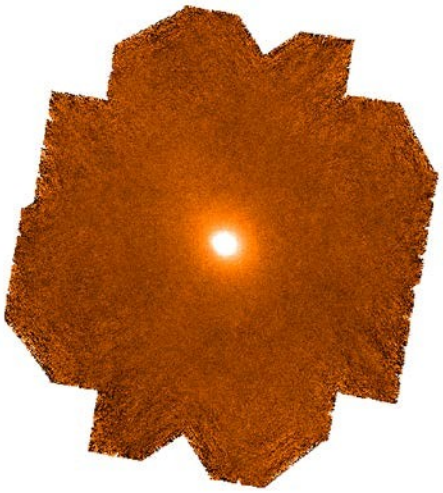

Figure 10: Sample image of C/2006 W3 (Christensen) at 70 μm showing the extended coma and a faint tail extending towards the north-east.

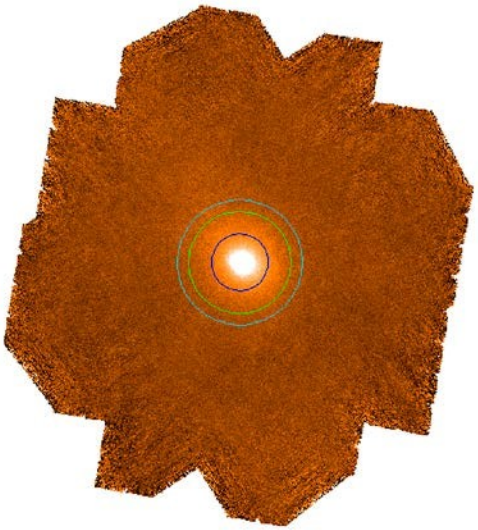

Figure 11: The same image as Figure 10 with a 50 arcsecond diameter aperture overplotted (blue circle). The HIPE apphot task automatically selects an annulus for the sky background although, in many cases, it is within the extended coma, so we do not use it, preferring to use a more distant aperture instead.

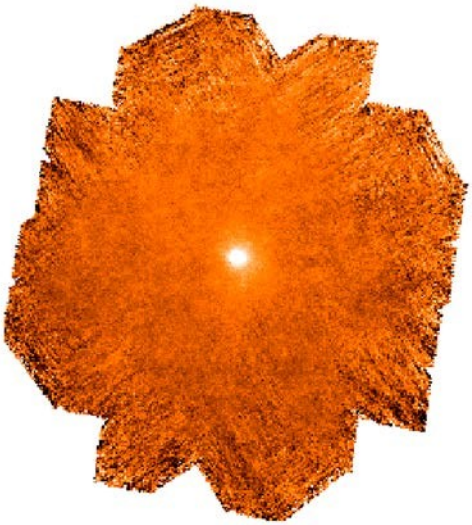

Figure 12: The corresponding image of C/2006 W3 (Christensen) at 160 μm for the simultaneous 70 μm image shown in Figure 10.

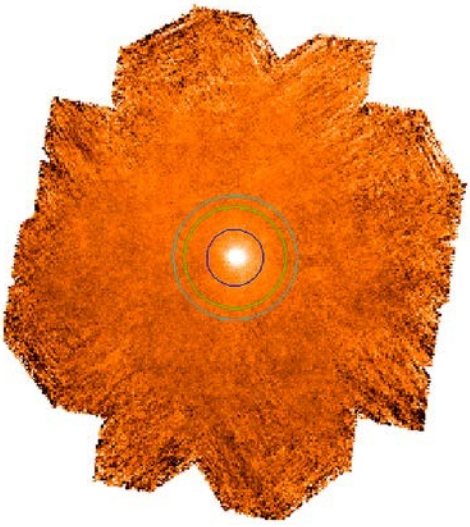

Figure 13: The same image as Figure 12 with a 50 arcsecond aperture overplotted.

7.3.3. Graphics-FluxVsRadii

In these graphics, we show the log Flux in milliJansky against log aperture radius in arcseconds along with the least squares power low fit for each ObsID and each filter. The structure of the filename is ObsID_TargetName_ band. The TargetName is as was defined in the proposal, so may bear little relation to the official IAU designation. The band is "blue1" (70 µm), "blue2" (100 µm), or "red" (160 µm). We show the least squares fit to the points, the nominal flux (i.e. intercept, which is equivalent to the flux in a 1 arcsecond radius aperture), the slope (exponent) and the correlation coefficient (as r^2). The fit can be expressed as Flux = intercept * radius^{slope}. A sample plot is shown in Figure 14.

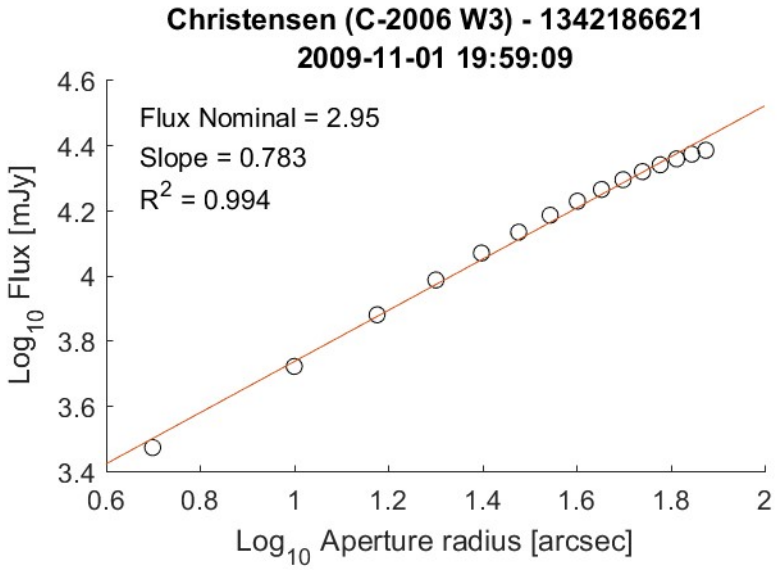

*Figure 14: A sample plot of flux against aperture radius. The plot title gives the target name, ObsID and the start time of the observation. The least squares fit is intercept * radius^{slope}. The intercept (nominal flux) is the flux that would be measured in a nominal 1 arcsecond radius aperture. In this case we can see clearly that the total flux is trending exponentially to a limiting value at the largest aperture radii.*

7.3.4. Coma profiles from visible CCD imaging

For each comet we also give a plot of the evolution of fit to the visible coma with heliocentric distance. This plot shows the variation of the slope of the power law fit to the integrated magnitude in R for apertures from 10-60 arcseconds against the heliocentric distance. The red, horizontal line marks the slope expected if the coma brightness shows an ideal 1/r dependence with distance from the nucleus (sometimes expressed also as 1/ρ): points above the line indicate a coma that falls off more steeply than 1/r – i.e. the coma is more concentrated than 1/r, or is point-like – while points below the line are more extended than an ideal 1/r coma – i.e. the coma is more diffuse. Radial brightness profiles versus radius for 14 comets including 67P/Churyumov-Gerasimenko (Baum et al., 1992) show that

[2] The full IAU designation and its explanation is as follows: nnnP or nnnP/name, for numbered periodic comets, C/yyyy** for unnumbered objects, where the initial letter indicates the type of object – "P" for an unnumbered periodic comet, "C" for non-periodic comet [additional designations, not applicable to objects in this work are "X" for a comet with only an approximate orbit not suitable for ephemeris generation, "D" for a disappeared or lost comet and "I" for an object that originated in interstellar space].

about half their observed comets follow a 1/r fall off quite closely, while the other half exhibited a somewhat steeper fall-off.

The structure of the filename is "ObsID-Coma_name", where the name is adapted from the official IAU designation (nnnP for numbered periodic comets, yyyy** for unnumbered objects)[2], e.g. 1342186621-Coma_2006w3.

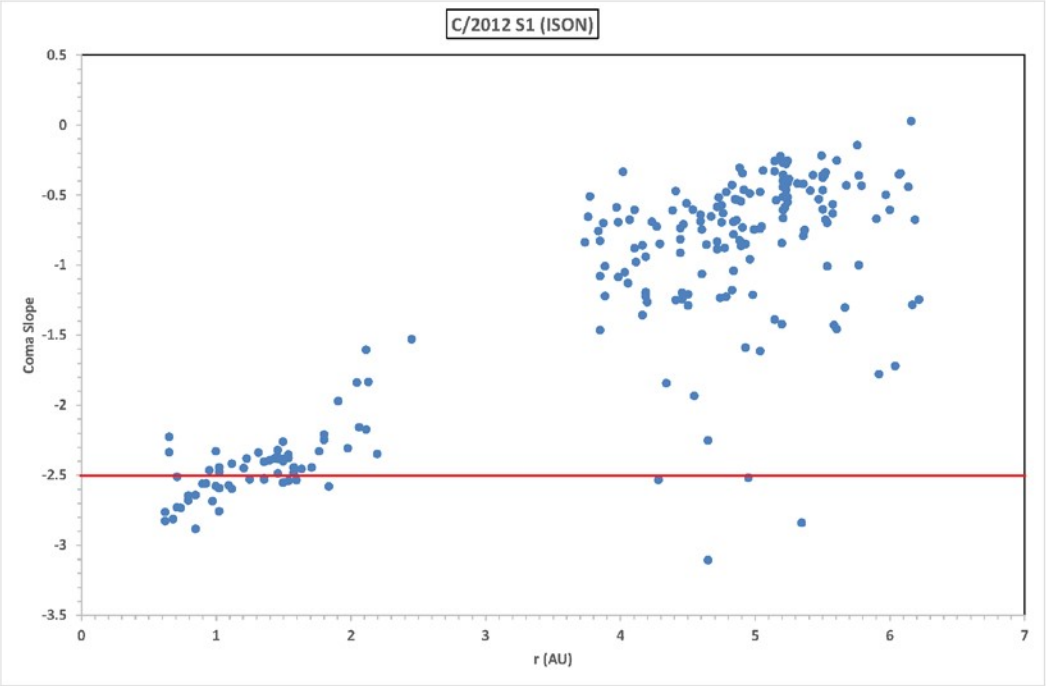

Figure 15: A typical plot of the variation of coma slope from CCD photometry against heliocentric distance. The coma slope is the exponent of the least squares fit of R magnitude against log aperture diameter. There are some outliers due to the difficulty of measuring accurately the total integrated magnitude in the larger apertures in bright sky conditions when the comet is faint and distant from the Sun; however, the trends can be seen clearly in the data.

7.3.5. Additional files for 29P/Schwassmann-Wachmann 1

Given the special characteristics of 29P/Schwassmann-Wachmann, we provide additional light curve files that give aperture photometry in R for the comet to provide light curve context for the Herschel data. These give the full light curve as magnitude within apertures of 10, 20, 30, 40, 50 and 60 arcseconds for the comet for the Herschel mission, with the epochs of PACS photometry marked.

Light curves are provided for

- 2009 (from 1st May)
- 2010 o 2010/11

Strictly speaking, in this work we deviate from the formal IAU naming convention by referring to

9P/Tempel 1 and 10P/Tempel 2, etc., mixing the official IAU and old-style (classical) designation. While the IAU name 9P/Tempel unambiguously defines (old style) Comet Tempel 1, the practice of adding the suffix “1”, “2”, “3”, etc. where there is more than one comet with the same name is so extended that we follow it here.

- 2011 o 2012
- 2013 (until June 30th)

The additional 2010/11 light curve is provided, covering the second half of 2010 and the first half of 2011, because the epoch of the Herschel data (02/01/2011) falls at the intersection of two years. The formal of the filename is ObsID-Light_29p_yyyy.

For 29P/Schwassmann-Wachmann 1, some additional contextual data is provided to show the typical time scales and evolution of an outburst. This is:

1. The evolution of a double outburst over a period of six days from quiescence on 19th January 2006, to post-maximum on 24th January 2006: ObsID-29P-200601_evolution-442
2. Pre-outburst and maximum for the outburst on 18th February 2006 in the form of images on 16th, 17th and 18th February 2006: ObsID-29p-200602-evolution-442
3. Normalised CCD light curve in R for 29P from 2001 – 2018: ObsID-29P-Normalised-light
4. Normalised CCD light curve in R for 29P during the Herschel mission on an expanded scale. The epochs of PACS Photometry observations are identified with arrows: ObsID-29PNormalised-light-expanded
5. The combination of (3) and (4) in a single figure with two panels: ObsID-29P-Normalised-lightinsert.
6. R-band light curve for a typical outburst (December 2007/January 2008) in apertures from 10-40 arcseconds to show the typical time scales of photometric activity: ObsID-29poutburst-20061229.
7. Magnitude differences between different apertures during the outburst shown in (6) to show how the wave of expansion from the outburst fills the different apertures: ObsID-29poutburst-20061229-Differences.

- Images for the correction of ObsIDs 1342212281 and 1342212282

In these images we show the process of correcting the photometry of 29P/Schwassmann-Wachmann 1 for the bright, background galaxies in the field of view that contaminate the coma in these two ObsIDs.

For each galaxy we present the following images:

- ObsID-HPPUNIMAPB/R-n – Unimap product showing the field with no overlay, where B/R are the blue (70 microns) and red (160 microns channels) respectively.

- ObsID-HPPUNIMAPB/R-n-ApPhot – Unimap product showing the field with the photometric aperture overlain on galaxy "n".

- In addition, in some cases, we present an additional file, ObsID-HPPUNIMAPB/R-1-resized – which gives a zoom of the image to see detail with more clarity.

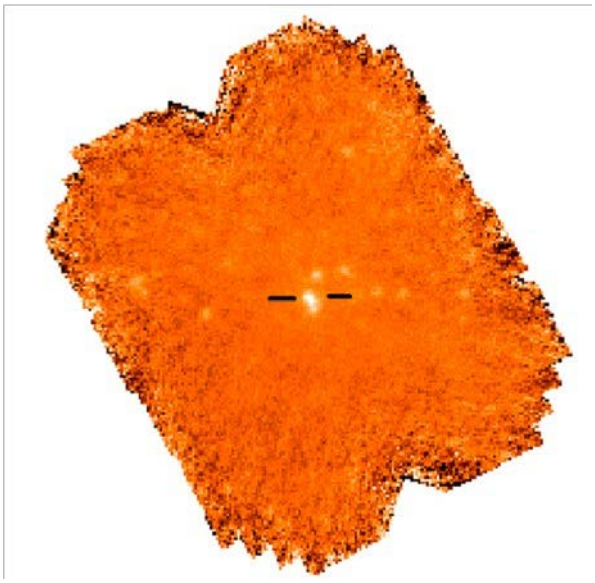

Figure 16: Raw map of 29P/Schwassmann-Wachmann 1. The comet is the brightest source in the field of view, but surrounded by background galaxies that contaminate the

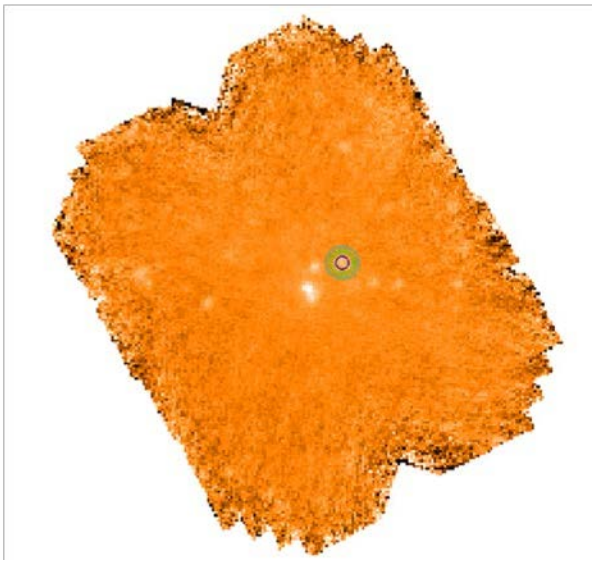

Figure 17: The same image, showing the process of extracting photometry of the contaminating galaxies to subtract their flux from the comet flux. The blue, inner ring is the chosen photometric aperture, with the outer annulus the chosen sky area.

The folder contains the raw images and the photometric apertures used to subtract out the background galaxies from the deep observation of 29P/Schwassmann-Wachmann 1 made on 2nd January 2011, when the comet was crossing a southern Leo. See Figure 16 and Figure 17 for examples.

7.4. Source list

Our source list is shown in Table 1, along with basic physical and observational data for the objects observed, which allows the Herschel data to be placed in their proper context. Instead of the geocentric distance for the epoch of observation, we give the herschelcentric distance; for the majority of objects, the difference between the two values is negligible but, given that Herschel ranged from ≈3.5-4.5 LD from Earth, in a highly inclined orbit, its range from the comet could be significantly different to that of the centre of the Earth.

Comet	Dynamical Type	Bands observed	T	q	P	# Epochs	Observation		r	Δ
							OD	Date		
C/2006 W3 (Christensen)	New	70, 160 70, 160	06/07/2009	3.126	$2.4x10^6$	2	171 469	01/11/2009 26/08/2010	3.326 4.955	3.557 4.538
C/2009 P1 (Garradd)	New	70, 100, 160 70, 160	23/12/2011	1.551	Open	2	889 1293	19/10/2011 27/11/2012	1.791 2.150	1.911 3.115
C/2011 L4 (PanSTARRS)	New	70, 160	10/03/2013	0.302	Open	1	1140	09/09/2012	3.261	3.582
C/2012 S1 (ISON)	New	70, 160	28/11/2013	0.0125	Open	1	1400	13/03/2013	4.470	4.095
C/2013 A1 (Siding Spring)	New	70, 100, 160	25/10/2014	1.400	Open	1	1418	31/03/2013	6.478	6.872
9P/Tempel 1	Jupiter Family	70, 100, 160	12/01/2011	1.543	5.56	1	797	20/07/2011	2.300	1.684
10P/Tempel 2	Jupiter Family	70, 160	04/07/2010	1.422	5.37	1	418	06/07/2010	1.423	0.752
29P/Schwassmann-Wachmann 1	Intermediate period	70, 160	10/07/2004 [3]	5.718	14.65	3	392 599 1375	10/06/2010 02/01/2011 17/02/2013	6.215 6.244 6.231	6.635 5.838 5.820

[3] Nominally this perihelion date applies only to the first two epochs of observation. The third epoch of observation took place after aphelion and thus the following perihelion date (07/03/2019) is more appropriate. However, given the very low orbital eccentricity (e=0.045, for Epoch 09/08/2009) and the minimal difference between the perihelion (5.718 AU) and aphelion (6.258 AU), the concept of the proximity of the observations to perihelion is of limited significance for this comet.

45P/Honda-Mrkos-Pajdusakova	Jupiter Family	70, 160	28/09/2011	0.533	5.26	1	824	16/08/2011	1.002	0.064
103P/Hartley 2	Jupiter Family	70, 160 70, 100, 160 70, 100, 160	28/10/2010	1.059	6.465	3	529 539 546	25/10/2010 04/11/2010 11/11/2010	1.060 1.063 1.076	0.117 0.137 0.182

Table 2: Source list for the catalogue. From left to right the columns are: name of target; Dynamical type; PACS bands in which it was observed (μm); perihelion distance (AU); Period (if determinate, years); number of epochs observed; OD(s) on which the comet was observed; calendar date(s) of observation; heliocentric distance of at the epoch of the observation (AU); herschelcentric distance at the epoch of the observation (AU). Orbit information is taken from the JPL Horizons System and can differ significantly from the elements obtained from the IAU's Minor Planet Center's Ephemeris Service (https://cgi.minorplanetcenter.net/cgi-bin/mpeph2.cgi) as these refer the elements to an epoch close to the date of retrieval – for C/2006 W3 (Christensen) and C/2009 P1 (Garradd) this is ≈10 years after perihelion, at which point the orbit has been significantly perturbed with respect to the orbital elements at the epoch of perihelion.

7.5. Comets not included in this catalogue

Three additional comets were observed by Herschel, two of them at high heliocentric distance and, thus, in an inactive state, the third, approximately two months after it had disrupted prior to reaching perihelion. These objects are not included in this compilation as they can be treated in the former two cases as point sources and are compiled in Volume II of this catalogue only and in the latter case no clear detection was made. In the majority of these cases the flux is below 25 mJy and thus the objects must be treated as faint sources requiring special treatment.

7.5.1. 67P/Churyumov-Gerasimenko

Integrations were taken at 70 (2828s), 100 (3956s) and 160 μm (6784s) on OD386 – 04/06/2010 – with the comet at r=4.1 AU, approaching aphelion. Weak, point source detections were obtained.

7.5.2. C/1995 O1(Hale-Bopp)

A deep integration (>10h) in mini scanmap mode was taken on OD392 – 10/06/2010 – at 70 and 160 μm, with the comet at r=30.0AU. A weak detection at ≈1 mJy was obtained at 70 μm. No clear detection was obtained at 160 μm.

7.5.3. C/2010 X1 (Elenin)

This comet was observed to disrupt in late August 2011, ≈6 weeks prior to perihelion. A single, deep integration (3.9h) was taken on the position of the comet on OD888 (19/10/2011), 2 days from its closest approach to Earth, optimized for detecting any possible discrete fragments within the expanding debris cloud. No point sources were detected, although there is a possible, very low confidence detection of the diffuse debris cloud.

8. The Catalogue

Our sample, listed in Table 1, consists of ten objects, of which five are short or intermediate period and five are dynamically new, Oort Cloud objects. The five dynamically new objects represent three distinct types: two with perihelion distance inside Mercury; two with perihelion distance close to the orbit of Mars, for which water sublimation will dominate at perihelion and one with perihelion beyond 3 AU, for which low-temperature volatiles should dominate the activity at all times.

Here was give brief notes on each of the ten objects, along with complementary information, where available, from visible monitoring from the Spanish "Observadores_cometas" group coordinated by one of the authors of this supplement.

For each comet we give an estimate of the dust activity at the epoch of observation using the Afρ parameter described by A'Hearn et al. (1984) and widely used to characterise cometary activity in the visible, although one of the conditions for it to be valid is that the coma radia; profile approximates to 1/r. The relationship between Afρ and the dust production rate Q_{dust} depends on many assumptions, with values of the conversion factor from Afρ to Q_{dust} that are derived typically between 5 and 10. This has been investigated by Fink & Rubin (2012) using data for Comet 67P/Churyumov-Gerasimenko and the in situ data from the Rosetta mission, who find differences of up to two orders of magnitude in the resultant values of Afρ according to the particle mass distribution adopted. Assuming a particle size distribution $Q \sim a^{-3}$, implying that $dn/da \sim a^{-4}$, they found Afρ = 227 cm for Q_{dust} = 4.66 kg/s giving a conversion factor of Q_{dust} (kg) = Afρ (cm)/48.7. Fink & Rubin (2012) quote values of $dn/da \sim a^{-3.8}$ for 9P/Tempel 1 and $dn/da \sim a^{-3.6 \text{ to } -4.0}$ for C/1995 O1 (Hale-Bopp), implying $Q \sim a^{-2.8}$ for both comets, suggesting that the assumption that $Q \sim a^{-3}$ is a good generalisation for a range of dynamic types.

8.1. Comments on individual objects

8.1.1. C/2006 W3 (Christensen)

8.1.1.1. ObsIDs used

1342186621, 1342186622, 1342203478, 1342203479

8.1.1.2. Background

C/2006 W3 (Christensen) was discovered by Christensen on 18th November 2006, in the course of the Catalina Sky Survey, although pre-discovery observations were found subsequently back to 29th October 2006. At the time of discovery, it was at r=10.67 AU and of magnitude 18.1. The comet is dynamically new, having fallen from a heliocentric distance of ≈5500AU, with 1/a(orig) = +0.000373 AU^{-1}, 1/a(fut) = +0.000241 AU^{-1} (elements from MPC 82313) and has a nominal orbital period of 2.4 million years.

8.1.1.3. Visible data

C/2006 W3 (Christensen) shows the light curve of a typical gassy, dynamically new object with considerable activity at large heliocentric distance. The comet's entry in Yoshida's on-line catalogue of

light curves (http://www.aerith.net/comet/catalog/2006W3/2006W3.html) finds a best light curve fit of $m_1 = -2.5 + 5 \log \Delta + 17.5 \log r$, giving a r^{-7} brightening law, as against the more typical 7 log r rate of brightening for dynamically new comets close to the Sun.

CCD aperture photometry by the Spanish "Observadores_cometas" group finds Afρ=3700 cm at perihelion within a 10^5km aperture. The coma slope, fitted as integrated magnitude against $\log_{10}$ aperture diameter from CCD photometry, decreases monotonically towards perihelion, from -1.85 at a heliocentric distance of 4.5 AU, to -2.35 at perihelion. For a coma with a 1/r radial profile – where "r" in the standard notation is the radial distance from the nucleus – we would expect a value of the slope of -2.5, thus the visible coma was always more condensed than the "ideal" 1/r coma profile.

Date	Exposure	Telescope	Filter	Observer	Site
05/12/2009	-	30cm	Unfiltered	Muler	MPC J47 (Lanzarote, Spain)
15/06/2010	7.5 minutes	25cm	Unfiltered	Tifner	MPC I32 (Rosario, Argentina)

Table 3: Details of the complementary visible images of C/2006 W3 (Christensen). These are not necessarily the images that are most nearly simultaneous with the Herschel data, but instead are the images as close temporally to the epoch of the Herschel observation that provide the most useful comparison in terms of depth, image scale and s/n. From left to right we give: the date of observation; the exposure time (if recorded – otherwise blank); the telescope diameter; the photometric filter or filters used (otherwise "unfiltered"; the observer name or names; and the observing site. The code that is listed is the Minor Planet Center IAU site code (see https://www.minorplanetcenter.net/iau/lists/ObsCodesF.html for details).

8.1.1.4. Herschel data

Herschel took imaging photometry at 70 and 160 μm at two epochs, both after perihelion. The first observation was taken using slow scan speed (10"/s), a mode that was later supressed for science use. Similarly, both epochs were taken using the original 45°/135° angles for scan and cross-scan.

Date	Observing mode	Integration Time	Scan speed	Scan length	Cross-scan separation	# Scan legs	# Repetitions
01/11/2009	Scan map	1130s	10"/s	9.9'	148.5"	3	2
26/08/2010	Scan map	2530s	20"/s	3'	20"	5	8

Table 4: Observing parameters for the observations of C/2006 W3 (Christensen) presented in the catalogue. From left to right the columns are: date of observation, observing mode, observation duration (sum of scan and cross-scan), scan speed, length of each scan leg, separation of the scan legs, the number of scan legs executed in the scan pattern, number of repetitions of the scan pattern.

8.1.1.5. Summary of results

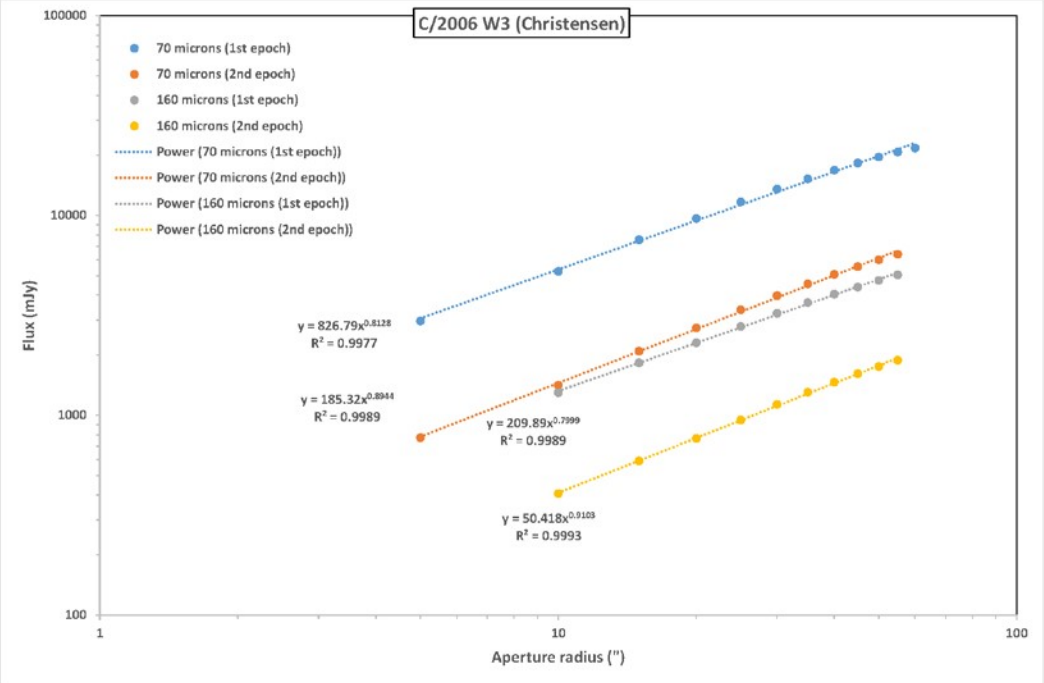

Figure 18: Coma profiles for C/2006 W3 (Christensen) for the two epochs of observation.

At both epochs of observation, the coma is clearly extended, with a tail to the north-east. Flux from the coma can be detected out to at least 60 arcseconds from the centre of light. Similarly, at both epochs the slope of the coma is flatter in 70 µm than at 160 µm, thus the coma is more concentrated close to the nucleus at the longer wavelength. At the second epoch the comet was much more distant from perihelion, although the integration was much deeper: at this epoch we see a similar pattern in the coma slopes, although the coma is marginally more extended than previously at 70 µm and marginally steeper at 160 µm but, in both cases, the differences are within the expected errors.

8.1.2. C/2009 P1 (Garradd)

8.1.2.1. ObsIDs Used

1342231249, 1342231250, 1342231251, 1342231252, 1342255964, 1342255965, 1342255970, 1342255971

8.1.2.2. Background

C/2009 P1 (Garradd) was discovered by Garradd from Siding Spring Observatory on 13th August 2009, with pre-discovery images subsequently located back to 27th September 2008. At the time of discovery, it was at r=8.69 AU and of magnitude 17.5. The comet is dynamically new and quite strongly hyperbolic

at perihelion (e=1.0010), with strong non-gravitational terms (A1 = +2.14, A2 = -0.1233), although the osculating elements show that the comet had closed by the time that the comet had receded to the orbit of Uranus after perihelion.

8.1.2.3. Visible data

The light curve of C/2009 P1 (Garradd) is consistent with a much less gassy nucleus than for C/2006 W3 (Christensen), although it showed a prominent gas tail at a heliocentric distance greater than 6 AU. The comet's entry in Yoshida's on-line catalogue of light curves (http://www.aerith.net/comet/catalog/2009P1/2009P1.html) finds a best light curve fit pre-perihelion of $m_1 = 3.2 + 5 \log \Delta + 10.5 \log r$ and, post-perihelion, of $m_1 = 2.1 + 5 \log \Delta + 16.0 \log r$; while the former shows a much slower rate of brightening inbound towards perihelion than for a typical, gassy comet, the rapid post-perihelion fade is typical of dynamically new objects.

CCD aperture photometry by the Spanish "Observadores_cometas" group finds Afρ=4700 cm at perihelion within a 10^5km aperture. The coma slope, fitted as integrated magnitude against $\log_{10}$ aperture diameter from CCD photometry, decreases towards perihelion, from -2.1 at a heliocentric distance of 5 AU, to -2.5 at 2.4AU and -2.75 at perihelion. Thus the visible coma was more condensed than the "ideal" 1/r coma profile at a heliocentric distance greater than 2.4AU, but more extended than a 1/r profile close to perihelion.

Date	Exposure	Telescope	Filter	Observer	Site
15/10/2011	30 minutes	35cm	RGB+unfiltered	Ligustri & Di Giusto	MPC 235 (Talmassons, Italy)
07/12/2012	-	40cm	Unfiltered	Hernández	MPC J24 (Tenerife, Spain)

Table 5: Details of the complementary visible images for C/2009 P1 (Garradd). These are not necessarily the images that are most nearly simultaneous with the Herschel data, but instead are the images as close temporally to the epoch of the Herschel observation that provide the most useful comparison in terms of depth, image scale and s/n. From left to right we give: the date of observation; the exposure time (if recorded – otherwise blank); the telescope diameter; the photometric filter or filters used (otherwise "unfiltered"; the observer name or names; and the observing site. The code that is listed is the Minor Planet Center IAU site code (see https://www.minorplanetcenter.net/iau/lists/ObsCodesF.html for details).

8.1.2.4. Herschel data

Herschel took imaging photometry at 70 and 160 μm at two epochs: the first, two months prior to perihelion; the second, eleven-months post-perihelion. The first observation was taken using the original 45°/135° angles for scan and cross-scan, while the second observation was taken with the

70°/110° angles for scan and cross-scan (the “magic angle”) that became default for the rest of the mission.

Date	Observing mode	Integration Time	Scan speed	Scan length	Cross-scan separation	# Scan legs	# Repetitions
19/10/2011	Scan map	710s	20”/s	9.9‘	148.5”	3	4
27/11/2012	Scan map	1414s	20”/s	3‘	4”	10	5

Table 6: Observing parameters for the observations of C/2009 P1 (Garradd) presented in the catalogue. From left to right the columns are: date of observation, observing mode, observation duration (sum of scan and cross-scan), scan speed, length of each scan leg, separation of the scan legs, the number of scan legs executed in the scan pattern, number of repetitions of the scan pattern.

8.1.2.5. Summary of results

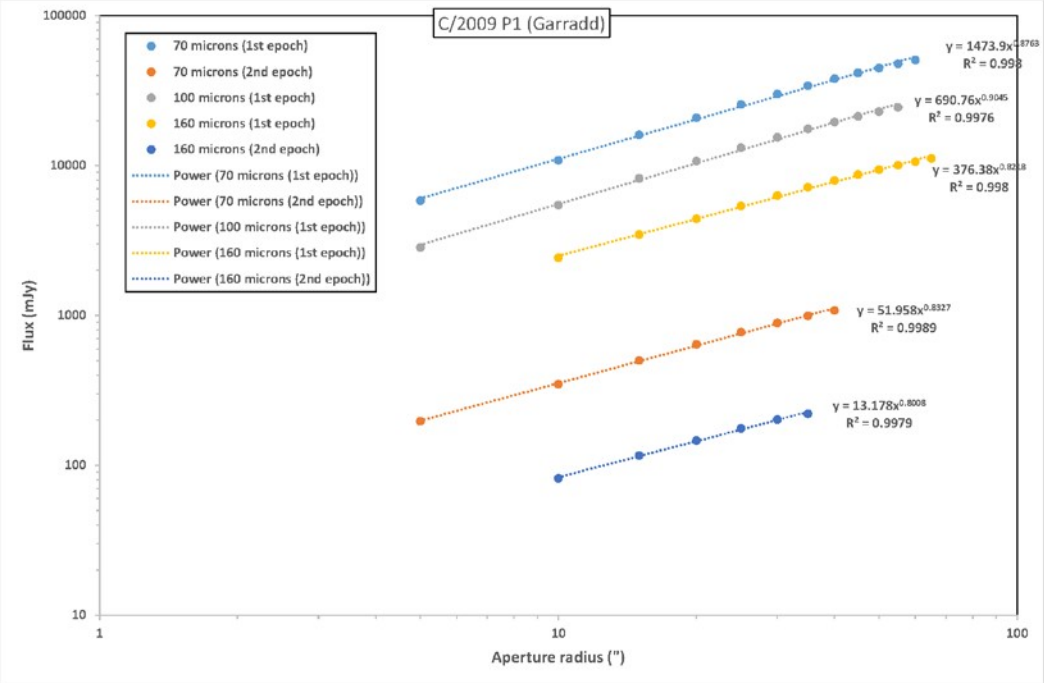

Figure 19: Coma profiles for C/2009 P1 Garradd at the two epochs of observation.

At both epochs of observation, the coma is extended, with a tail to the east clearly visible at 70 and 100 µm. Flux from the coma can be detected out to at least 90 arcseconds from the centre of light. Although the flux is much lower at the second epoch than at the first, this is mainly due to the considerable increase in the herschelcentric distance, with only a modest increase in the heliocentric distance between the two epoch. We see that the coma profile is slightly steeper at both 70 µm and 160 µm at the first epoch, with the comet closer to perihelion than at the second epoch. It is also

slightly steeper at both epochs at 70 µm than at 160 µm, although the steepest value of all was found at 100 µm, which was only measured at the first epoch.

8.1.3. C/2011 L4 (PanSTARRS)

8.1.3.1. ObsIDs Used

1342250781, 1342250782

8.1.3.2. Background

C/2011 L4 (PanSTARRS) was discovered by the PanSTARRS-1 Telescope at Haleakala on 6th June 2011, with pre-discovery images subsequently located back to 21st May 2011. At the time of discovery, it was at r=8.04 AU and of magnitude 19.4. The comet is dynamically new and was slightly hyperbolic at perihelion (e=1.00003), although with closed original and future orbits (1/a(orig) = +0.000029 AU^{-1}, 1/a(fut) = +0.000446 AU^{-1}), implying that the comet has fallen from ≈70000 AU (slightly more than 1 light year) in the outer fringes of the Oort Cloud. This comet was interesting for being Halley-class in activity and for having a perihelion distance slightly within the orbit of Mercury (q=0.302)

8.1.3.3. Visible data

The light curve of C/2011 L4 (PanSTARRS) was similar to that of C/2006 W3 (Christensen) beyond r≈5.3 AU, indicating a large gas content. The rate of brightening slowed progressively within the orbit of Jupiter as water sublimation took over, although the comet continued to brighten at a respectable rate even close to perihelion, becoming a naked-eye object that reached m_1≈+1 in March 2013. A gas tail started to develop at a heliocentric distance ≈4.5 AU. The comet's entry in Yoshida's on-line catalogue of light curves (http://www.aerith.net/comet/catalog/2011L4/2011L4.html) finds a best light curve fit pre-perihelion of $m_1 = -1.8 + 5 \log \Delta + 18.0 \log r$ beyond the orbit of Jupiter and of $m_1 = 5.0 + 5 \log \Delta + 7.5 \log r$ close to perihelion, with a rapid post-perihelion fade typical of dynamically new objects.

CCD aperture photometry by the Spanish "Observadores_cometas" group finds Afρ≈50000 cm at 0.86 AU post-perihelion, within a 10^5km aperture and Afρ≈470 close to the epoch of observation by Herschel. The coma slope, fitted as integrated magnitude against $\log_{10}$ aperture diameter from CCD photometry, decreases towards perihelion, from being effectively a point source at a heliocentric distance greater than 4.5 AU, to -2.5 at 2AU and approximately at -2.65 within 2 AU. Thus the visible coma was more condensed than the "ideal" 1/r coma profile at a heliocentric distance greater than 2.0AU, but slightly more extended than a 1/r profile close to perihelion.

Date	Exposure	Telescope	Filter	Observer	Site
07/07/2012	-	25.4cm	RGB+unfiltered	Ligustri	MPC H06 (Mayhill, New Mexico)

Table 7: Details of the complementary visible image for C/2011 L4 (PanSTARRS). These are not necessarily the images that are most nearly simultaneous with the Herschel data, but instead are the images as close temporally to the epoch of the Herschel observation that provide the most useful comparison in terms of depth, image scale and s/n. From left to right we give: the date of observation; the exposure time (if recorded – otherwise blank); the telescope diameter; the photometric filter or filters used (otherwise "unfiltered"; the observer name or names; and the observing site. The code that is listed is the Minor Planet Center IAU site code (see https://www.minorplanetcenter.net/iau/lists/ObsCodesF.html for details). Due to the southerly declination of the comet at the epoch of the Herschel observation and the relatively small elongation from the Sun, there are few observations from Northern Hemisphere sites close to the epoch of observation by Herschel.

8.1.3.4. Herschel data

Herschel took imaging photometry at 70 and 160 µm at a single epoch, three days before the end of the pre-perihelion visibility window: the comet did not have visibility for Herschel post-perihelion until after the end of cryogen. The observation was taken using the original 45°/135° angles for scan and cross-scan.

Date	Observing mode	Integration Time	Scan speed	Scan length	Cross-scan separation	# Scan legs	# Repetitions
09/09/2012	Scan map	2280s	20"/s	5'	18.5"	8	4

Table 8: Observing parameters for the observations of C/2011 L4 (PanSTARRS) presented in the catalogue. From left to right the columns are: date of observation, observing mode, observation duration (sum of scan and cross-scan), scan speed, length of each scan leg, separation of the scan legs, the number of scan legs executed in the scan pattern, number of repetitions of the scan pattern.

8.1.3.5. Summary of results

The coma is clearly extended to the east at 70 and 160 µm, with a tail out to at least 75", clearly visible at 70 µm. Flux from the coma can be detected out to at least 40 arcseconds from the centre of light, although this appears to be mainly contribution from the tail beyond ≈20" from the centre of light. Although the extent of the coma is not great in the Herschel data, the coma profile ($\log_{10}$ flux against $\log_{10}$ aperture) is the flattest and most extended for any of the dynamically new objects in our sample, indicating the smallest degree of concentration of flux close to the nucleus of any comet in our sample.

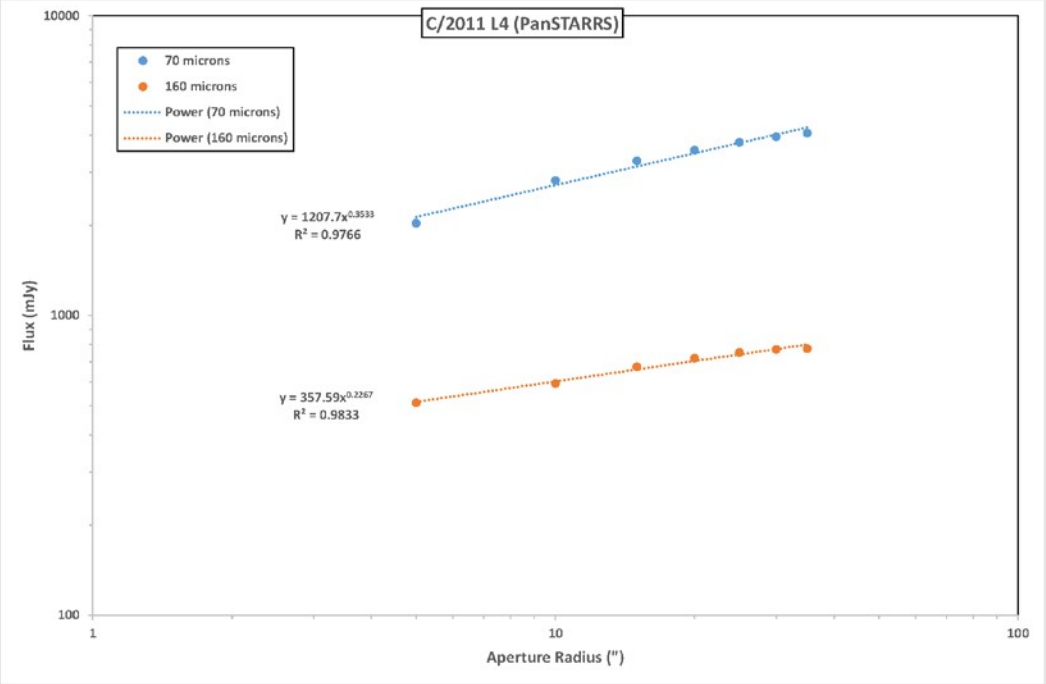

Figure 20: Coma profiles for C/2011 L4 (PanSTARRS) for the Herschel observations.

8.1.4. C/2012 S1 (ISON)

8.1.4.1. ObsIDs Used

1342267433, 1342267434, 1342267443, 1342267444

8.1.4.2. Background

C/2012 S1 (ISON) was discovered by the International Scientific Optical Network (ISON) near Kislovodsk, Russia on 21st September 2012, with pre-discovery images subsequently located back to 30th September 2011. At the time of discovery, it was at r=8.04 AU and of magnitude 19.4. The comet was dynamically new and was slightly hyperbolic at perihelion (e=1.0002) This comet was particularly interesting as it was a sungrazer (q=0.0126 AU), so potentially could become either extremely brilliant or fail to survive perihelion. The comet showed a series of small outbursts, initiating ≈2 weeks before perihelion that were later realized to be due to the progressive disruption of the nucleus. A small remnant was briefly observed post-perihelion, which was observed for approximately two weeks around closest approach to the Earth. The disruption led to large non-gravitational terms in the orbit (non-gravitational parameters A1 = +7.87, A2 = +0.6396).

8.1.4.3. Visible data

The light curve of C/2012 S1 (ISON) was similar to that of C/2009 P1 (Garradd), never showing a particularly rapid rate of brightening, even beyond the orbit of Jupiter. Similar to C/2009 P1 (Garradd), the rate of brightening slowed within the orbit of Jupiter as water sublimation took over, although the comet continued to brighten at a respectable rate even close to perihelion. A gas tail started to develop

at a heliocentric distance ≈4.5 AU, at the time that the comet was observed by Herschel. The comet's entry in Yoshida's on-line catalogue of light curves (http://www.aerith.net/comet/catalog/2012S1/2012S1.html) finds a best light curve fit preperihelion of $m_1 = 5.5 + 5 \log \Delta + 10 \log r$ to 4.3 AU from the Sun, and of $m_1 = 8.0 + 5 \log \Delta + 7.5 \log r$, thereafter.

CCD aperture photometry by the Spanish "Observadores_cometas" group finds Afρ≈480 cm at 1 AU, within a 10^5km aperture and Afρ≈50 close to the epoch of observation by Herschel, indicating that the comet had only a low level of intrinsic activity. The coma slope, fitted as integrated magnitude against $\log_{10}$ aperture diameter from CCD photometry, decreases progressively towards perihelion, from being effectively a point source at a heliocentric distance greater than 3.5 AU, to -2.5 inside 1.6 AU and approximately -2.6 when inside the Earth's orbit. Thus the visible coma was more condensed than the "ideal" 1/r coma profile at a heliocentric distance greater than 1.6AU, but slightly more extended than a 1/r profile within the Earth's orbit.

Date	Exposure	Telescope	Filter	Observer	Site
14/03/2013	-	23.5cm	unfiltered	González	MPC J01 (León, Spain)

Table 9: Details of the complementary visible image for C/2012 S1 (ISON). These are not necessarily the images that are most nearly simultaneous with the Herschel data, but instead are the images as close temporally to the epoch of the Herschel observation that provide the most useful comparison in terms of depth, image scale and s/n. From left to right we give: the date of observation; the exposure time (if recorded – otherwise blank); the telescope diameter; the photometric filter or filters used (otherwise "unfiltered"; the observer name or names; and the observing site. The code that is listed is the Minor Planet Center IAU site code (see https://www.minorplanetcenter.net/iau/lists/ObsCodesF.html for details).

8.1.4.4. Herschel data

Herschel took imaging photometry at 70 and 160 μm at a single epoch, three days before the end of the pre-perihelion visibility window: the comet did not have visibility for Herschel post-perihelion until after the end of cryogen. The observation was taken using the 70°/110° angles configuration for scan and cross-scan.

Date	Observing mode	Integration Time	Scan speed	Scan length	Cross-scan separation	# Scan legs	# Repetitions
13/03/2013	Mini Scan map	3392s	20"/s	3'	4"	10	6

Table 10: Observing parameters for the observations of C/2012 S1 (ISON) presented in the catalogue. From left to right the columns are: date of observation, observing mode, observation duration (sum of scan and cross-scan), scan speed, length of each scan leg, separation of the scan legs, the number of scan legs executed in the scan pattern, number of repetitions of the scan pattern.

8.1.4.5. *Summary of results*

We see a small coma at 70 µm, with a narrow tail extending to ≈30-40" to the east. The signal at 160 µm is very weak, although there is a hint of a similar tail. The coma profile (log_{10} flux against log_{10} aperture) is one of the flattest for any of the dynamically new objects in our sample with only a small extension of flux and little central condensation obvious at 70 µm, although the coma is significantly steeper at 160 µm.

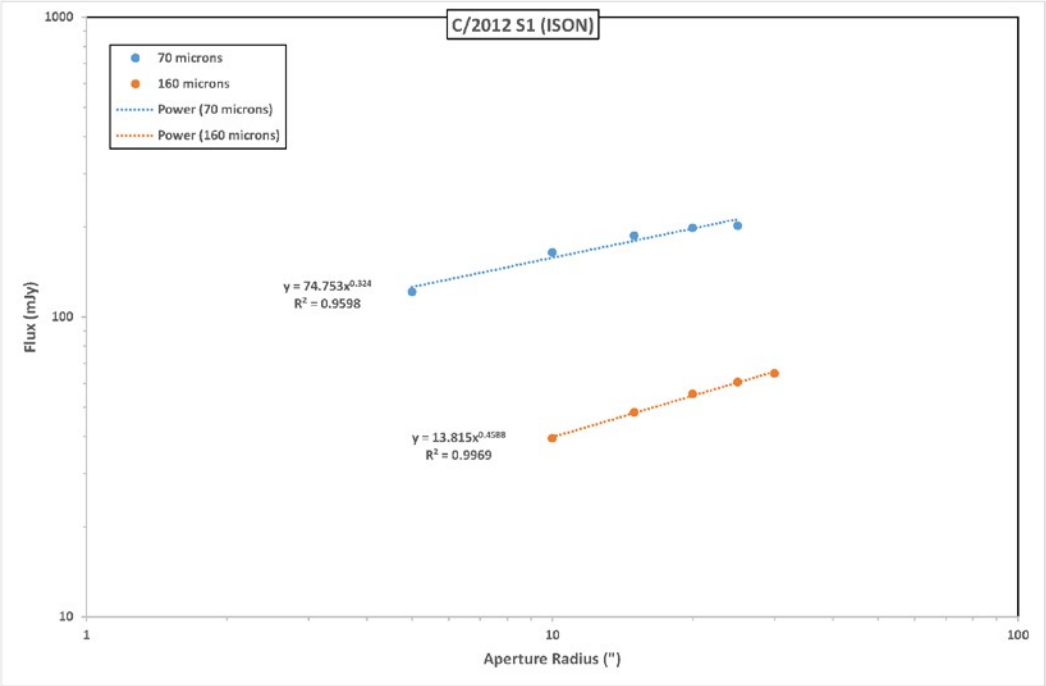

Figure 21: Coma profile for C/2012 S1 (ISON) from the Herschel observations.

8.1.5. C/2013 A1 (Siding Spring)

8.1.5.1. *ObsIDs Used*

1342268982, 1342268983, 1342268984, 1342268985

8.1.5.2. *Background*

C/2013 A1 (Siding Spring) was discovered from Siding Spring Observatory (Australia) on 3rd January 2013, with pre-discovery images subsequently located back to 4th October 2012. At the time of discovery, it was at r=7.21 AU and of magnitude 18.6. The comet is dynamically new and had an orbit that was slightly hyperbolic at perihelion (e=1.0003), but which has closed since. This comet was particularly interesting due to its close Mars pass: at 18:27:30UT on 19th October 2014, the comet passed at 0.000939 AU from the centre of the planet (140 500km, 0.37 LD).

8.1.5.3. *Visible data*

The light curve of C/2013 A1 (Siding Spring) shows unique features within our sample. A faint gas tail is visible in images made two days after discovery but, at the time that the comet was observed by

Herschel, the comet's visibility was very poor from the northern hemisphere; later images, closer to the epoch of the Herschel observation, do not resolve the tail. The comet's entry in Yoshida's on-line catalogue of light curves (http://www.aerith.net/comet/catalog/2013A1/2013A1.html) finds a best light curve fit pre-perihelion of $m_1 = 8.8 + 5 \log \Delta + 6 \log r$ (t+40), indicating both that the comet's activity showed a strong perihelion asymmetry (more typical in dynamically highly evolved comets), although in the sense of peak activity being advanced with respect to perihelion, which is unusual given that normally, when an asymmetry is observed, it is in the sense of a *delay* in peak activity with respect to perihelion. The small exponent of increase in activity with heliocentric distance shows that the comet was volatile-poor, even at a heliocentric distance of more than 7 AU but, despite that, there was a 2 magnitude outburst two weeks after perihelion.

CCD aperture photometry by the Spanish "Observadores_cometas" group finds Afρ≈30 cm within a 25000 km aperture close to the epoch of the Herschel observation[4] and Afρ≈75 cm immediately after solar conjunction, at a heliocentric distance 4.8 AU. The coma slope, fitted as integrated magnitude against $\log_{10}$ aperture diameter from CCD photometry, decreases towards perihelion, from being effectively a point source at a heliocentric distance greater than 4.5 AU, to -2.5 at 2AU and approximately at -2.65 within 2 AU. Thus the visible coma was more condensed than the "ideal" 1/r coma profile at a heliocentric distance greater than 2.0AU, but slightly more extended than a 1/r profile close to perihelion.

Date	Exposure	Telescope	Filter	Observer	Site
05/01/2013	-	40cm	Unfiltered	Hernández	MPC J24 (Tenerife, Spain)
10/01/2013	1260s	25cm	Unfiltered	Garcia	MPC J38 (Asturias, Spain)
26/01/2013	-	40cm	Unfiltered	Hernández	MPC J24 (Tenerife, Spain)

Table 11: Details of the complementary visible images for C/2013 A1 (Siding Spring). These are not necessarily the images that are most nearly simultaneous with the Herschel data, but instead are the images as close temporally to the epoch of the Herschel observation that provide the most useful comparison in terms of depth, image scale and s/n. From left to right we give: the date of observation; the exposure time (if recorded – otherwise blank); the telescope diameter; the photometric

[4] We choose this smaller aperture as it close to the diameter of the visible coma as reported by the HST.

filter or filters used (otherwise "unfiltered"; the observer name or names; and the observing site. The code that is listed is the Minor Planet Center IAU site code (see https://www.minorplanetcenter.net/iau/lists/ObsCodesF.html for details).

8.1.5.4. Herschel data

Herschel took imaging photometry at 70, 100 and 160 µm at a single epoch, four days before the end of the pre-perihelion visibility window: the comet did not re-enter visibility for Herschel until after the end of cryogen. The observation was taken using the optimal 70°/110° angles for scan and cross-scan.

Date	Observing mode	Integration Time	Scan speed	Scan length	Cross-scan separation	# Scan legs	# Repetitions
09/09/2012	Mini Scan map	6048s	20"/s	3.5'	4"	10	10

Table 12: Observing parameters for the observations of C/2013 A1 (Siding Spring) presented in the catalogue. From left to right the columns are: date of observation, observing mode, observation duration (sum of scan and cross-scan), scan speed, length of each scan leg, separation of the scan legs, the number of scan legs executed in the scan pattern, number of repetitions of the scan pattern.

8.1.5.5. Summary of results

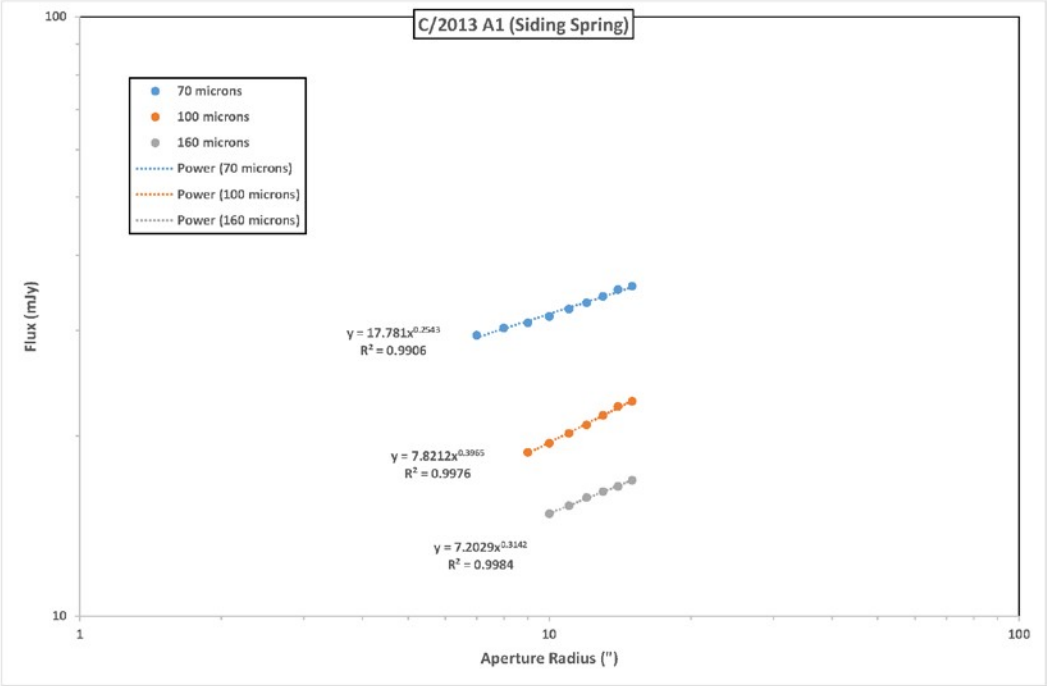

Figure 22: Coma profiles for C/2013 A1 (Siding Spring) for the Herschel observations.

The coma appears slightly extended at 70 and 100 µm, with no obvious elongation of coma or tail, although the s/n is not as high as would have been desirable. At 160 µm the s/n is very low. Flux from the coma can be detected only out to 15-20 arcseconds from the centre of light. The coma profile is very flat for this object: as for C/2009 P1 (Garradd), the coma is steepest at 100 µm and much flatter at 70 and 160 µm.

8.1.6. 9P/Tempel 1

8.1.6.1. ObsIDs Used

1342224492, 1342224493, 1342224494, 1342224495

8.1.6.2. Background

Discovered on 3rd April 1867 by Ernst Tempel at magnitude 9, the comet was on its twenty-fourth return to perihelion when observed by Herschel, although the 2011 return was only the eleventh to be observed as the comet was lost after its 1879 return and not recovered until 1967. The comet's orbit is entirely within the orbits of Mars and Jupiter with a perihelion distance of 1.54 AU, aphelion at 4.75 AU and a period of 5.52 years in 2011 that has increased to 5.56 years for its latest return. 9P/Tempel 1 is a small comet (mean radius 2.8 km) of low activity that was the target for the NASA Deep Impact mission (A'Hearn & Combi, 2007).

8.1.6.3. Visible data

The 2011 return was a poor one, with the comet on the far side of the Sun and thus unobservable to Herschel for ten months around perihelion. The heavily observed 2005 return's entry in Yoshida's online catalogue of light curves (http://www.aerith.net/comet/catalog/0009P/2005.html) finds a best light curve fit around perihelion of $m_1 = 6.0 + 5 \log \Delta + 25 \log r$. There is though some evidence that the comet was rather less active than in 2005 at the much less heavily covered 2011 perihelion pass (http://www.aerith.net/comet/catalog/0009P/2011.html). This equates to a switch-on of activity at ≈3.0 AU pre-perihelion, with an almost equally rapid switch-off of activity at ≈2.5 AU post-perihelion.

Date	Exposure	Telescope	Filter	Observer	Site
20/08/2011	-	40cm	Unfiltered	Hernández	MPC J24 (Tenerife, Spain)
26/01/2013	-	23.5cm	unfiltered	González	MPC J01 (León, Spain)

Table 13: Details of the complementary visible images of 9P/Tempel 1. These are not necessarily the images that are most nearly simultaneous with the Herschel data, but instead are the images as close temporally to the epoch of the Herschel observation that provide the most useful comparison in terms of depth, image scale and s/n. From left to right we give: the date of observation; the exposure time (if recorded – otherwise blank); the telescope diameter; the photometric filter or filters used (otherwise "unfiltered"; the observer name or names; and the observing site. The code that is listed is the Minor Planet Center IAU site code (see https://www.minorplanetcenter.net/iau/lists/ObsCodesF.html for details).

CCD aperture photometry by the Spanish "Observadores_cometas" group finds Afρ≈30 cm within a 25000 km aperture close to the epoch of the Herschel observation[5]. The coma slope, fitted as integrated magnitude against $\log_{10}$ aperture diameter from CCD photometry, decreases towards perihelion, from being effectively a point source at a heliocentric distance greater than 2.0 AU, to being an "ideal" 1/r coma profile within 2.6 AU. A faint, broad tail is visible in images taken in August and September.

8.1.6.4. Herschel data

Herschel took imaging photometry at 70, 100 and 160 µm at a single epoch, six months after perihelion. The observation was taken using the optimal 70º/110º angles for scan and cross-scan.

Date	Observing mode	Integration Time	Scan speed	Scan length	Cross-scan separation	# Scan legs	# Repetitions
20/07/2011	Mini Scan map	2828s (70 µm) 3956s (100 µm) 6784 s (160 µm)	20"/s	3 '	4"	10	5

Table 14: Observing parameters for the observations of 9P/Tempel 1 presented in the catalogue. From left to right the columns are: date of observation, observing mode, observation duration (sum of scan and cross-scan), scan speed, length of each scan

[5] We choose this smaller aperture as, in general, little flux is measured outside this coma diameter by CCD

leg, separation of the scan legs, the number of scan legs executed in the scan pattern, number of repetitions of the scan pattern.

observers.

8.1.6.5. Summary of results

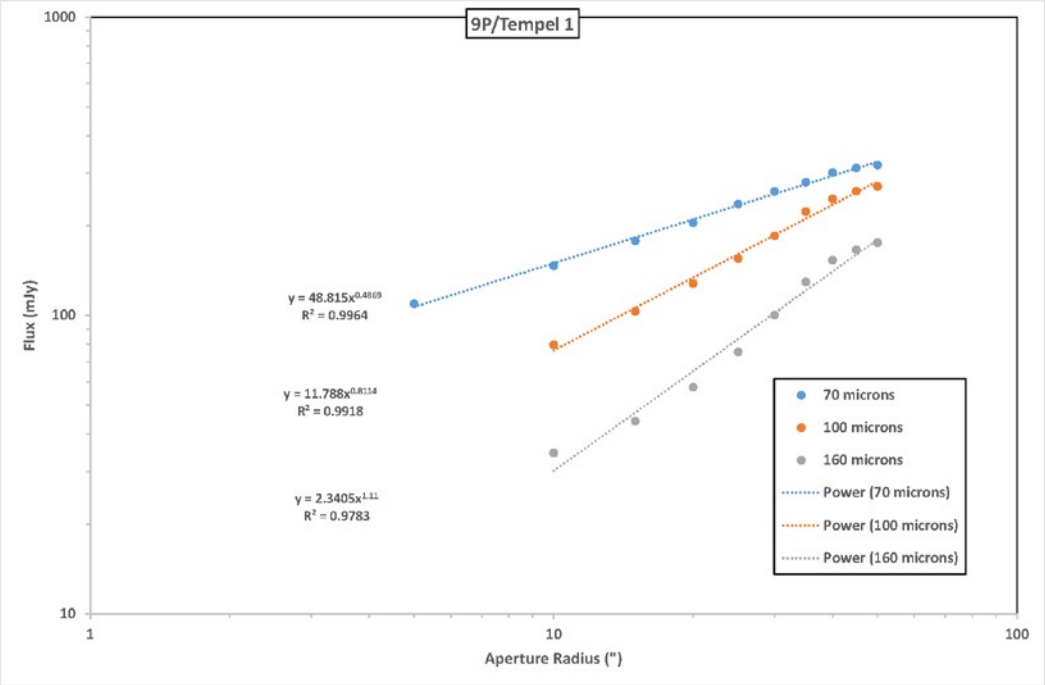

Figure 23: Coma profiles for 9P/Tempel 1 for the Herschel observations.

The coma appears slightly extended at 70 and 100 µm, with a faint tail to the west-south-west. At 160 µm the s/n is very low and confusion is an issue as there are several similarly faint sources in the field. Flux from the coma can be detected out to ≈60 arcseconds from the centre of light. The coma slope increases considerably from 70 to 160 µm, showing that the coma is more extended at shorter

wavelengths and quite point-like at 160 µm: the 160 µm data for this comet is the only case where we find a coma slope >1 in our sample.

8.1.7. 10P/Tempel 2

8.1.7.1. ObsIDs Used

1342199877, 1342199878

8.1.7.2. Background

Discovered on 3rd July 1873 by Ernst Tempel at magnitude 9.5, the comet was on its twenty-sixth return to perihelion when observed by Herschel, of which twenty-one have been observed. The comet's orbit crosses the orbit of Mars, with a perihelion distance of 1.42 AU, aphelion at 4.71 AU and a period of 5.37 years. The nucleus has a mean radius of 5.3 km.

8.1.7.3. Visible data

Circumstances were very good for observing the comet in 2010, with the comet close at opposition not long after perihelion and reaching a total visual magnitude of 8. The entry in Yoshida's on-line catalogue of light curves (http://www.aerith.net/comet/catalog/0009P/2005.html) finds a best light curve fit pre-perihelion, inside 2.4 AU, of $m_1 = 4.6 + 5 \log \Delta + 35 \log r$, however, the data suggests that the rate of rise was even faster. This equates to a sudden switch-on of activity at ≈2.4 AU preperihelion, with a much slower switch-off of activity at ≈4.6 AU post-perihelion, consistent with a very evolved nucleus.

CCD aperture photometry by the Spanish "Observadores_cometas" group finds Afρ≈440 cm within a 25000 km aperture at the epoch of the Herschel observation[6]. Unusually, the coma slope, fitted as integrated magnitude against $\log_{10}$ aperture diameter from CCD photometry, increases towards perihelion, from being effectively very diffuse at a heliocentric distance ≈2.3 AU, to being an "ideal" 1/r coma profile within 1.9 AU. Images show a strongly green coma, typical of C_2 emission and the broad fan tail (typical in comets observed almost head-on) around perihelion. The gas coma is as large as 15 arcminutes at the time of the Herschel observations.

Date	Exposure	Telescope	Filter	Observer	Site
08/07/2010	300s	40cm	Unfiltered	Ligustri	MPC Q62 (Siding Spring, Australia)

[6] Again, we choose this smaller aperture as, in general, little flux is measured outside this coma diameter by CCD observers.

12/08/2010	1560s	25.4cm	BVR+unfiltered	Ligustri	MPC H06 (New Mexico, USA)

Table 15: Details of the complementary visible images of 10P/Tempel 2. These are not necessarily the images that are most nearly simultaneous with the Herschel data, but instead are the images as close temporally to the epoch of the Herschel observation that provide the most useful comparison in terms of depth, image scale and s/n. From left to right we give: the date of observation; the exposure time (if recorded – otherwise blank); the telescope diameter; the photometric filter or filters used (otherwise "unfiltered"; the observer name or names; and the observing site. The code that is listed is the Minor Planet Center IAU site code (see https://www.minorplanetcenter.net/iau/lists/ObsCodesF.html for details).

8.1.7.4. Herschel data

Herschel took imaging photometry at 70 and 160 µm at a single epoch, just two days after perihelion. The observation was taken using the optimal 70°/110° angles for scan and cross-scan.

Date	Observing mode	Integration Time	Scan speed	Scan length	Cross-scan separation	# Scan legs	# Repetitions
06/07/2010	Scan map	1420s	20"/s	9.9 '	148.5"	3	4

Table 16: Observing parameters for the observations of 10P/Tempel 2 presented in the catalogue. From left to right the columns are: date of observation, observing mode, observation duration (sum of scan and cross-scan), scan speed, length of each scan leg, separation of the scan legs, the number of scan legs executed in the scan pattern, number of repetitions of the scan pattern.

8.1.7.5. Summary of results

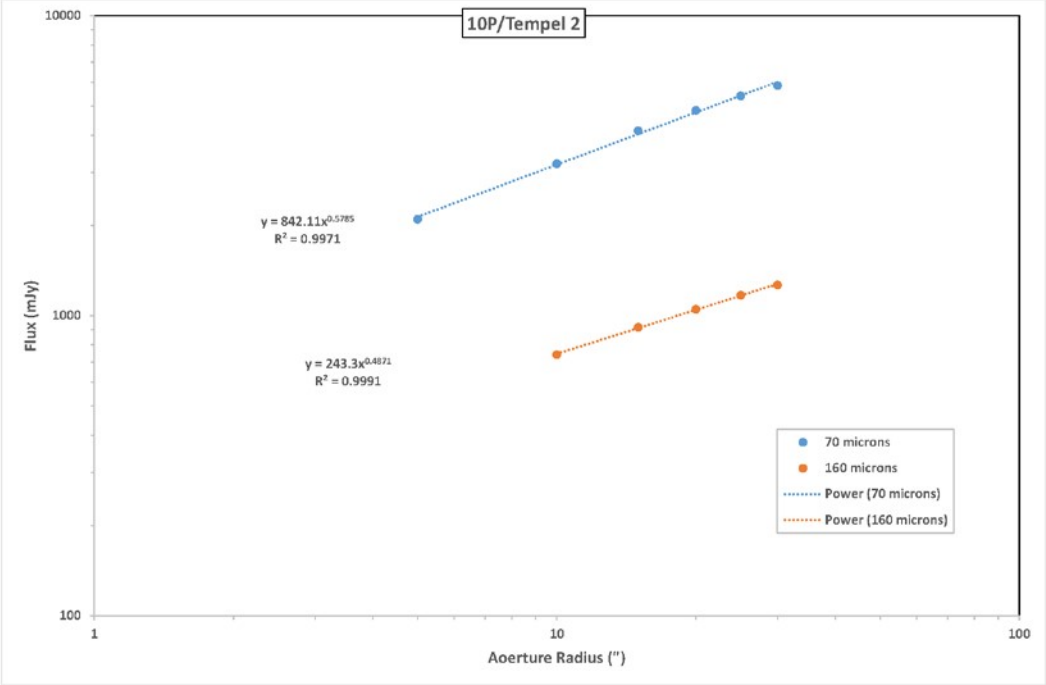

Figure 24: Coma profiles for 10P/Tempel 2 for the Herschel observations.

The coma is clearly extended at 70 and 160 µm on a north-south axis, with a faint fan tail to the west, particularly at 70 µm. Flux from the coma can be detected out to ≈25-30 arcseconds from the centre of light. The coma slope is much steeper at 70 than at 160 µm.

8.1.8. 29P/Schwassmann-Wachmann 1

8.1.8.1. ObsIDs Used

1342198444, 1342198445, 1342212281, 1342212282, 1342263832, 1342263833, 1342263834, 1342263835

8.1.8.2. Background

Discovered in 15th November 1927 by Schwassmann and Wachmann at magnitude 12, the comet was later located in images taken as far back as 4th March 1902. 29P/Schwassmann-Wachmann is a member of the class of giant comets, having an absolute magnitude of +3 and a radius of the nucleus of 31km. At present, it has an almost circular orbit between the orbits of Jupiter and Saturn. When first discovered the orbital eccentricity was as high as 0.15 but it has reduced steadily due to planetary perturbations to the current value of 0.045. The comet's orbit covers only a small range of heliocentric distance, with a perihelion distance of 5.72 AU, aphelion at 6.26 AU and a period of 14.65 years (when first observed, the period was 16.44 years). The most remarkable aspect of the comet's activity are the frequent outbursts that may reach an amplitude of 6 or 7 magnitudes: these are uncorrelated with the position of the comet in its orbit.

8.1.8.3. Visible data

Given the unusual orbit of this comet its visibility circumstances were similar to those of Jupiter, with full visibility of 47 and 50 days each year and 14-16 additional days of limited visibility at hot betas while, for earthbound observation, there is visibility for approximately 6-8 months each year depending on the comet's declination which, during the first Herschel observations was +10° but, by the final epoch of -24°, greatly limiting northern hemisphere visibility. The entry in Yoshida's on-line catalogue of light curves (http://www.aerith.net/comet/catalog/0029P/2004.html, http://www.aerith.net/comet/catalog/0029P/2019.html) give a light curve fit of $m_1 = 4.0 + 5 \log \Delta + 7.5 \log r$, however, as the light curve is completely dominated by the outbursts, this is no more than a very approximate baseline.

Given that normally 29P/Schwassmann-Wachmann 1 does not even approximate to a 1/r coma[7], the assumptions in calculating Afρ are not valid, thus we cannot offer even indicative values for comparison with other comets in the sample.

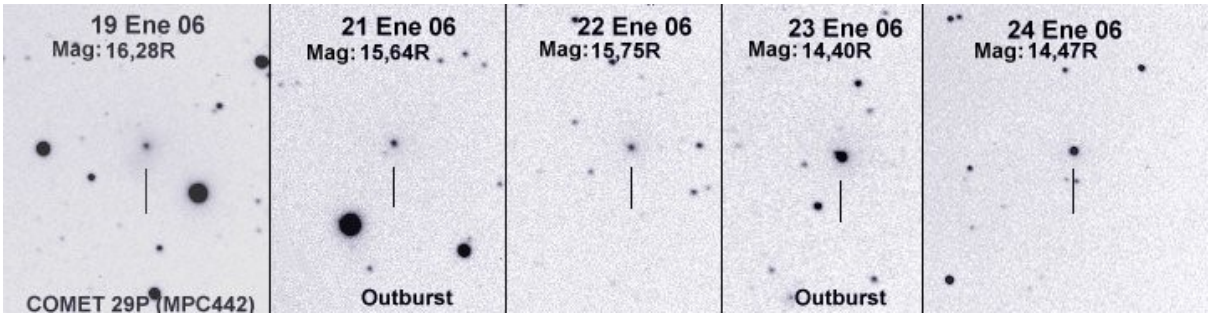

Figure 25: The development of a typical outburst of 29P/Schwassmann-Wachmann 1 over an interval of five days. In the first image we see the comet in its quiescent state, with a faint, extended coma surrounding a weak nuclear condensation. Two nights later, the outburst has initiated and the central condensation is 0.6 magnitudes brighter and better defined. On the third night the nuclear condensation is fainter and less well-defined, as it expands. On the fourth night, a new and bigger outburst initiates – the nuclear condensation, involved with a fainter star, is 2 magnitudes brighter than pre-outburst – which, in the final frame, is starting to decay.

However, given that this comet is completely unlike any other in our sample in its behaviour we give some additional information of use to understand the Herschel data and the circumstances and context of each of the Herschel observations. The photometric progress of a typical outburst is shown in Figure 2.

[7] When an outburst starts, the comet develops an intense, stellar nuclear condensation that contains almost all the flux (see Figure 1). As the outburst develops, the wave of brightness spreads outwards and fades until it becomes a diffuse coma that can be several arcminutes across. When a new outburst appears, it appears within the extended coma that is the remains of the previous outburst.

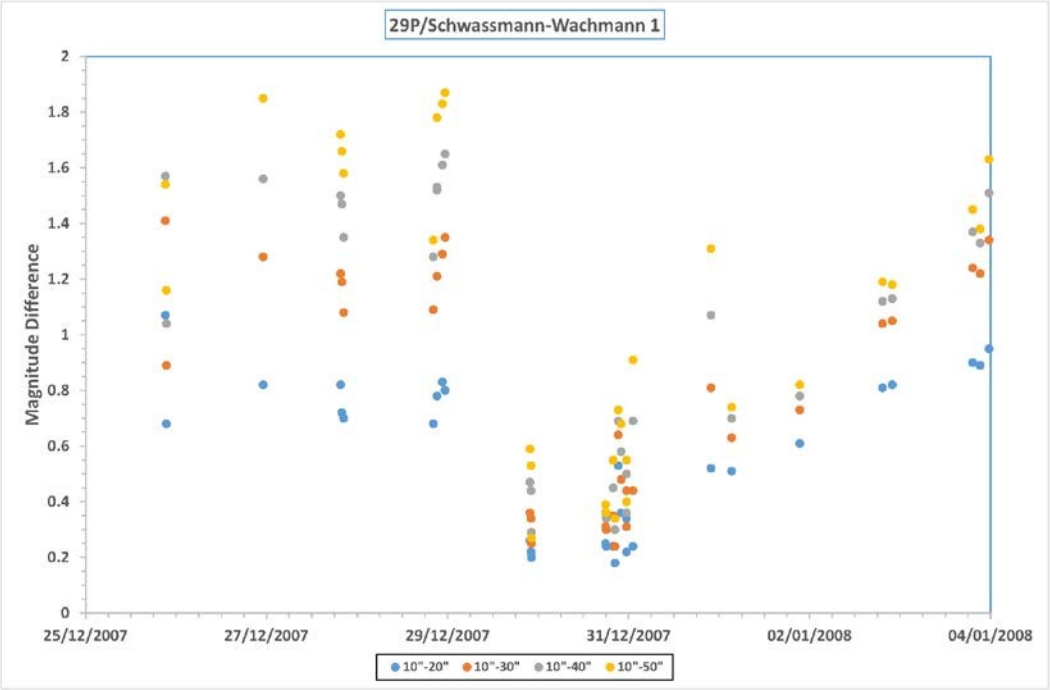

Figure 26: The photometric progress of a typical outburst of 29P/Schwassmann-Wachmann 1 shown as the difference between the integrated magnitude in apertures from 20" to 50" with the magnitude in a 10" aperture. Pre-outburst there is a faint, extended coma that reveals itself by the fact that the integrated magnitude in the largest apertures is much brighter than in 10". At the peak of the outburst, most of the integrated flux is present in the quasi-stellar nuclear condensation and the magnitude differences between the smallest and the larger photometric apertures are close to zero but, as the outburst declines, these differences increase again steadily as the coma expands outwards at a typical velocity of ≈300 m/s, filling progressively the different apertures.

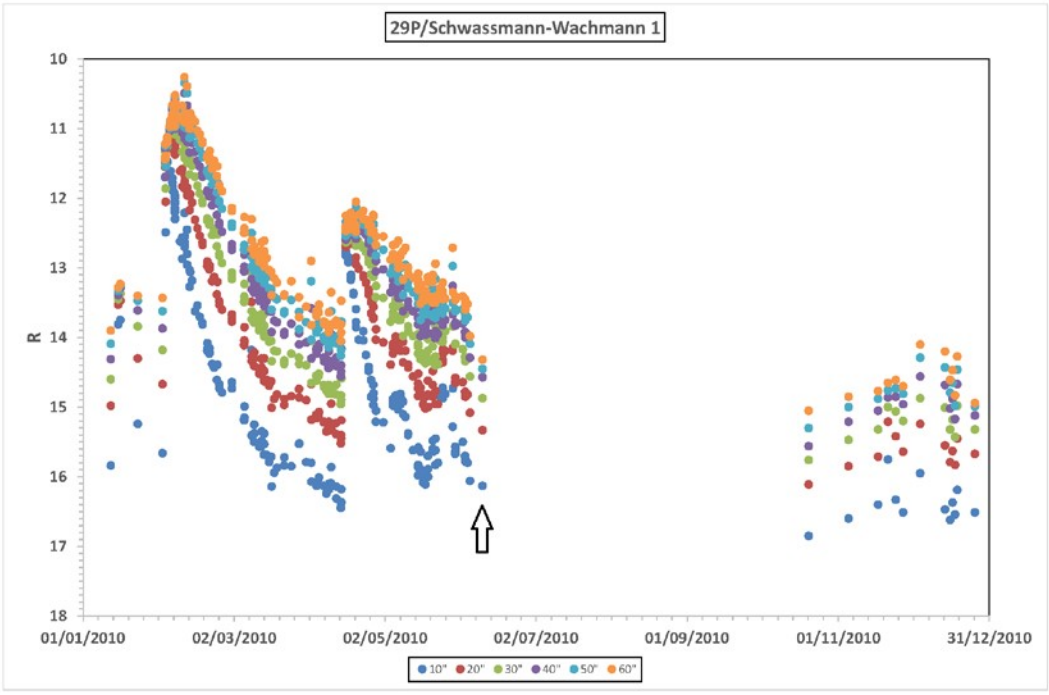

Figure 27: Photometric context for the first epoch of Herschel-PACS observations. The observations were taken at the end of the visibility window, in the decline phase of a minor outburst of 1 magnitude amplitude, that took place on 24th May 2010, 16 days before the Herschel observation, whose date is marked with an arrow.

The first epoch of observation with PACS was taken on the penultimate day of the visibility window, meaning that circumstances for ground-based observers were not ideal, with the comet low in evening twilight, so ground-based coverage ended shortly after the Herschel data were obtained. The observations took place 16 days after a small outburst of one magnitude amplitude that started on 24th May 2010 within the expanding coma of a previous outburst on 5th May 2010 (see Figure 2).

The second epoch of observation by Herschel-PACS was taken at the end of the visibility window, with the comet about to enter hot betas. 29P/Schwassmann-Wachmann 1 in an exceptionally low state after a long period of inactivity (see Figure 3). This low-activity state was not broken until a twomagnitude outburst on 21st January 2011, 19 days after the epoch of the Herschel observations.

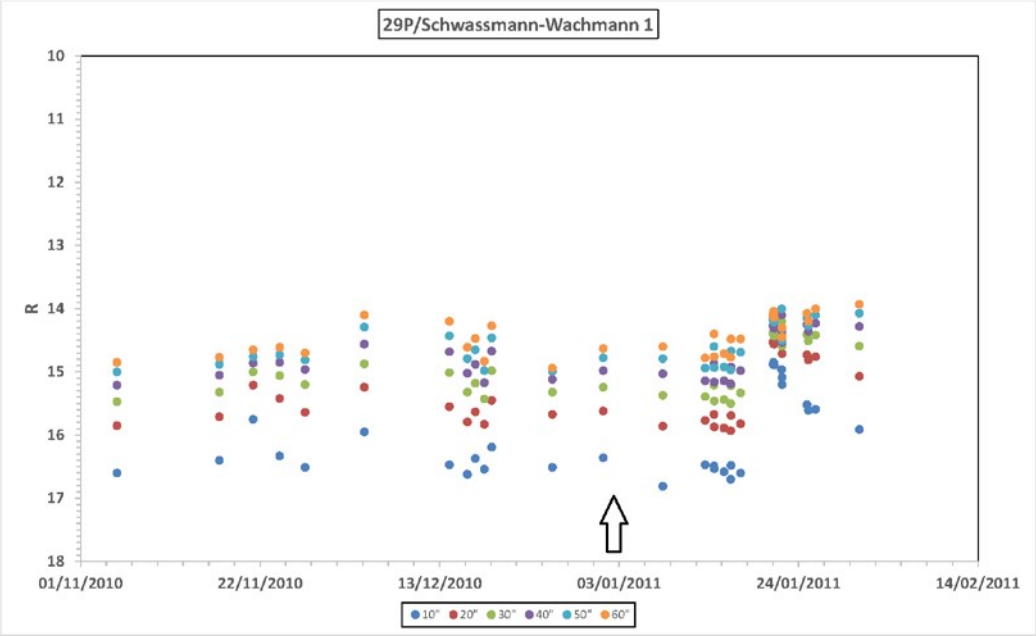

Figure 28: Photometric context for the second epoch of Herschel-PACS observations. The observations were taken at the end of the visibility window with the comet at an extremely low and inactive state at epoch of the Herschel observation, which is marked with an arrow. There had been no outburst in the two months prior to the Herschel observations.

The final Herschel-PACS observations of 29P/Schwassmann-Wachmann 1 were also taken at the end of a visibility window, with the comet about to enter hot betas and was, again, in a very low state. A small outburst appears to have occurred shortly after the Herschel observations were executed (there is an inconvenient gap in light curve coverage at this time, but coverage is sufficient to demonstrate that no outburst was active at the time of the Herschel observations).

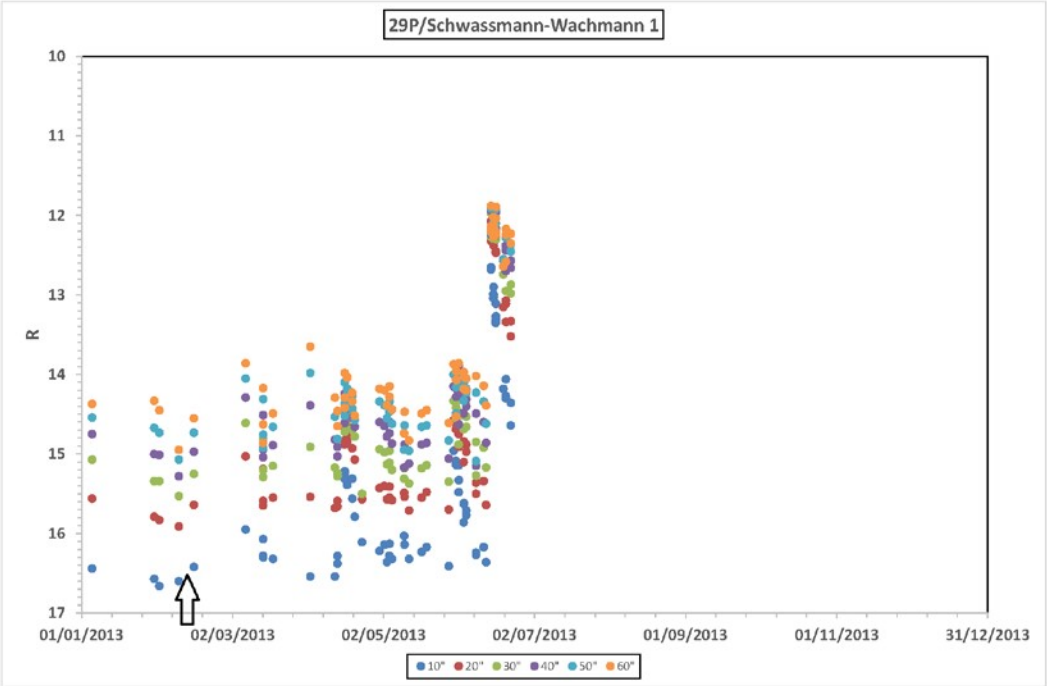

Figure 29: Photometric context for the third epoch of Herschel-PACS observations, taken at the start of the visibility window on the cold side. Again, the Herschel observations, marked with an arrow, were taken at an epoch when the comet was in a prolonged extremely low and inactive state. There had been no outburst in the two months prior to the Herschel observations.

Date	Exposure	Telescope	Filter	Observer	Site
21/05/2010	1080s	25cm	Unfiltered	García	MPC J38 (Asturias, Spain)
10/06/2010	1080s	25cm	Unfiltered	García	MPC J38 (Asturias, Spain)
12/01/2011	1260s	25cm	Unfiltered	García	MPC J38 (Asturias, Spain)
16/01/2011	1080s	25cm	Unfiltered	García	MPC J38 (Asturias, Spain)
29/01/2013	2685s	30cm	Unfiltered	Naves and	MPC 213

				Campàs	(Barcelona, Spain)
03/04/2013	-	25cm	Unfiltered	Lozano	MPC I57 (Elche, Spain)

Table 17: Details of the complementary visible images of 29P/Schwassmann-Wachmann 1. These are not necessarily the images that are most nearly simultaneous with the Herschel data, but instead are the images as close temporally to the epoch of the Herschel observation that provide the most useful comparison in terms of depth, image scale and s/n. From left to right we give: the date of observation; the exposure time (if recorded – otherwise blank); the telescope diameter; the photometric filter or filters used (otherwise "unfiltered"; the observer name or names; and the observing site. The code that is listed is the Minor Planet Center IAU site code (see https://www.minorplanetcenter.net/iau/lists/ObsCodesF.html for details).

8.1.8.4. Herschel data

Herschel took imaging photometry at 70 and 160 µm at three epochs, spanning the comet's pass through aphelion. The first and second observations were taken using angles of 45º and 135º for scan and cross-scan. The third observation was taken using the optimal 70º/110º angles for scan and crossscan in mini scan map mode, with a much smaller field of view.

Date	Observing mode	Integration Time	Scan speed	Scan length	Cross-scan separation	# Scan legs	# Repetitions
10/06/2010	Scan map	1420s	20"/s	9.9 '	148.5"	3	4
02/01/2011	Scan map	5700s	20"/s	5'	18.5"	8	10
17/02/2013	Mini Scan map	10140s	20"/s	3'	2"	8	10

Table 18: Observing parameters for the observations of 29P/Schwassmann-Wachmann 1 presented in the catalogue. From left to right the columns are: date of observation, observing mode, observation duration (sum of scan and cross-scan), scan speed, length of each scan leg, separation of the scan legs, the number of scan legs executed in the scan pattern, number of repetitions of the scan pattern.

8.1.8.5. Summary of results

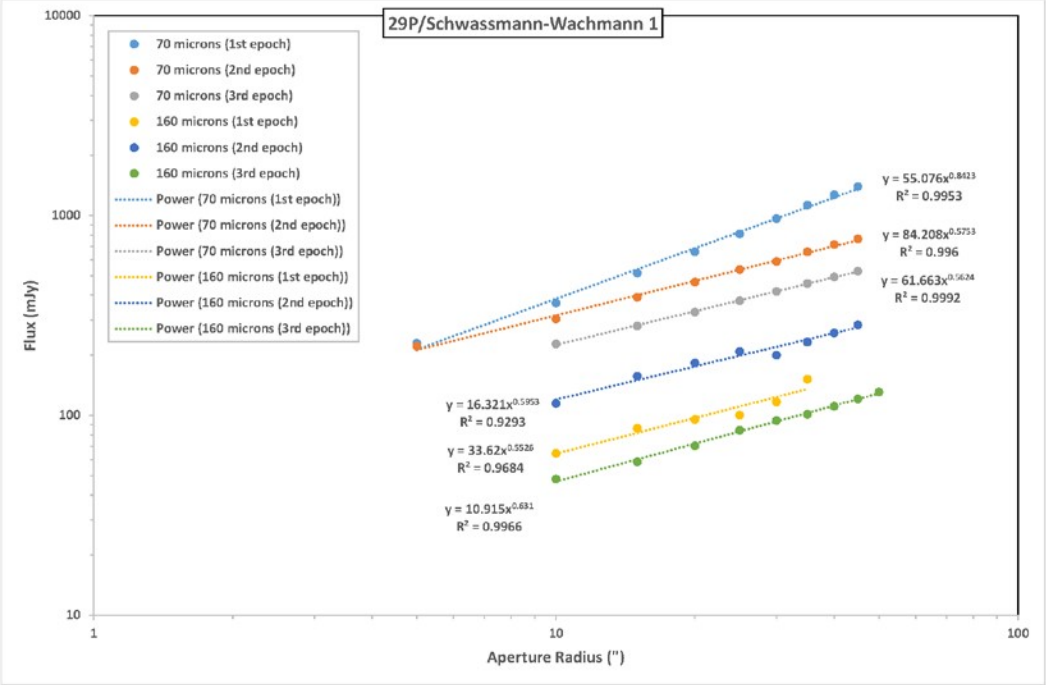

Figure 30: Coma profiles for 29P/Schwassmann-Wachmann 1 for the three epochs of observation.

The coma is clearly extended at 70 µm in the first epoch of observation, when the comet was brightest and in an active state, with wings visible in the east-west axis around a bright central condensation and an extension to the north. The s/n at 160 µm is low, but a similar extension can be detected faintly, particularly when contours are overlain. Similar structures can be seen in the second and third epoch data, with their much deeper exposures, although we note that the comet is severely confused with a background galaxy in the 160 µm second epoch data. Flux from the coma can be detected out to ≈20-25 arcseconds from the centre of light, although the visible gas coma reported by visual observers extends out to 60 arcseconds from the nucleus in simultaneous observations[8]. Visual observations close to the third epoch of Herschel data show an even larger coma, extending out to at least 210 arcseconds from the nucleus. The coma slope is much steeper 70 µm at the first epoch of observation than at the two later epochs when the comet was less active, showing that the emission was concentrated close to the nucleus when in the higher activity state, but also considerably more concentrated at 70 than at 160 µm. The coma slope is similar at all three epochs at 160 µm, while the slope is also very similar at 70 µm at the second and third epochs to the 160 µm values at all three epochs.

8.1.9. 45P/Honda-Mrkos-Pajdusakova

8.1.9.1. ObsIDs Used

1342227469, 1342227470

[8] Data kindly provided by Juan José "JJ" González (Asturias, Spain).

8.1.9.2. Background

Discovered on 3rd December 1948 by Minora Honda at magnitude 9.0, the comet was on its twelfth return to perihelion when observed by Herschel, of which eleven have been observed. The comet's orbit crosses the orbit of Venus, with a perihelion distance of 0.53 AU, aphelion at 5.52 AU, slightly outside the orbit of Jupiter and a period of 5.26 years, one of the shortest known. The nucleus has a mean radius of 0.8 km.

8.1.9.3. Visible data

Circumstances were very good for observing the comet in 2011, with the comet making the twelfth closest ever observed pass of a comet to the Earth (see the MPC's list of closest-ever observed comet passes to Earth at https://www.minorplanetcenter.net/iau/lists/ClosestComets.html) and also close to opposition not long after perihelion, reaching a total visual magnitude of 6.5. However, the close pass was over the South Pole of the Earth, with the comet reaching a declination of -68° as seen from Herschel and beyond -70° as seen from the centre of the Earth, thus the comet was only accessible to the small community of southern hemisphere observers while in visibility to Herschel and closest to Earth[9]. The entry in Yoshida's on-line catalogue of light curves (http://www.aerith.net/comet/catalog/0045P/2011.html) finds a best light curve fit pre-perihelion of $m_1 = 14.2 + 5 \log \Delta + 23 \log r$, which is an excellent fit to the data from the 2006, 2011 and 2016 returns. This equates to a sudden switch-on of activity at ≈2.0 AU pre-perihelion, with the comet only observed for ≈4 months, pre-perihelion.

CCD aperture photometry by the Spanish "Observadores_cometas" group finds that the value of Afρ within a 10000 km aperture[9] was doubling every five days two weeks before the Herschel observation, at which point the comet moved too far south to be observed from Europe. This would be consistent with a value of Afρ ≈900 cm at the epoch of observation by Herschel. The coma slope, fitted as integrated magnitude against $\log_{10}$ aperture diameter from CCD photometry, shows different behaviour pre- and post-perihelion. It is effectively a point source at a heliocentric distance larger than 1.5 AU, becoming an "ideal" 1/r coma profile at ≈0.8 AU and then increasing diffuse to ≈0.6 AU. Images show a strongly green coma, typical of C_2 emission and a narrow, strongly blue, gas tail (typical of ionised carbon monoxide) around perihelion. The gas coma was as large as 15 arcminutes at the time of the Herschel observations, but extremely diffuse, with almost no central condensation, although post-perihelion visual observers reported a very condensed coma.

[9] Closest approach to the centre of the Earth was 0.06005 AU at ≈03:30 UT on 15th August 2011. Closest approach to Herschel was 0.05824 AU at ≈14:15 UT on 14th August 2011.

Date	Exposure	Telescope	Filter	Observer	Site

[9] Again, we choose this smaller aperture as, in general, little flux is measured outside this coma diameter by CCD observers.

23/09/2011	-	12.5cm	Unfiltered	López	MPC J63 (Alicante, Spain)
29/09/2011	240s	50cm	BVR+Unfiltered	Ligustri	MPC H06 (New Mexico, USA)
01/10/2011	1645s	30cm	Unfiltered	Naves and Campàs	MPC 213 (Barcelona, Spain)

Table 19: Details of the complementary visible images for 45P/Honda-Mrkos-Pajdusakova. These are not necessarily the images that are most nearly simultaneous with the Herschel data, but instead are the images as close temporally to the epoch of the Herschel observation that provide the most useful comparison in terms of depth, image scale and s/n. From left to right we give: the date of observation; the exposure time (if recorded – otherwise blank); the telescope diameter; the photometric filter or filters used (otherwise "unfiltered"; the observer name or names; and the observing site. The code that is listed is the Minor Planet Center IAU site code (see https://www.minorplanetcenter.net/iau/lists/ObsCodesF.html for details).

8.1.9.4. Herschel data

Herschel took imaging photometry at 70 and 160 µm at a single epoch, six weeks before perihelion, during the brief, four-day, visibility window to Herschel at closest approach to Earth. The observation was taken using the 45°/135° angles for scan and cross-scan. A singularity of the observations was that the differential tracking rate was the highest of any object observed by Herschel in a standard observing mode (see Figure 31).

Date	Observing mode	Integration Time	Scan speed	Scan length	Cross-scan separation	# Scan legs	# Repetitions
16/08/2011	Scan map	2138s	20"/s	5 '	20"	15	2

Table 20: Observing parameters for the observations of 45P/Honda-Mrkos-Pajdusakova presented in the catalogue. From left to right the columns are: date of observation, observing mode, observation duration (sum of scan and cross-scan), scan speed, length of each scan leg, separation of the scan legs, the number of scan legs executed in the scan pattern, number of repetitions of the scan pattern.

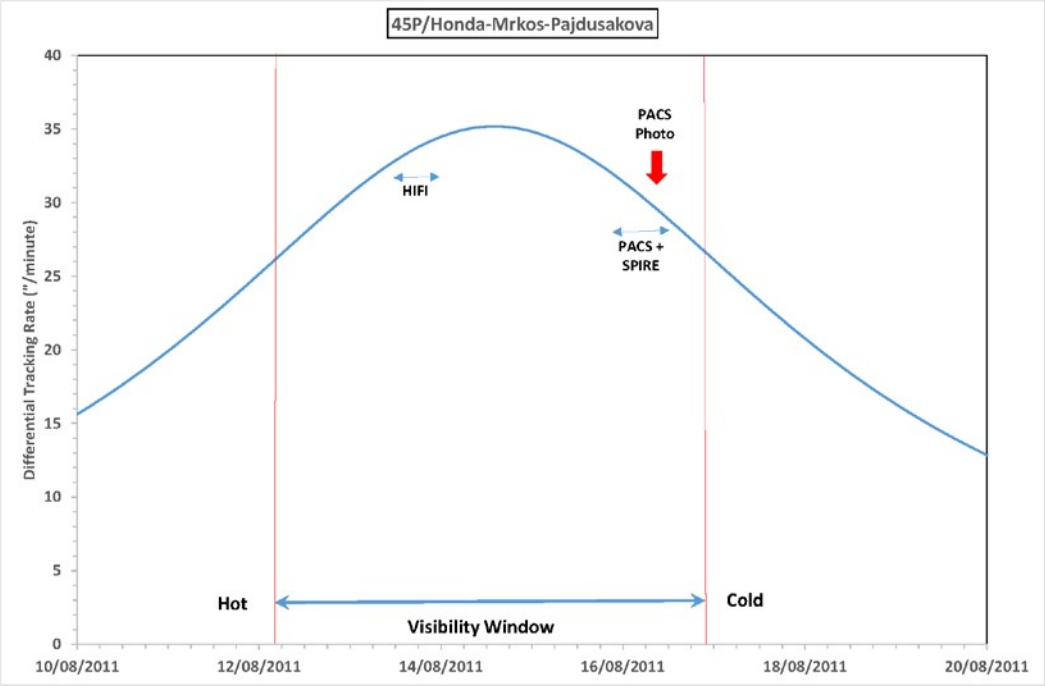

Figure 31: Circumstances of the Herschel observations of 45P/Honda-Mrkos-Pajdusakova. There was a very short visibility window due to the rapid motion of the comet as it made its close pass to the Earth, with it entering visibility on the hot side. By this stage of the mission, with spacecraft performance well understood and known to be trustworthy, the differential tracking limit was relaxed from the initial limit of 10"/minute at the start of the mission to a recommended maximum of ≈30"/minute but, with a maximum of 35".2 reached on 14th August 2011, it was decided that, within the limits imposed on Mission Planning, the observations should be scheduled away from the moment of greatest differential tracking rate to ensure tracking quality. The tracking of the observations was found to be perfect, despite the large differential rate[10].

8.1.9.5. Summary of results

The coma is clearly extended at 70 and 160 µm on a north-south axis, with a faint fan tail to the west, particularly at 70 µm. Flux from the coma can be detected out to ≈25-30 arcseconds from the centre of light. The coma slope is almost identical at 70 and at 160 µm.

[10] Although this did not affect the imaging observations, the ephemeris of the comet was found to be deficient. Despite all efforts to refine the ephemeris with last-minute astrometry, the lack of radar observations – radar data was not obtained until after the Herschel observations as the comet was below the horizon of the Goldstone radar at closest approach to Earth – showed that the ephemeris had an error of 7 arcseconds at the epoch of the Herschel observations. With the comet in the deep southern sky, very little visible astrometry was reported in the last few days before the Herschel observations and so the degree of refinement of the orbit that was possible with last minute astrometry was limited.

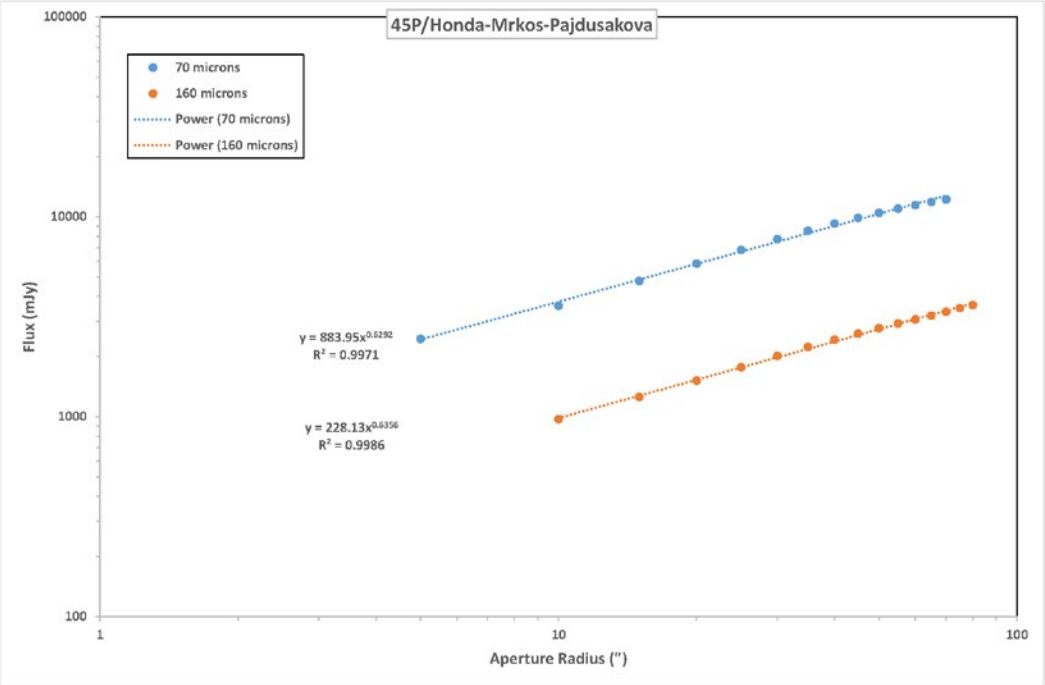

Figure 32: Coma profiles for 45P/Honda-Mrkos-Pajdusakova for the Herschel observations.

8.1.10. 103P/Hartley 2

8.1.10.1. ObsIDs Used

1342207079, 1342207080, 1342209003, 1342209004, 1342209005, 1342209006

8.1.10.2. Background

Discovered on 15th March 1986 by Malcolm Hartley at magnitude 17, the comet was on its fourth return to perihelion when observed by Herschel, all of which have been observed. The comet's orbit is always exterior to the Earth, with a perihelion distance of 1.06 AU (with very close approaches to Earth possible), aphelion at 5.88 AU and a period of 6.47 years. The nucleus has a mean radius of 0.8 km.

103P/Hartley 2 has an interesting dynamic history. Prior to 1947 it had a relatively low eccentricity orbit with perihelion at 2.09 AU and aphelion at 4.90 AU. Close encounters with Jupiter in 1947 and 1971 reduced the comet's perihelion distance, first to 1.62 AU and then to 0.90 AU, greatly increasing the comet's activity[11]. The low heliocentric distance for perihelion is though unstable on timescales of a few centuries: 103P/Hartley 2 will return to a perihelion distance ≈2 AU and the consequent much lower activity in about two centuries from today.

[11] A further Jupiter encounter in 1993 took perihelion back outside the Earth's orbit to the current distance, but another encounter with Jupiter in 2054 will again make it Earth-crossing until yet another Jupiter encounter in 2088 moves perihelion back to the present heliocentric distance once more. See Kinoshita (2017) for details.

8.1.10.3. Visible data

Circumstances were very good for observing the comet in 2010, with the comet close at opposition shortly before perihelion and reaching a total visual magnitude of slightly brighter than 5. The comet remained close to the Earth and relatively bright for several months as the comet essentially moved parallel to the Earth's orbit for the last third of 2010. The entry in Yoshida's on-line catalogue of light curves (http://www.aerith.net/comet/catalog/0103P/2010.html) finds a best light curve fit preperihelion, inside 4.3 AU, of $m_1 = 8.7 + 5 \log \Delta + 20 \log r$ (t-20). The relatively large pre-perihelion heliocentric distance of switch-on of activity is consistent with a nucleus that is less evolved than the others in our sample, typical of objects that have recently experienced a large downward jump in perihelion distance.

CCD aperture photometry by the Spanish "Observadores_cometas" group finds Afρ≈3400 cm within a 25000 km aperture at the epoch of the Herschel observation[12], showing activity of the order of one tenth that of 1P/Halley at the same heliocentric distance. The coma slope, fitted as integrated magnitude against $\log_{10}$ aperture diameter from CCD photometry, is close to the ideal "ideal" 1/r coma profile, although slightly more condensed down to 1.2 AU. Between 1.2 AU and perihelion it is essentially an ideal 1/r coma. Images show a strongly green coma, typical of C_2 emission with a faint, broad tail extending slightly to the north of west, with a faint, narrow gas tail embedded within it. Visually, the gas coma was as large as 45 arcminutes at the time of the Herschel observations, although diameters as large as a degree were registered a week before the Herschel observing campaign started.

Date	Exposure	Telescope	Filter	Observer	Site
23/10/2010	360s	16cm	RGB+Unfiltered	Ligustri	MPC H06 (New Mexico, USA)
04/11/2010	210s	25.4cm	BVR+unfiltered	Ligustri	MPC H06 (New Mexico, USA)
10/11/2010	1560s	25cm	Unfiltered	Tifner	MPC I32 (Rosario, Argentina)

[12] Again, we choose this smaller aperture as, in general, little flux is measured outside this coma diameter by CCD observers.

Table 21: Details of the complementary visible images for 103P/Hartley 2. These are not necessarily the images that are most nearly simultaneous with the Herschel data, but instead are the images as close temporally to the epoch of the Herschel observation that provide the most useful comparison in terms of depth, image scale and s/n. From left to right we give: the date of observation; the exposure time (if recorded – otherwise blank); the telescope diameter; the photometric filter or filters used (otherwise "unfiltered"; the observer name or names; and the observing site. The code that is listed is the Minor Planet Center IAU site code (see https://www.minorplanetcenter.net/iau/lists/ObsCodesF.html for details).

8.1.10.4. Herschel data

Herschel took imaging photometry at 70 and 160 µm at three epochs, with data obtained at 100 µm at the second and third epochs: the first epoch of observation was three days before perihelion, the second and third, seven and fourteen days respectively after perihelion. The observations were taken using 45°/135° angles for scan and cross-scan.

Date	Observing mode	Integration Time	Scan speed	Scan length	Cross-scan separation	# Scan legs	# Repetitions
25/10/2010	Scan map	1420s	20"/s	9.9 '	148.5"	3	4
04/11/2010	Scan map	1420s (70 & 100 µm) 2840s (160 µm)	20"/s	9.9 '	148.5"	3	4
11/11/2010	Scan map	1420s (70 & 100 µm) 2840s (160 µm)	20"/s	9.9 '	148.5"	3	4

Table 22: Observing parameters for the observations of 103P/Hartley 2 presented in the catalogue. From left to right the columns are: date of observation, observing mode, observation duration (sum of scan and cross-scan), scan speed, length of each scan leg, separation of the scan legs, the number of scan legs executed in the scan pattern, number of repetitions of the scan pattern.

8.1.10.5. Summary of results

The coma is clearly extended at 70 and 160 µm on an east-west axis, with an obvious tail orientated slightly to the north of west, particularly at 70 µm, although visible too at 100 and at 160 µm. The tail orientation is identical to that seen in the quasi-simultaneous CCD images. Flux from the tail can be detected out to ≈4 arcminutes from the centre of light, with flux from the coma out to ≈80 arcseconds. The coma slope is similar at 70 and 100 µm, with almost identical values being found at both wavelengths and at all three epochs. The coma though, although still steep, is significantly flatter and more extended at 160 µm at all three epochs.

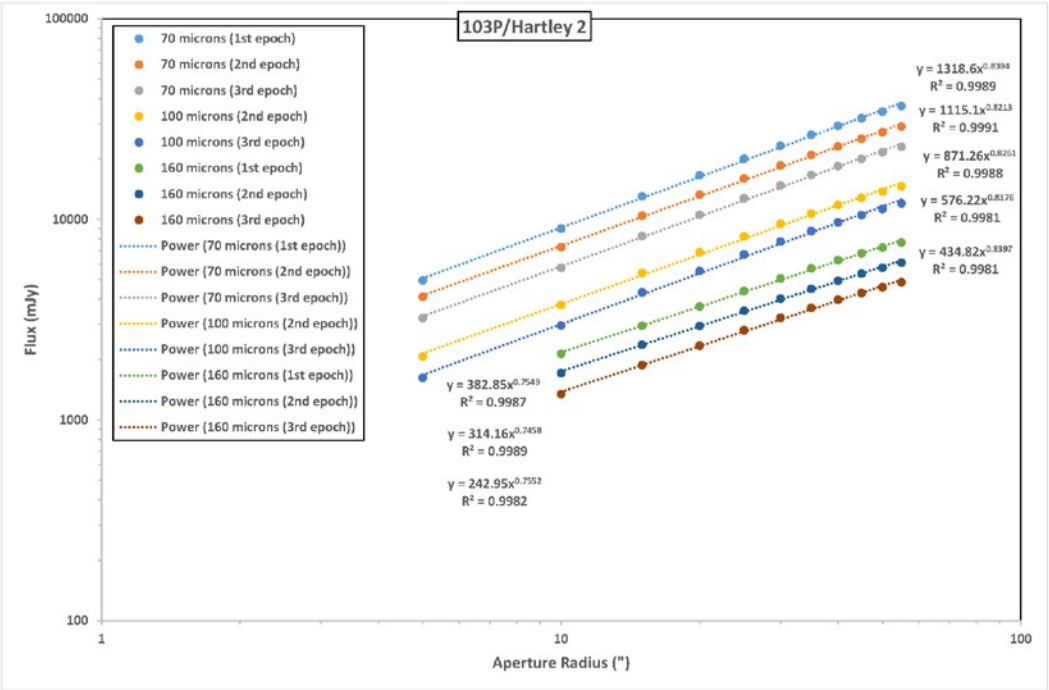

Figure 33: Coma profiles for 103P/Hartley 2 for the three epochs of observation.

8.2. Summary of aperture photometry

Comet	Date	OD	r	Delta	Band	Radius 1 (")	Radius 2 (")	Intercept	Slope	Radius 1 (km)	Radius 2 (km)	Flux (Radius 1, mJy)	Flux (Radius 2, mJy)
C/2006 W3 (Christensen)	01/11/2009	171	3.326	3.557	70	5	55	1318.60	0.84	424	4668	5091.3	38104.3
C/2006 W3 (Christensen)	26/08/2010	469	4.955	4.538	70	5	55	1115.10	0.82	497	5466	4181.9	29969.1
C/2006 W3 (Christensen)	01/11/2009	171	3.326	3.557	160	5	55	871.26	0.83	660	7261	3292.8	23870.5
C/2006 W3 (Christensen)	26/08/2010	469	4.955	4.538	160	5	30	842.11	0.58	2727	16364	2136.6	6024.0
C/2009 P1 (Garradd)	19/10/2011	889	1.791	1.911	70	10	50	55.08	0.84	48129	240643	383.1	1486.0
C/2009 P1 (Garradd)	27/11/2012	1293	2.15	3.115	70	10	75	84.21	0.58	42347	317606	316.7	1009.4
C/2009 P1 (Garradd)	27/11/2012	1293	2.15	3.115	100	10	50	61.66	0.56	42217	211084	225.1	556.6
C/2009 P1 (Garradd)	19/10/2011	889	1.791	1.911	160	15	40	883.95	0.63	696	1857	4857.6	9004.2
C/2009 P1 (Garradd)	27/11/2012	1293	2.15	3.115	160	5	70	48.82	0.49	6108	85507	106.9	386.3
C/2011 L4 (PanSTARRS)	09/09/2012	1140	3.261	3.582	70	5	60	826.79	0.81	12901	154810	3058.6	23050.3
C/2011 L4 (PanSTARRS)	09/09/2012	1140	3.261	3.582	160	5	55	185.32	0.89	16459	181046	781.8	6675.8
C/2012 S1 (ISON)	13/03/2013	1400	4.47	4.095	70	5	60	1473.90	0.88	6931	83172	6039.1	53292.0
C/2012 S1 (ISON)	13/03/2013	1400	4.47	4.095	160	5	65	690.76	0.90	11298	146870	2961.7	30137.5
C/2013 A1 (Siding Spring)	31/03/2013	1418	6.478	6.872	70	5	35	1207.70	0.35	12991	90940	2132.6	4241.1
C/2013 A1 (Siding Spring)	31/03/2013	1418	6.478	6.872	100	5	25	74.75	0.32	14852	74260	125.9	212.1
C/2013 A1 (Siding Spring)	31/03/2013	1418	6.478	6.872	160	7	15	17.78	0.25	34893	74772	29.2	35.4
9P/Tempel 1	20/07/2011	797	2.3	1.684	70	5	55	576.22	0.82	497	5466	2148.2	15258.4
9P/Tempel 1	20/07/2011	797	2.3	1.684	100	5	55	434.82	0.84	660	7261	1679.7	12580.3

9P/Tempel 1	20/07/2011	797	2.3	1.684	160	10	70	11.78	0.81	12215	85507	76.3	370.0
10P/Tempel 2	06/07/2010	418	1.423	0.752	70	5	40	376.38	0.82	11298	90382	1412.7	7801.9
10P/Tempel 2	06/07/2010	418	1.423	0.752	160	9	15	7.82	0.40	44863	74772	18.7	22.9
29P/Schwassmann-Wachmann 1	10/06/2010	392	6.215	6.635	70	10	55	382.85	0.75	849	4668	2177.4	7885.5
29P/Schwassmann-Wachmann 1	02/01/2011	599	6.244	5.838	70	10	55	314.16	0.75	994	5466	1749.6	6239.0
29P/Schwassmann-Wachmann 1	17/02/2013	1375	6.231	5.82	70	10	55	242.95	0.76	1320	7261	1382.7	5010.0
29P/Schwassmann-Wachmann 1	10/06/2010	392	6.215	6.635	160	10	30	243.30	0.49	5455	16364	746.9	1275.4
29P/Schwassmann-Wachmann 1	02/01/2011	599	6.244	5.838	160	10	45	16.32	0.60	48129	216579	64.3	157.4
29P/Schwassmann-Wachmann 1	17/02/2013	1375	6.231	5.82	160	10	45	33.62	0.55	42347	190563	120.0	275.5
45P/Honda-Mrkos-Pajdusakova	16/08/2011	824	1.002	0.064	70	10	50	10.92	0.63	42217	211084	46.7	128.8
45P/Honda-Mrkos-Pajdusakova	16/08/2011	824	1.002	0.064	160	10	35	228.13	0.64	464	1625	985.8	2185.7
103P/Hartley 2	25/10/2010	529	1.06	0.117	70	10	70	2.34	1.11	12215	85507	29.9	257.1
103P/Hartley 2	04/11/2010	539	1.063	0.137	70	10	60	209.89	0.80	25802	154810	1324.0	5550.5
103P/Hartley 2	11/11/2010	546	1.076	0.182	70	10	50	50.42	0.91	32918	164588	410.1	1774.8
103P/Hartley 2	04/11/2010	539	1.063	0.137	100	10	65	51.96	0.83	13862	90102	353.5	1679.8
103P/Hartley 2	11/11/2010	546	1.076	0.182	100	10	35	13.18	0.80	22595	79084	83.3	227.2
103P/Hartley 2	25/10/2010	529	1.06	0.117	160	5	35	357.59	0.23	12991	90940	515.0	800.6
103P/Hartley 2	04/11/2010	539	1.063	0.137	160	10	30	13.82	0.46	29704	89112	39.7	65.8
103P/Hartley 2	11/11/2010	546	1.076	0.182	160	10	15	7.20	0.31	49848	74772	14.8	16.9

Table 23: Summary of photometric data for the objects listed in this catalogue. The columns are, from left to right: comet name; date of observation, OD of observation, heliocentric distance at time of observation, herschelcentric distance at time of observation; wavelength; radius in arcsec of minimum photometric aperture used for the fit; radius in arcsec of the maximum aperture

used for the observation; intercept of power law fit to flux v aperture; exponent of power law fit to flux v aperture; physical size at the comet in kilometres of the minimum photometric aperture used for the fit; physical size at the comet of the maximum aperture used for the fit; total integrated flux in mJy calculated from the fit within the smallest aperture radius; total integrated flux in mJy calculated from the fit within the maximum aperture radius.

9. Analysis

The aim of this catalogue is to make it possible for scientists to exploit this important Herschel data set in new and imaginative ways. Thus it would defeat our purpose for us to define the possible lines of use of the data. Here we limit ourselves to showing just a few, simple correlations that illustrate the possibilities of the data.

Evidently, the raw data has obvious limitations. A small comet, with low activity, but close to the Earth and to the Sun, may give fluxes as high as a much larger comet that is much more distant from the Sun. All other factors being equal, the inverse square law states that the amount of radiation received by the target with be four times as high at a heliocentric distance of 1AU as at 2AU. At the same time, the amount of radiation received from the target at the Earth or, in this case, at Herschel's detectors, also scales as the inverse square of the herschelcentric distance. In reality, a comet's activity increases as it gets closer to the Sun so, typically, in the visible, a comet will brighten as r^n, where typically $3<n<4$. However, we can normalise the Herschel fluxes by multiplying them by a factor of $r^2*\Delta^2$ to convert them to equivalent fluxes at 1 AU from both the Sun and Herschel, as shown in Figure 34.

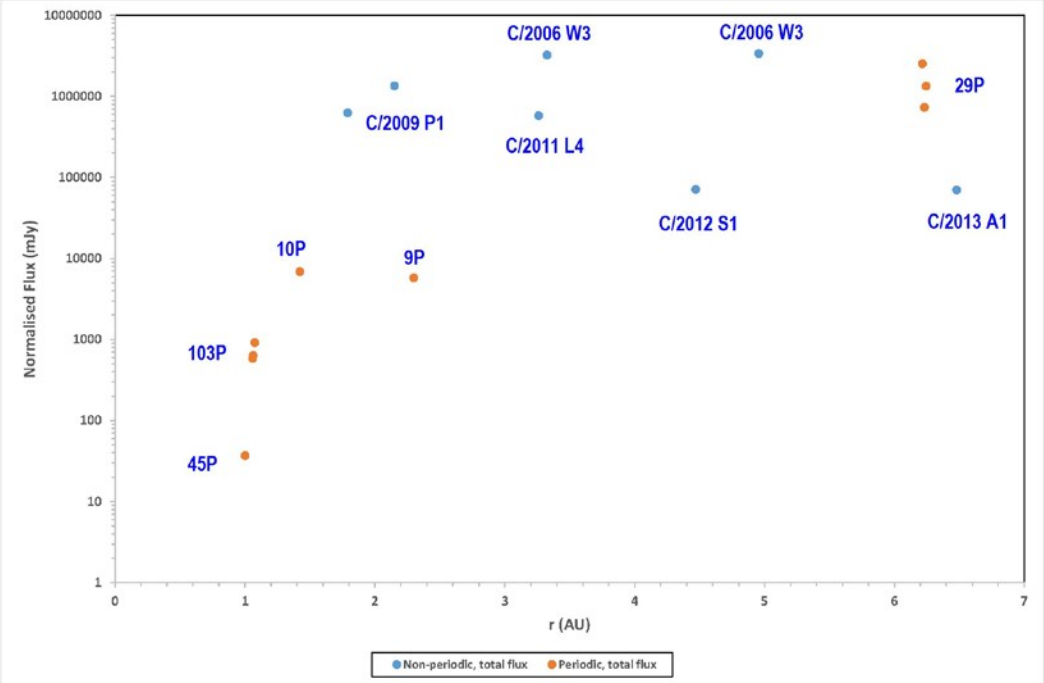

*Figure 34: Total normalised flux (flux integrated out to the limit of the detectable coma) in mJy for the comets in our sample – measured flux * r^2 * Δ^2 – against the heliocentric distance at the epoch of observation. The identity of the individual objects is marked.*

Figure 34 allows us to see at a glance whether an object is of high or low activity at the heliocentric distance at which it was observed. We see that the highest normalised fluxes correspond to C/2006 W3 (Christensen) which, is clearly an object of high activity. The second most active object in our sample is 29P/Schwassmann-Wachmann 1. For 29P, we find that there is a difference of a factor of ≈3 between the highest and lowest normalised flux and that the highest normalised flux corresponds to the first epoch of observation, at which time it was declining from outburst (see Section 10.1.8.3), while the lowest normalised flux corresponds to the third epoch of observation when the comet was

in quiescence and at a particularly low state of activity. We see in the context for these observations in the normalised visible light curve, plotted as R – 5*log10 Δ – 5* log10 r against date, with the epochs of the Herschel observations identified.

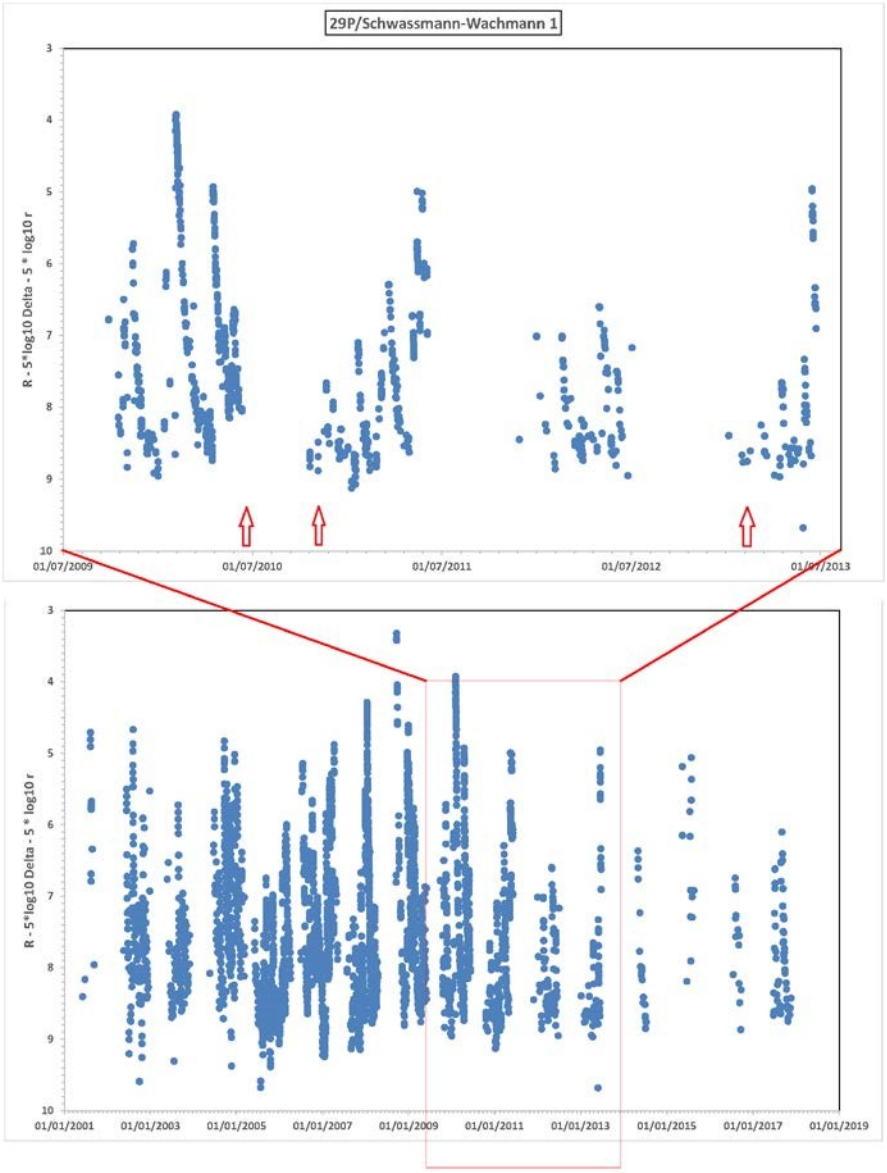

Figure 35: The context for the Herschel observations of 29P/Schwassmann-Wachmann 1. The normalised magnitude from CCD photometry in R obtained between 2001 and 2017 is plotted against date. In the upper panel, the photometry covering the period of the Herschel mission is shown on an expanded scale. We see that the visible flux was approximately a factor of 2 higher at the first epoch of observation than at the second or third, when it was in a quiescent state. We can see that there was a slow decline in the baseline level during the Herschel mission.

During the course of the Herschel mission activity declined rapidly, picking-up again shortly after the end of Helium. At the same time, we see a slow decline in the baseline brightness in the visible, consistent with the decline in activity. Figure 36 and Figure 37 show the relationship between the flux measured by Herschel and the size of the coma detected in the Herschel data. In Figure 36 we see that there is no obvious correlation between the physical size of the coma and the total flux measured to the limiting diameter of the coma that were measured by Herschel. Nor is there an obvious

difference between the focus of the highly evolved, periodic comets of the Jupiter family and the dynamically new, non-periodic comets.

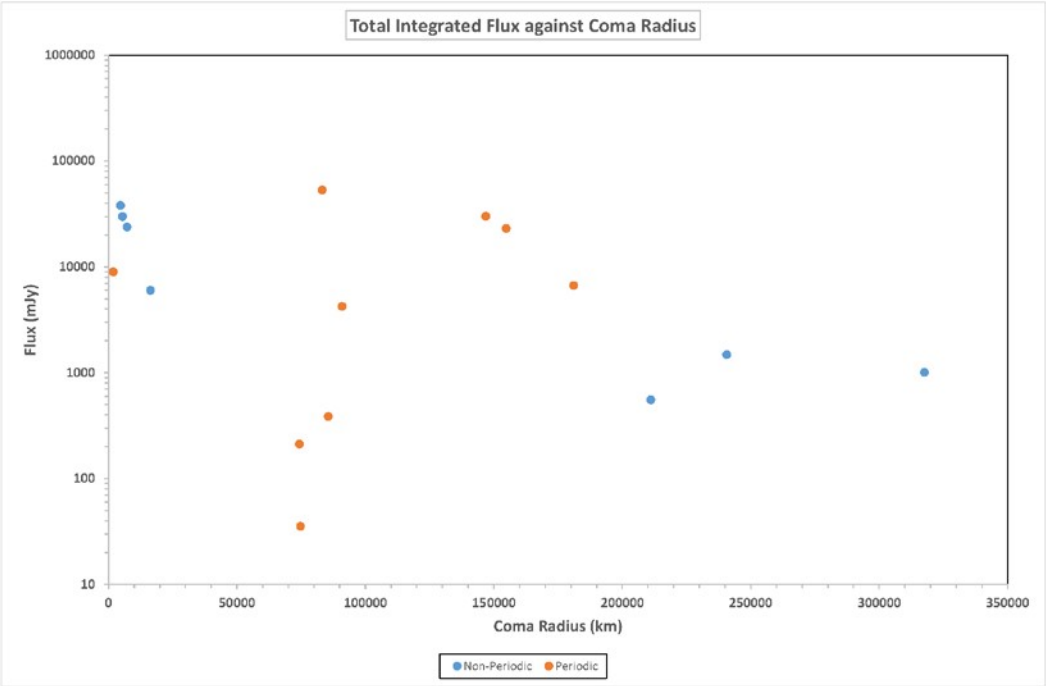

Figure 36: Total integrated flux in mJy to the limit of the detectable coma against the coma radius in Km for the comets in our sample.

However, if instead we plot the normalized Herschel flux against the Herschel coma diameter where, once again, we correct the total flux measured out to the limiting diameter of the coma by a factor of $r^2 * \Delta^2$ to bring it to a nominal 1 AU both heliocentric and herschelcentric distance, against the coma radius, we do see a significant correlation (Figure 37). The locus of the Jupiter family comets is the lower left of the plot, save for 29P, which is the highest points to the top right. Comets 29P (which is a particularly unusual case in an intermediate period orbit), C/2006 W3 and C/2009 P1 occupy a similar locus on the diagram, indicating a high level of intrinsic activity. Comets C/2011 L4, C/2012 S1 and C/2013 A1 have an activity an order of magnitude lower than our three most active objects, but still significantly higher than the most active of the short period comets – 9P and 10P. In contrast, 45P is the least active object in the sample by approximately an order of magnitude.

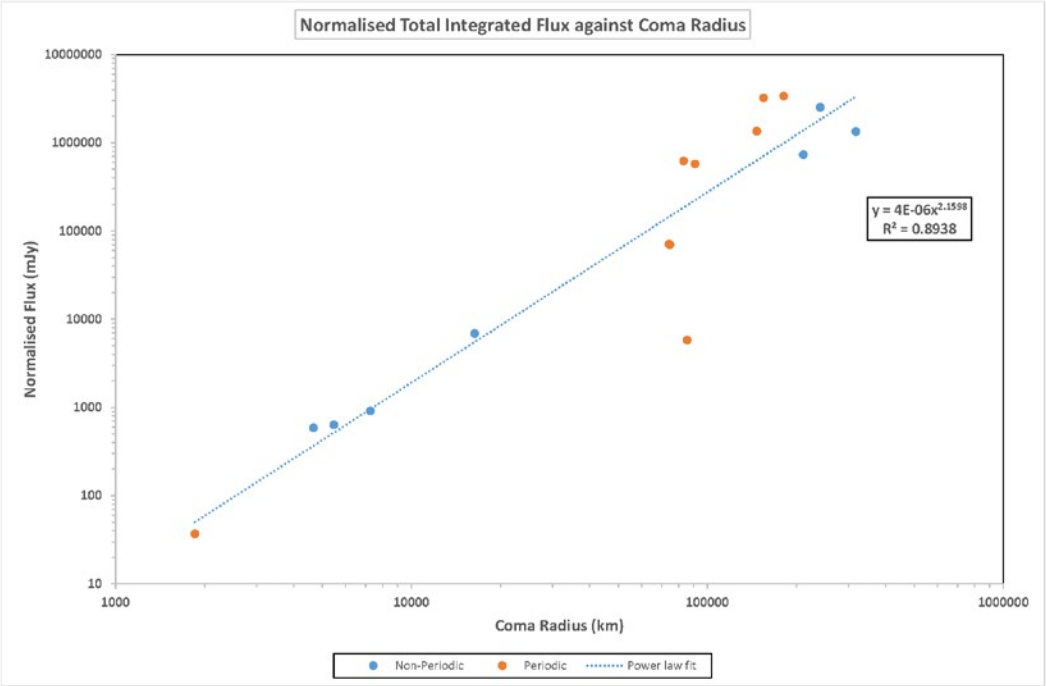

Figure 37: Normalised total integrated flux to the limit of the coma, in mJy, against the coma radius, in Km. We see a strong correlation between the maximum detectable extent of the coma and the normalised total flux in the sense that the comets with the largest coma also have the largest normalized flux.

In contrast, there seems to be no obvious relationship between the slope of the coma and the heliocentric distance at the time of observation. The comets in our sample do not show consistent differences between 70 and 160 µm, or between periodic and non-periodic objects, or between objects observed at large and small heliocentric distance.

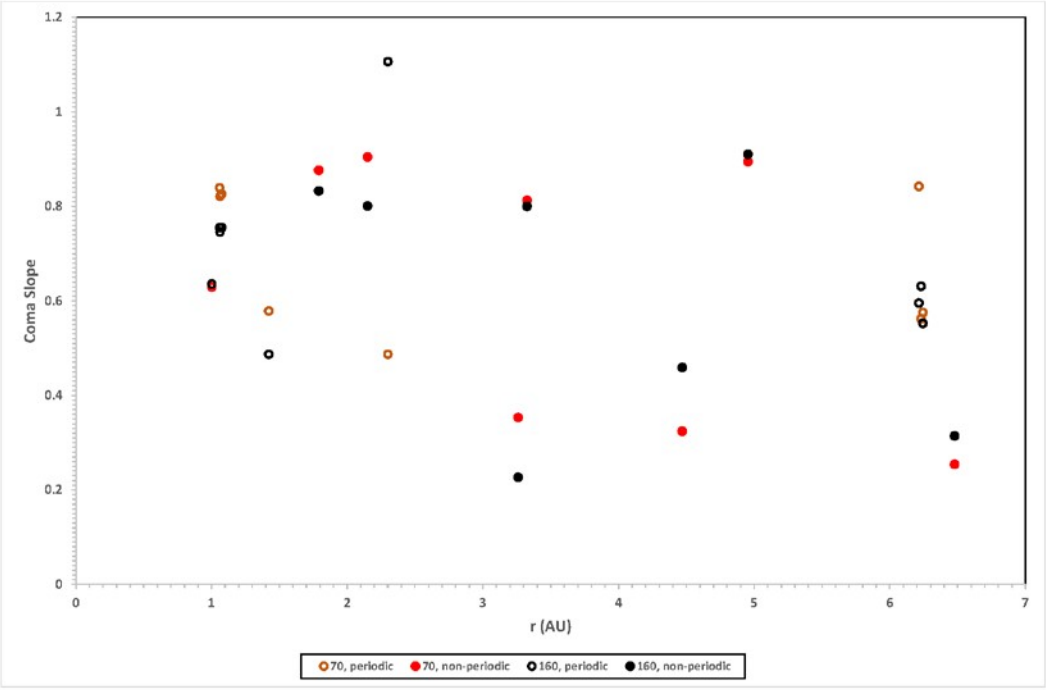

Figure 38: Plot of slope of the coma at 70 and 160 µm against the heliocentric distance at the epoch of observation. There is no obvious correlation between the slope of the coma and the heliocentric distance for the comets in the sample, although

there is a suggestion that they may split into two groups on the y-axis, with one group that has a slope of ≈0.8 and the other ≈0.3-0.4.

There is a suggestion of a split into two groups: one of slope ≈0.8 and another with slope ≈0.3-0.4, but this could be fortuitous, or due to selection effect in the data.

10. Contributing Observers

The observers who have contributed visual or CCD data that have been referenced in this catalogue to give context for the Herschel data are listed in Table 24.

CCD Observers		
Name	Instrument	Site code
Faustino Garcia	25cm	MPC J38 (Asturias, Spain)
Juan José (Juanjo) González	23.5cm	MPC J01 (León, Spain)
Francisco Hernández	40cm	MPC J24 (Tenerife, Spain)
Rolando Ligustri	16cm	MPC H06 (New Mexico, USA)
Rolando Ligustri	25.4cm	MPC H06 (Mayhill, New Mexico)
Rolando Ligustri	40cm	MPC Q62 (Siding Spring, Australia)
Rolando Ligustri	50cm	MPC H06 (New Mexico, USA)
Rolando Ligustri & Di Giusto	35cm	MPC 235 (Talmassons, Italy)
Fernando López	12.5cm	MPC J63 (Alicante, Spain)
Juan Lozano	25cm	MPC I57 (Elche, Spain)
Gustavo Muler	30cm	MPC J47 (Lanzarote, Spain)

Ramón Naves and Montse Campàs	30cm	MPC 213 (Barcelona, Spain)
Fernando Tifner	25cm	MPC I32 (Rosario, Argentina)
Visual Observers		
Valentín Díaz	Multiple	Alicante, Spain
Juan José (JJ) González		Asturias, Spain
Carlos Labordena		Castellón, Spain

Table 24: Table of observers who contributed to this study with either CCD images or visual observations. The observations used were selected from a much larger pool of data from many more observers, whose efforts are gratefully acknowledged. From left to right we give the observer's name, the instrument used and the site code and location. For the visual observers, who are by nature mobile, the principal observing location is shown – no instrument details are given as a single observer may have used as many as half a dozen instruments on different occasions, from the naked eye to 20cm diameter, according to the object to be observed and its circumstances of observation.

11. Conclusions

Making meaningful photometry of comets with an extended coma poses multiple issues for the observer, as does the problem of how to compare different objects observed in very different conditions. We have applied aperture photometry in multiple apertures in an attempt to resolve these issues, showing that we can interpolate the fitted coma profile to calculate the integrated flux within particular physical aperture sizes at the comet. We combine these data with CCD imaging in the visible to understand better the activity of the ten active comets that were observed by Herschel during its almost four years of cold mission. To date, very little work has been done on the coma profiles of comets in the infrared. We show that for the comets in our sample, CCD observations in the visible show that almost all tend to a 1/r coma profile approximation close to perihelion. In contrast, the infrared profiles are, with a single exception, all flatter than 1/r, some of them, considerably so.

12. References

A'Hearn, M. F.; Schleicher, D. G.; Millis, R. L.; Feldman, P. D.; Thompson, D. T., 1984, Comet Bowell 1980b, AJ, 89, 579

A'Hearn, Michael F.; Combi, Michael R., 2007, Deep Impact at Comet Tempel 1, Icarus, 187, 1 Bauer,

O.H, 2006, PACS Instrument Description Document Part I, PACS-ME-GR-002, v3.1

Baum, William A.; Kreidl, Tobias J.; Schleicher, David G., 1992, Cometary grains, AJ, 104, 1216

de Graauw, Th.; Helmich, F. P.; Phillips, T. G.; Stutzki, J.; Caux, E.; Whyborn, N. D.; Dieleman, P.; Roelfsema, P. R.; Aarts, H.; Assendorp, R.; Bachiller, R.; Baechtold, W.; Barcia, A.; Beintema, D. A.; Belitsky, V.; Benz, A. O.; Bieber, R.; Boogert, A.; Borys, C.; Bumble, B.; Caïs, P.; Caris, M.; Cerulli-Irelli, P.; Chattopadhyay, G.; Cherednichenko, S.; Ciechanowicz, M.; Coeur-Joly, O.; Comito, C.; Cros, A.; de Jonge, A.; de Lange, G.; Delforges, B.; Delorme, Y.; den Boggende, T.; Desbat, J.-M.; Diez-González, C.; di Giorgio, A. M.; Dubbeldam, L.; Edwards, K.; Eggens, M.; Erickson, N.; Evers, J.; Fich, M.; Finn, T.; Franke, B.; Gaier, T.; Gal, C.; Gao, J. R.; Gallego, J.-D.; Gauffre, S.; Gill, J. J.; Glenz, S.; Golstein, H.; Goulooze, H.; Gunsing, T.; Güsten, R.; Hartogh, P.; Hatch, W. A.; Higgins, R.; Honingh, E. C.; Huisman, R.; Jackson, B. D.; Jacobs, H.; Jacobs, K.; Jarchow, C.; Javadi, H.; Jellema, W.; Justen, M.; Karpov, A.; Kasemann, C.; Kawamura, J.; Keizer, G.; Kester, D.; Klapwijk, T. M.; Klein, Th.; Kollberg, E.; Kooi, J.; Kooiman, P.-P.; Kopf, B.; Krause, M.; Krieg, J.-M.; Kramer, C.; Kruizenga, B.; Kuhn, T.; Laauwen, W.; Lai, R.; Larsson, B.; Leduc, H. G.; Leinz, C.; Lin, R. H.; Liseau, R.; Liu, G. S.; Loose, A.; López-Fernandez, I.; Lord, S.; Luinge, W.; Marston, A.; Martín-Pintado, J.; Maestrini, A.; Maiwald, F. W.; McCoey, C.; Mehdi, I.; Megej, A.; Melchior, M.; Meinsma, L.; Merkel, H.; Michalska, M.; Monstein, C.; Moratschke, D.; Morris, P.; Muller, H.; Murphy, J. A.; Naber, A.; Natale, E.; Nowosielski, W.; Nuzzolo, F.; Olberg, M.; Olbrich, M.; Orfei, R.; Orleanski, P.; Ossenkopf, V.; Peacock, T.; Pearson, J. C.; Peron, I.; Phillip-May, S.; Piazzo, L.; Planesas, P.; Rataj, M.; Ravera, L.; Risacher, C.; Salez, M.; Samoska, L. A.; Saraceno, P.; Schieder, R.; Schlecht, E.; Schlöder, F.; Schmülling, F.; Schultz, M.; Schuster, K.; Siebertz, O.; Smit, H.; Szczerba, R.; Shipman, R.; Steinmetz, E.; Stern, J. A.; Stokroos, M.; Teipen, R.; Teyssier, D.; Tils, T.; Trappe, N.; van Baaren, C.; van Leeuwen, B.-J.; van de Stadt, H.; Visser, H.; Wildeman, K. J.; Wafelbakker, C. K.; Ward, J. S.; Wesselius, P.; Wild, W.; Wulff, S.; Wunsch, H.-J.; Tielens, X.; Zaal, P.; Zirath, H.; Zmuidzinas, J.; Zwart, F., 2010, The Herschel-Heterodyne Instrument for the Far-Infrared (HIFI), A&A 518, L6

Exter, K., 2017, Herschel Explanatory Supplement Volume III: The Photodetector Array Camera And Spectrometer (PACS) Handbook, HERSCHEL-HSC-DOC-2101, v2.0

Ferlet, Marc, 2010, In-flight characterisation of Herschel-SPIRE optical performances, Space Telescopes and Instrumentation 2010: Optical, Infrared, and Millimeter Wave. Edited by Oschmann, Jacobus M., Jr.; Clampin, Mark C.; MacEwen, Howard A., Proceedings of the SPIE, 7731, id. 773135

Feuchtgruber, F., Sturm, E., and Poglitsch, A. (2010). PACS OBCPs and DMC Sequences. PICC-ME-LE005, v2.2.

Feuchtgruber, H., 2010, PACS OBCPs and DMC Sequences, PACS-ME-LI-005, v2.2

Fink U. & Rubin M., 2012, The calculation of Afρ and mass loss rate for comets, Icarus, 221, 721

G. L. Pilbratt, J. R. Riedinger, T. Passvoge, G. Crone, D. Doyle, U. Gageur, A. M. Heras, C. Jewel, L. Metcalfe, S. Ott and M. Schmidt, 2010, Herschel Space Observatory: An ESA facility for far-infrared and submillimetre astronomy, A&A 518, L1

Geis, N. & D. Lutz, 2010, Herschel/PACS modelled point-spread functions, PICC-ME-TN-029, v2.0

Griffin, M. J.; Abergel, A.; Abreu, A.; Ade, P. A. R.; André, P.; Augueres, J.-L.; Babbedge, T.; Bae, Y.; Baillie, T.; Baluteau, J.-P.; Barlow, M. J.; Bendo, G.; Benielli, D.; Bock, J. J.; Bonhomme, P.; Brisbin, D.; Brockley-Blatt, C.; Caldwell, M.; Cara, C.; Castro-Rodriguez, N.; Cerulli, R.; Chanial, P.; Chen, S.; Clark,

E.; Clements, D. L.; Clerc, L.; Coker, J.; Communal, D.; Conversi, L.; Cox, P.; Crumb, D.; Cunningham, C.; Daly, F.; Davis, G. R.; de Antoni, P.; Delderfield, J.; Devin, N.; di Giorgio, A.; Didschuns, I.; Dohlen, K.; Donati, M.; Dowell, A.; Dowell, C. D.; Duband, L.; Dumaye, L.; Emery, R. J.; Ferlet, M.; Ferrand, D.; Fontignie, J.; Fox, M.; Franceschini, A.; Frerking, M.; Fulton, T.; Garcia, J.; Gastaud, R.; Gear, W. K.; Glenn, J.; Goizel, A.; Griffin, D. K.; Grundy, T.; Guest, S.; Guillemet, L.; Hargrave, P. C.; Harwit, M.; Hastings, P.; Hatziminaoglou, E.; Herman, M.; Hinde, B.; Hristov, V.; Huang, M.; Imhof, P.; Isaak, K. J.; Israelsson, U.; Ivison, R. J.; Jennings, D.; Kiernan, B.; King, K. J.; Lange, A. E.; Latter, W.; Laurent, G.; Laurent, P.; Leeks, S. J.; Lellouch, E.; Levenson, L.; Li, B.; Li, J.; Lilienthal, J.; Lim, T.; Liu, S. J.; Lu, N.; Madden, S.; Mainetti, G.; Marliani, P.; McKay, D.; Mercier, K.; Molinari, S.; Morris, H.; Moseley, H.; Mulder, J.; Mur, M.; Naylor, D. A.; Nguyen, H.; O'Halloran, B.; Oliver, S.; Olofsson, G.; Olofsson, H.-G.; Orfei, R.; Page, M. J.; Pain, I.; Panuzzo, P.; Papageorgiou, A.; Parks, G.; Parr-Burman, P.; Pearce, A.; Pearson, C.; Pérez-Fournon, I.; Pinsard, F.; Pisano, G.; Podosek, J.; Pohlen, M.; Polehampton, E. T.; Pouliquen, D.; Rigopoulou, D.; Rizzo, D.; Roseboom, I. G.; Roussel, H.; Rowan-Robinson, M.; Rownd, B.; Saraceno, P.; Sauvage, M.; Savage, R.; Savini, G.; Sawyer, E.; Scharmberg, C.; Schmitt, D.; Schneider, N.; Schulz, B.; Schwartz, A.; Shafer, R.; Shupe, D. L.; Sibthorpe, B.; Sidher, S.; Smith, A.; Smith, A. J.; Smith, D.; Spencer, L.; Stobie, B.; Sudiwala, R.; Sukhatme, K.; Surace, C.; Stevens, J. A.; Swinyard, B. M.; Trichas, M.; Tourette, T.; Triou, H.; Tseng, S.; Tucker, C.; Turner, A.; Vaccari, M.; Valtchanov, I.; Vigroux, L.; Virique, E.; Voellmer, G.; Walker, H.; Ward, R.; Waskett, T.; Weilert, M.; Wesson, R.; White, G. J.; Whitehouse, N.; Wilson, C. D.; Winter, B.; Woodcraft, A. L.; Wright, G. S.; Xu, C. K.; Zavagno, A.; Zemcov, M.; Zhang, L.; Zonca, E., 2010, The Herschel-SPIRE instrument and its in-flight performance, A&A, 518, L3

Kanoshita, K., 2017, 103P/Hartley

Marton G., L. Calzoletti, A. M. Perez Garcia, C. Kiss, R. Paladini, B. Altieri, M. Sánchez Portal, M. Kidger, and the Herschel Point Source Catalogue Working Group, 2017, The Herschel/PACS Point Source Catalogue Explanatory Supplement

Minor Planet Center, 2018, List Of Observatory Codes

Mueller, M. & Jellema, W., 2014, The HIFI Beam: Release #1, Release Note for Astronomers, HIFI-ICCRP-2014-001, v1.1

Müller, T, 2010, PACS Photometer - Point/Compact Source Observations: Mini Scan-Maps & ChopNod, PICC-ME-TN-036, v2.0

Müller, T., 2010, PACS Photometer - Point/Compact Source Observations: Mini Scan-Maps & ChopNod, PICC-ME-TN-036, v2.0

PACS ICC, 2010, PACS photometer - Prime and Parallel scan mode release note, PICC-ME-TN-035, v1.2

Piazzo, L., Calzoletti, L., Faustini, F., Pestalozzi, M., Pezzuto, S., Elia, D., di Giorgio, A., and Molinari, S., 2015, UNIMAP: a generalized least-squares map maker for Herschel data. MNRAS, 447, 1471

Poglitsch, A., C. Waelkens, N. Geis, H. Feuchtgruber, B. Vandenbussche, L. Rodriguez, O. Krause, E. Renotte, C. van Hoof, P. Saraceno J. Cepa, F. Kerschbaum, P. Agnèse, B. Ali, B. Altieri, P. Andreani, J.-L. Augueres, Z. Balog, L. Barl, O. H. Bauer, N. Belbachir, M. Benedettini, N. Billot, O. Boulade, H. Bischof,

J. Blommaert, E. Callut, C. Cara, R. Cerulli, D. Cesarsky, A. Contursi, Y. Creten, W. De Meester, V. Doublier, E. Doumayrou, L. Duband, K. Exter, R. Genzel, J.-M. Gillis, U. Grözinger, T. Henning, J. Herreros, R. Huygen, M. Inguscio, G. Jakob, C. Jamar, C. Jean, J. de Jong, R. Katterloher, C. Kiss, U. Klaas, D. Lemke, D. Lutz, S. Madden, B. Marquet, J. Martignac, A. Mazy, P. Merken, F. Montfort, L. Morbidelli, T. Müller, M. Nielbock, K. Okumura, R. Orfei, R. Ottensamer, S. Pezzuto, P. Popesso, J. Putzeys, S. Regibo, V. Reveret, P. Royer, M. Sauvage, J. Schreiber, J. Stegmaier, D. Schmitt, J. Schubert, E. Sturm, M. Thiel, G. Tofani, R. Vavrek, M. Wetzstein, E. Wieprecht and E. Wiezorrek, 2010, The Photodetector
Array Camera and Spectrometer (PACS) on the Herschel Space Observatory, A&A 518, L2

Romero Calvo, C., 2018, Masters Dissertation, Technische Universität, Berlin, Fakultät VI, IGG

Sauvage, M. & K. Okumura, 2005, Preparing AOTs for the PACS photometer, SAp-PACS-MS-0186-03, v2.1

Schulz Bernhard, Gábor Marton, Ivan Valtchanov, Ana María Pérez García, Sándor Pintér, Phil Appleton, Csaba Kiss, Tanya Lim, Nanyao Lu, Andreas Papageorgiou, Chris Pearson, John Rector, Miguel Sánchez Portal, David Shupe, Viktor L. Tóth, Schuyler Van Dyk, Erika Varga-Verebélyi, Kevin Xu, 2017, SPIRE Point Source Catalog Explanatory Supplement

Valtchanov, I, 2017, Herschel Explanatory Supplement Volume Iv, The Spectral And Photometric Imaging Receiver (SPIRE) Handbook, HERSCHEL-DOC-0798, v3.1

Various, 2018, Herschel Legacy Ancillary Data Product (ADP) pages

Various, 2018a, The Herschel PACS Documentation Library pages

Yoshida, S., 2006, 9P/Tempel 1 (2005)

Yoshida, S., 2011, 29P/Schwassmann-Wachmann 1 (2004)

Yoshida, S., 2011, C/2006 W3 (Christensen)

Yoshida, S., 2012, 9P/Tempel 1 (2012)

Yoshida, S., 2012a, 45P/Honda-Mrkos-Pajdusakova (2011)

Yoshida, S., 2013, C/2011 L4 (PanSTARRS)

Yoshida, S., 2013a, C/2012 S1 (ISON)

Yoshida, S., 2013b, 103P/Hartley 2

Yoshida, S., 2014, C/2009 P1 (Garradd)

Yoshida, S., 2017, C/2013 A1 (Siding Spring)

Yoshida, S., 2018, 29P/Schwassmann-Wachmann 1 (2019)